Emerging Evidence of a Second Glass Phase in Strong to Ultra-Fragile Bulk Metallic Glass-Forming Liquids

Thesis by

Sydney Lea Corona
they.them.theirs

In Partial Fulfillment of the Requirements for the
Degree of
Doctor of Philosophy

Caltech

CALIFORNIA INSTITUTE OF TECHNOLOGY
Pasadena, California

2022
Defended 28 April 2022

To the part of me I lost

And all the parts I found

ACKNOWLEDGEMENTS

Your PhD is a fight. On the third floor of Keck there is a story that describes one's thesis defense as fighting a snake (Appendix E). It describes that the longer the time spent in your PhD, the smaller the snake you fight in your defense. But what they don't tell you is that some of us come in with a snake we are already fighting. Sometimes these are small battles, sometimes they are life or death. Mine were the latter. I entered Caltech with PTSD, anxiety, and depression. Through my time here I found myself, my chosen family, re-found my given family, and much more. Through communities of dance and climbing I found self expression, strength, and encouragement. Through my advisor's field of researchers he nurtured himself, I found camaraderie and family. Around the world in my research exchange in Finland I found how small this place really is and how connected we can be. Through all of it, I found a family, and that family saved my life.

First, I want to first thank my advisor, Bill Johnson, for both long discussions about science and open conversations about the rigor and difficulty of graduate school. I have always appreciated your honesty, and it has helped me find my way. The group you fostered over your career is full of genuine, kind, and humble humans, as well as impactful and impressive researchers. This unique combination of traits comes directly from your humility, brilliance, and hard work, and drives me to raise students and postdocs of the same quality of person hood. And finally, thank you Bill for granting me the freedom to grow both personally and professionally, for the second could not have happened without the first.

I would like to thank my co-advisor, Konrad Samwer. Your enthusiasm and support for my degree has been continually validating. I appreciate so greatly your offering to be my co-advisor "whether it can be done formally or not" simply because you wanted to support me on my journey. Your guidance has helped me find a next job that is supportive of my professional and personal journey, and your emphasis and reminders to maintain myself and my values remain close to my heart.

I would like to thank Bill Goddard for your kindness and generosity. You offered me a group to interact with in my last year — offering me the camaraderie I had been missing. Thank you for making me a welcomed member of the group, enthusiastically discussing my work at such dinners with anyone who would listen,

and for collaborating on our computational works. Your brilliance and guidance are greatly appreciated.

Thank you Keith Schwab for our regular chats throughout my degree. We sometimes discussed work, but most often we discussed the things we enjoy and keep us sane: the outdoors. Thank you for encouraging me to always follow my passions and to continue my hobbies no matter how hard work became, for that was when they would be most important. I look forward to these chats through our futures as well.

Thank you Brent Fultz for supporting my accommodations during courses in my first two years, and providing research group camaraderie in my third and fourth years. Your group has been very supportive, a joyful home base at conferences, and I am greatly appreciative for you all.

Thank you Kathy Faber for supporting my candidacy work and including me in your group in my early Caltech years. Our passing conversations in the halls of Keck gave wonderful support and guidance to new instruments and techniques.

I would like to thank my candidacy committee, Kathy Faber, Keith Schwab, and Brent Fultz for their time in my candidacy exam, guidance throughout my degree, and support as I finish.

Next I want to thank my therapists and my self for the work put in to better understand myself and my needs throughout my career. I entered graduate school with PTSD and the regular work independently and in therapy has helped me immensely with maneuvering how I interact with the world. I write this for I believe it should not be kept secret, for battles with mental health should be de-stigmatized. I started therapy the year before graduate school, continued throughout, and will continue through my career. I would also like to thank my therapy cat, Paisley, for she has been so joyously supportive and silly every time I need it.

I want to thank my mentors turned friends that have supported me throughout my career thus far — Emily Kinser, Jenna Balestrini, and Sam Johnson for being unstoppable female forces. Michael Floyd and Andrew Hoff for their expertise in maneuvering the graduate experience in Bill's lab. Jose Lado and Bruno Amorim for your advice and guidance on my first postdoc proposal — offering your time to someone you did not know was incredibly validating and you have all of my gratitude. And to all of you, I am continually grateful for your candid honesty about your experience. It prepared me more than I could imagine. Thank you.

I would like to thank those I met in my hobbies of climbing and dancing over the

last few years. Your encouragement and excitement have been a wonderful balance to the stress of graduate school. Thank you for holding safe space for me and all my parts. I loved sharing in these spaces. I could not possibly write a list in fear of missing someone, so know I love you all dearly and hold you close in my heart.

I would like to thank my family for their unconditional love, support, and acceptance of me and my self as I have grown into who I am as a person. This has been deeply healing for me, and words cannot express how much your love in these recent years has meant, and how foundational it has been in the development of my strengths. Your love and acceptance of my non-binary self has been beautiful. Thank you, I love you all. Mom and Dad, I love you so dearly. Thank you for being there to listen and/or support me in whatever ways I've needed over my life. You both listen and care so beautifully, and it means so much.

Paul Buerkner, thank you for always being yourself and showing me I can do the same. You were the first person to give me the safe space to be fully myself outside of gender, and you see me for all I am, always. I continually learn so much from you and words cannot describe how wonderful you are. I love you deeply and I remain excited for all of our adventures to come.

David Cutler-Creutz, your love and support have helped me find more love and deeper acceptance for my self and my body. You help me relinquish insecurities I no longer want to carry, showing me they were never mine to hold in the first place. Thank you for sharing in this adventure with me, for our explorations and silly adventures fill my joyous memories. I'm sure I'll see you soon.

Éowyn Lucas, thank you for showing me how strong someone can be — in body, mind, and heart — and for showing me I have that in myself too. Our friendship is so deeply supportive of independence, autonomy, human connection, and safe spaces. You are such a genuine, loving human. Let's go cry on some big walls.

Thank you Katie Shanks, Claire Saunders, Daniel Mukasa, and Shaheed Qaasim for being my homies and holding such safe spaces for me as I explore who I am as a person. Your judgement-free accepting spaces have helped me grow so much. Katie, it has been a joy exploring the non-binary space with you. You remind me of all the ways I can be myself, and help me adventure thoroughly. Claire, #choochoo. Love you dearly, ride or die. Thank you for trusting me with your self and your being. I'm honored and I look forward to all our shenanigans to come. Daniel, it has been an absolute gift getting to know you over quarantine and finding such a

wonderful human to laugh with. I've loved every moment of or boba walks and conversations. Cheers to never being burnt-out again. Shaheed, our long phone calls are always a joy. I've appreciated our honest conversations exploring so many topics that are easy, and others that are hard. Thank you for always being honestly your self. You are an incredible human and I am so very grateful to call you my friend.

I would like to thank my quarantine bubble: Éowyn Lucas, David Cutler-Kreutz, and Logan Gloor. We made it through a wild year with an abundance of silliness and adventures, and I am so grateful to have us all on the dream quaran-team.

Academically, I have many people to thank. I'd like to thank Joerg Loeffler and Mihai Stoicha at ETH Zurich, and Jong Hyun Na at GMT for support on sample casting, as well as Celia Chari for SEM and Seola Lee for nanoindentation help during COVID. To the Johnson group alumni at Bill's retirement party, thank you for the many candid conversations about academia. This really helped me find that I wanted to pursue academia and that my approach was feasible. Dale Conner, thank you for reminding me to not make sure every box is checked before testing something, but also showing me that some of them should definitely be checked before testing something. Thank you to all the students I have mentored, for as I taught you, you have helped me learn more about myself. TMS conference colleagues and friends, our candid conversations have been brilliant. You are true wing-humans of academia.

To my Finland family, thank you for being my home and family. You all know how much my time in Finland meant to me, so you know I cannot possibly put it all into words. But I found my self there. I accepted my self there. And I felt so loved for being myself there. I miss you all so dearly and I'll see you soon.

To my wild Taco Tuesday homies, thank you for a regular dose of bi-weekly shenanigans and spontaneity. The silliness is an absolute joy every time, and we never cease to amaze me with the adventures we pursue.

The Caltech Y, to Greg and Agnes and JJ, thank you for hosting such a kind and wonderful space to explore leadership and the outdoors. Our many trips kept me grounded in my first few years and I will cary these memories with me as I continue through life. Thank you.

ABSTRACT

This thesis compiles three experimental works that provide evidence for distinct bulk metallic glass (BMG) phases across a range of kinetic fragilities. Motivated by An *et al.*'s computational discovery of a secondary heterogeneous glass phase in pure Ag and binary AgCu and CuZr, the thesis reports the distinct glass phases in the high and ultra-high fragile regime with a tunable $Pt_{80-X}Cu_XP_{20}$ system, and the kinetically strong $Ni_{71.4}Cr_{5.64}Nb_{3.46}P_{16.5}B_3$ (Ni208) BMG.

The high-fragility work utilizes direct measurement techniques for liquid configurational enthalpy as a function of temperature on anneal-equilibrated samples (Chapter 2). An apparent first-order glass-melting transition is revealed across kinetic fragilities ranging from $m = 60$ to over 90. The glass-melting temperature, T_{gm}, traverses up the ΔT region with increasing Cu content, X. A further experimental study of PtCuP explored the traditional and second glass phases to determine if they are in fact equivalent to the two glasses of An *et al.* (Chapter 3). Hardness data reveal that while the high-fragility samples grow the second glass during anneal, it forms in the ultra-fragile samples on quenching. Further, this apparent glass-melting transition is visible via traditional thermodynamic methods in ultra-fragile samples. For X = 20, where T_{gm} is in the inaccessible ΔT region, rapid capacitive discharge heating visualizes T_{gm} as well.

Investigation of a kinetically stronger Ni-based BMG connects the presence of the secondary glass to the embrittlement transition in Ni208 (Chapter 4). Inclusions are only present in embrittled samples, and are suppressed to lower temperatures when the initial melt is overheated above a critical toughening temperature. The inclusions show a heterogeneous structure and 30% increased hardness, similar to the computational Ag secondary glass phase.

These works provide compelling evidence for the existence of a secondary glass phase across the spectrum from strong to ultra-fragile glasses, and validates the initial computational discovery. This proves to be a significant work, as it presents direct experimental evidence of a novel phenomenon in metallic liquids, and presents a new solid-like glass phase.

PUBLISHED CONTENT AND CONTRIBUTIONS

[1] Qi An et al. "The L–G phase transition in binary Cu–Zr metallic liquids". In: *Physical Chemistry Chemical Physics* 24.1 (2022), pp. 497–506. ISSN: 1463-9076, 1463-9084. DOI: 10.1039/D1CP04157F. URL: http://xlink.rsc.org/?DOI=D1CP04157F (visited on 02/15/2022).
Sydney L. Corona contributed to the research discussions, conducted parallel experimental tests (pending publication), and supported writing and editing of the manuscript.

[2] Yidi Shen et al. "Shear Banding in Binary Cu-Zr Metallic Glass: Comparison of the G-Phase With L-Phase". In: *Frontiers in Materials* 9 (2022). ISSN: 2296-8016. URL: https://www.frontiersin.org/article/10.3389/fmats.2022.886788 (visited on 06/02/2022).
Sydney L. Corona contributed to the research discussions, conducted parallel experimental tests (pending publication), and supported writing and editing of the manuscript.

[3] Qi An et al. "The first order L-G phase transition in liquid Ag and Ag-Cu alloys is driven by deviatoric strain". In: *Scripta Materialia* 194 (Mar. 2021), p. 113695. ISSN: 13596462. DOI: 10.1016/j.scriptamat.2020.113695. URL: https://linkinghub.elsevier.com/retrieve/pii/S1359646220308174 (visited on 03/25/2021).
Sydney L. Corona contributed to the research discussions, conducted parallel experimental tests (pending publication), and supported writing and editing of the manuscript.

[4] Qi An et al. "First-Order Phase Transition in Liquid Ag to the Heterogeneous G-Phase". In: *The Journal of Physical Chemistry Letters* 11.3 (Feb. 6, 2020), pp. 632–645. ISSN: 1948-7185, 1948-7185. DOI: 10.1021/acs.jpclett.9b03699. URL: https://pubs.acs.org/doi/10.1021/acs.jpclett.9b03699 (visited on 06/06/2020).
Sydney L. Corona contributed to the research discussions, conducted parallel experimental tests (pending publication), and supported writing and editing of the manuscript.

[5] Qi An et al. "Formation of two glass phases in binary Cu-Ag liquid". In: *Acta Materialia* 195 (Aug. 2020), pp. 274–281. ISSN: 13596454. DOI: 10.1016/j.actamat.2020.05.060. URL: https://linkinghub.elsevier.com/retrieve/pii/S1359645420304079 (visited on 07/13/2020).
Sydney L. Corona contributed to the research discussions, conducted parallel experimental tests (pending publication), and supported writing and editing of the manuscript.

[6] Jong H. Na et al. "Observation of an apparent first-order glass transition in ultrafragile Pt–Cu–P bulk metallic glasses". In: *Proceedings of the National*

TABLE OF CONTENTS

LIST OF ILLUSTRATIONS

LIST OF TABLES

Chapter 1

THE HISTORY AND EVOLUTION OF BULK METALLIC GLASS

1.1 Metallic Glass and the Bulk Form

Traditionally, metals are ordered and crystalline, while disordered glasses are polymeric, molecular, or inorganic compounds such as oxides, chalcogenides, etc. Bulk metallic glasses (BMGs), however, are amorphous metal alloys, and were the first materials to bridge this gap. They extend metallic alloys to the amorphous state, and emerge with beneficial properties from each. The first metallic glass was achieved in 1960, when Duwez reported a Au-Si alloy that was splat quenched at 10^5 - 10^8 K/s, yielding an amorphous foil ~10-μm thick.[1, 2, 3, 4] This first amorphous metallic alloy would begin a new field of research; Metallic Glass (MG), and later, with slower cooled samples on the millimeter scale, Bulk Metallic Glass (BMG).

To achieve a successful BMG, relatively rapid quenching of the molten alloy is utilized to circumvent its natural tendency toward rapid crystallization. During quenching, the molten alloy must pass rapidly through a thermodynamic regime (Figure 1.1) where the liquid is metastable.[5] The sample must be undercooled below its equilibrium melting temperature or liquidus temperature, T_l , in the case of an alloy, while remaining in the liquid phase. This regime is termed the Super-Cooled Liquid (SCL). The SCL alloy is then cooled until atomic motion is arrested, and a configurationally frozen liquid or amorphous phase is achieved below the glass transition (T_g). Through the SCL, crystallization must be bypassed prior to
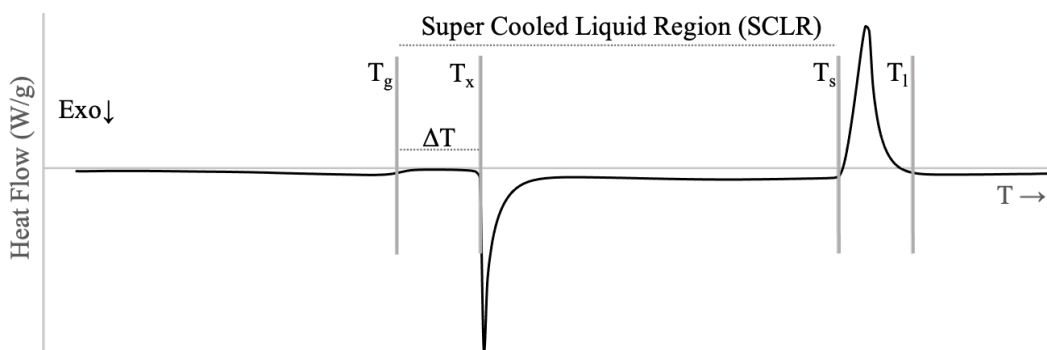
Figure 1.1: Representative thermal scan depicting characteristic transitions in BMGs.
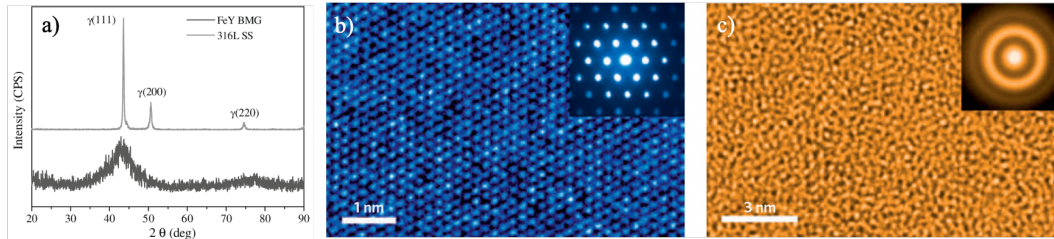
Figure 1.2: Visualization of ordered vs. disordered characteristics. a) Representative X-ray diffraction patterns for crystalline (top) and amorphous (bottom) material. TEM image and electron diffraction for an ordered material (b) and a metallic glass (c). Reproduced from Wang *et al.* (a) [6], and Jafary-Zadeh *et al.* (b,c) [7]. For b and c, copyright © 2018 by the authors. Licensee MDPI, Basel, Switzerland. This article is an open access article distributed under the terms and conditions of the Creative Commons Attribution (CC BY) license (http://creativecommons.org/licenses/by/4.0/)

arriving at the glass transition.

Once cast to below T_g, the sample requires verification of its amorphous structure and lack of long-range order. This is most commonly displayed in X-Ray Diffractometer (XRD) scans and diffraction patterns by a broad diffraction band in place of crystalline peaks. High resolution Transmission Electron Microscopy (TEM) images are often used to visualize the presence or absence of atomic order. Figure 1.2a displays representative crystalline (top) and amorphous (bottom) XRD scans, while Figures 1.2b and 1.2c show typical TEM and electron diffraction for ordered and amorphous materials, respectively.[6, 7] From diffraction patterns, one can compute Radial Distribution Functions (RDFs) that report the distribution of atomic neighbor distances between pairs of atoms. The absence of periodicity (peaks) implies a lack of long range atomic order.

Metallic Glass Characteristics: Thermal and Mechanical Properties

Once quenched to ambient temperature, BMGs display characteristic thermal events on subsequent reheating from the glassy state (Figure 1.1).

In typical glasses, on passing through the Glass Transition Temperature, T_g, there is an endothermic increase in heat capacity accompanied by a change in the volume thermal expansion coefficient. T_g is traditionally defined as the temperature where the observed viscosity reaches 10^{12} Pa-s or 10^{13} Poise during cooling (or heating). Above T_g, atoms (or molecules) display increased mobility and the liquid exhibits the ability to "flow" under stress. It transitions from solid-like to fluid-like behavior.[8]

Above T_g, liquid fluidity increases rapidly (by orders of magnitude) over a narrow range of temperature. This temperature regime is utilized to reshape the material and produce net-shape parts as is done in glass blowing, blow molding, or injection molding.[5] The viscosity of 10^{12} Pa-s (often taken to define T_g) corresponds to the typical softening point of silicate glasses above which glass blowing can be implemented.[8]

Similar to other glass systems, BMGs can be formed and reshaped as temperature increases above the glass transition. However, given their metallic nature, there are marked differences. First, the glass transition of MGs occurs over a wide range of temperatures; T_g ranges from room temperature (e.g., for the Duwez Au-Si metallic glass) to as high as ~800 K for MGs based on refractory metals.[9, 10] This compares, for example, to a lower and smaller range of 60 - 500 K for traditional molecular and polymeric glasses.[11, 12] Second, while the glass transition is present across all glass systems, BMGs tend to crystallize more readily and undergo an accompanying distinct thermal event before melting; recalescence. Recalescence is an exothermic heat release from the relatively sudden atomic rearrangement from the liquid to crystalline phase transition. This occurs at a temperature designated as T_x.

Many traditional glasses exhibit very sluggish crystallization kinetics and display no distinct exothermic event or well-defined T_x. The region of liquid metastability during heating, $\Delta T = T_x - T_g$, thus tends to be smaller for BMGs than for many polymer, molecular, or silicate glasses, where crystallization often does not occur on any practical laboratory time scale between T_g and T_m. The relevant transitions and temperature regimes are illustrated by a representative BMG Differential Scanning Calorimeter (DSC) trace as shown in Figure 1.1.

Metallic Glasses exhibit certain unusual mechanical properties compared with traditional glasses and crystalline metals. For example, they have typical tensile strength several times greater than steel and other crystalline engineering metals. This is presumed to be due to the absence of dislocations and other extended defects that are responsible for plastic yielding and deformation in the case of crystalline metals. Metallic glasses deform by stress-induced activation of nano-meter scale local soft regions called shear transformation zones.[13, 14] Below T_g, deformation tends to become spatially localized and concentrated into bands called shear bands. The formation and operation of these shear bands under stress is the primary mechanism of plastic deformation in MGs. Unlike molecular and oxide glasses, MGs may ex-

hibit significant ductility under certain loading conditions such as compression and bending. In this case, one observes formation and operation of many shear bands throughout a macroscopic sample. In contrast, MGs exhibit little or no ductility in unconfined loading conditions such as pure tension. In a tensile test, metallic glasses tend to fail along a single narrow shear band inclined at an angle of 45 degrees with respect to the tensile axis. The fracture toughness (K_C) of metallic glasses is reported to vary over an extremely wide range from that of very brittle silicate glasses ($K_C \sim 1\ MPa - m^{1/2}$) to as high as that of tough steels ($K_C \sim 100\ MPa - m^{1/2}$).[15] Above T_g, flow becomes delocalized and homogeneous much like flow in an ordinary liquid, albeit with a high viscosity. In this regime above T_g, metallic glasses can be shaped and formed in the same manner as thermoplastics.[2, 16, 17, 18]

In summary, while MGs offer distinct improvements over traditional metals such as very high strength, they may also exhibit limited toughness and ductility, and ultimately experience catastrophic brittle failure; e.g., in tension. The tendency to crystallize easily in the supercooled liquid region means that relatively high cooling rates from the molten state are required to produced BMGs. The requirement for rapid cooling in turn limits the maximum dimensions of BMGs due to ability to extract heat on quenching. In practice, BMGs are limited to cast rods of diameter in the mm to cm range, or thin plates of similar thicknesses (Section 1.3). So similar to traditional metallurgy, much research in the field of BMGs is directed to addressing these limitations. Alloy development pursued the discovery of alloys that have greater resistance to crystallization, and that exhibit enhanced toughness and ductility, or other desirable attributes. Other areas of active study include oxidation resistance, magnetism, and ferromagnetism. Further, studies of BMG composites address brittle failure by utilizing crystalline dendrites in an amorphous matrix to arrest crack growth. This has resulted in increasing fracture toughness ten-fold.[19]

This unusual combination of properties motivated research to investigate their fundamental origins. The remaining sections of this chapter outline the applications, underlying physics, formation criteria, and casting methods that took BMGs from microns thick to the bulk scale as Bulk Metallic Glass (BMG).

Applications
Following BMG discovery, many applications were explored. These applications span commercial and research sectors. Examples are included in Figure 1.3.
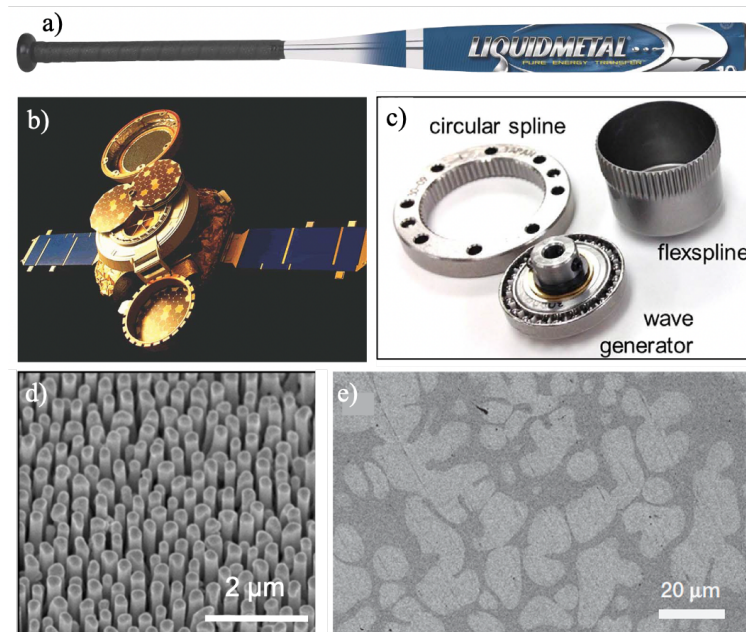
Figure 1.3: Visualization of select applications. a) A BMG-coated baseball bat by LiquidMetal Technologies [5], b) a BMG disc on the Genesis Mission as a solar wind collector [5], c) BMG flex splines for strain wave gears [20], d) thermoplastic formed BMG nano-rod for a subcutaneous blood glucose sensor [21], and e) a BMG matrix composite for increased toughness [22]. All images reproduced with permission. Image d: Reprinted with permission from [21]. Copyright 2017 American Chemical Society.

In the commercial sector, applications have been explored in sporting goods, consumer electronics, and medical applications.[5] Sporting equipment has included golf clubs, baseball bats, and tennis rackets with BMG coatings or frames. Consumer electronics applications have included injection molded and die-cast phone frames and casings for increased scratch, water, and dent resistance. In orthodontics, fabrication of dental brackets and appliances is being explored.

In the research sector, a Zr-based BMG was used as a collection device for the solar wind on the 2001 NASA Genesis Discovery mission.[23] The "flow" characteristics of BMGs have led to its use in additive manufacturing. NASA JPL has used cast net-shaped BMG strain wave gears for precision robotics on rovers for improved wear resistance.[20] Metallic glasses are an improved material for gearbox flexsplines due to BMG embrittlement resistance at the low temperatures encountered in space applications.[20]

When BMGs first emerged, it was hypothesized that a stronger, tougher, general-

use glassy "steel" was possible. But as time progressed and research developed, the most successful pursuits arose when BMG compositions and properties were tuned and selected *specifically* to meet particular goals and specifications in "niche" applications. For example, the most common and processable BMG alloys to date are the Zr-, Fe-, and Pt-based alloy families. Zr-BMGs (e.g., Vitreloy alloys) are the most widely studied BMG system and have the most widespread structural applications, while ferromagnetic Fe-base BMGs have been adopted in widespread use as soft magnetic materials in inductors and transformer cores, and Pt-based amorphous alloys have been used as a catalyst site for subcutaneous blood glucose sensors, to name a few niche applications.[24, 25, 21]

Since fine tuning of properties of BMGs is where they provide the greatest benefits, Section 1.3 describes how fundamental research developed standardized rules and procedures for achieving and identifying good metallic glass formers with desirable properties. These approaches, similar to applications, were informed by combining theories and methods of both crystalline metals and traditional amorphous materials. But to fully understand BMG casting, these theories and methods are first described in Section 1.2 below.

1.2 Classical Theory for Bulk Metallic Glass

Periodicity in *ordered* materials permits simplifying models and assumptions in theory development. These theories have underlain the advancement of our understanding of periodic crystalline materials in a broad range of fields; e.g., semiconductors, structural materials, Bloch's theorem, etc.[26] Glasses in general and BMGs in particular — without long-range atomic order — do not lend themselves to such simplifications. A microscopic theory of the statistical mechanics of glasses has been developed based on the concept of potential energy landscapes (PELs). The PEL theory provides a microscopic basis for understanding the thermodynamic, kinetic, and physical properties of glasses. The basic results of PEL theory provide the basis for much of the work on metallic glasses in the present thesis. As such, it is important to provide an outline of the basic theory.

Potential Energy Landscape Description of Bulk Metallic Glass

Metallic glasses are described energetically by a Potential Energy Landscape (PEL). A PEL provides a topographic view of all the accessible potential energy states across a system of interacting particles (Figure 1.4). This potential energy is a function
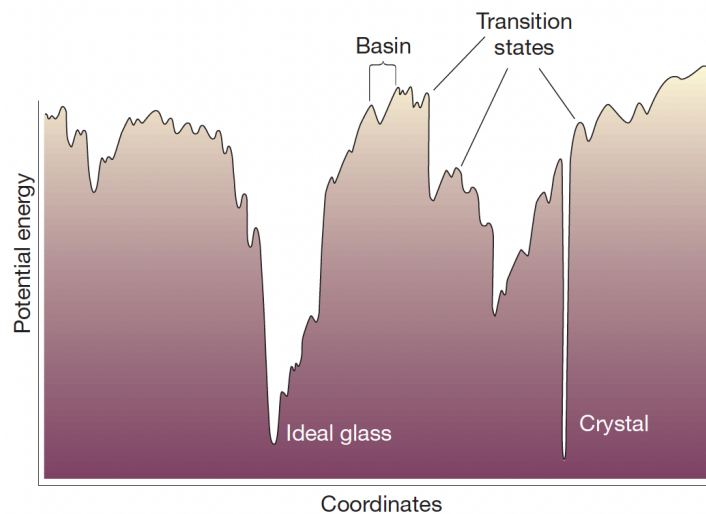
Figure 1.4: Representative PEL. Reproduced with permission from [28].

of the 3N atomic coordinates of all the atoms that comprise the system. These energies arise from pair interactions (or more generally, many-body interactions) between atoms, where the total potential energy is the sum of these interactions across all atomic pairs. Varied local environments and configurations yield different potential energies. A stable atomic arrangement corresponds to a local minimum in the overall potential energy whereby the force on each atom is zero. Such a local potential energy minimum is referred to as an inherent state (i.e., a state of energy in a 3N particle system) of the liquid/glass. Therefore, specific stable atomic configurations described by these minima are referred to as the inherent states of the PEL; where crystal atomic configurations have deeper wells and greater stability compared to typical amorphous inherent state structures.[27]

Movement around the PEL can be described as a sequence of transitions from one inherent state to another; excitations.[27, 29, 28] Elementary excitations over potential energy barriers move a system between its inherent state energy wells in the PEL. They allow for inter-basin hopping between the local minima, but are not energetic enough to move the system from a liquid inherent state to a crystalline state; relaxations discussed further in Section 1.2: Kinetic Behavior in the PEL, Relaxations. Glasses and liquids utilize this inter-basin hopping to achieve their characteristic configurational changes associated with flow. Upon heating above T_g, enough thermal energy is available to allow inter-basin hopping and internal movement between amorphous/liquid inherent states, but not enough to access a crystalline state or to access the higher energy states of a liquid above its melting

points (melting basin depth not shown in Figure 1.4).

In addition to PEL theory's effective description of the energetics of atomic configurations, it can be combined with statistical mechanics to determine thermodynamic state variables such as energy. It can be further refined by assuming separability of vibrational and configurational components for a more specific analysis, as discussed below.

Thermodynamic Application of PEL: Separable Configurational and Vibrational Components via the Canonical Ensemble

A key feature of PEL theory is that it allows for separation of configurational and vibrational components in thermodynamic functions. This occurs through a number of steps. First, with a PEL, a distribution of occupied inherent energy states is required to describe a system. A statistical distribution is chosen to describe the density of states (DOS); e.g., Gaussian, exponential, etc. Second, a partition function ($\mathbb{Z}$) is required. $\mathbb{Z}$ is a function of temperature and microstate energies as a model of microscopic constituents of a system; i.e., number of particles, volume, particle mass. It relates these microscopic details to thermal quantities through its logarithmic derivatives. Third, the partition function type is selected. For this work, a canonical partition function is of practical use. The canonical partition function comes from the canonical ensemble that allows environmental heat exchange at fixed number of particles, volume, and temperature (the NVT ensemble). This applies to equilibrium conditions of BMGs at fixed T and is therefore useful here.

Combining these criteria, a distribution-defined DOS and the Canonical $\mathbb{Z}$, the resultant separation is described through an example derivation of free energy, F.

Separability is achieved via the canonical approach to the partition function — where taking the log of the partition function for the Helmholtz free energy yields a sum of the exponential components (the log of factors is a sum); demonstrated below.

Separability arises from the derivative of

$$F = -kT \ln{(\mathbb{Z})}, \tag{1.1}$$

where $\mathbb{Z}$ is the canonical partition function with a DOS coefficient;

$$\mathbb{Z} = \int D(E) \exp\left[\frac{-E}{kT}\right] dE. \tag{1.2}$$

with E the energy of the system. When E is represented by a sum of its configurational and vibrational parts, the following results:

$$E = E_{Config} + E_{vib,har} + E_{vib,anh},$$ (1.3)

where vibrational energies are further divided into harmonic and non-harmonic components.

When combining equations 1.1 - 1.3,

$$F = -kTln\left(\int D(E)\exp\left[\frac{-(E_{Config} + E_{vib,har} + E_{vib,anh})}{kT}\right] dE\right)$$ (1.4)

and using exponential and log manipulations

$$e^{x+y} = e^x \cdot e^y$$ (1.5)

$$ln(e^{x+y}) = ln(e^x \cdot e^y)$$ (1.6)

$$ln(a \cdot b) = ln(a) + ln(b)$$ (1.7)

$$ln(e^x \cdot e^y) = ln(e^x) + ln(e^y) = x + y$$ (1.8)

the thermodynamic functions emerge with distinguishable contributions from configurational and vibrational parts, and can be treated individually;

$$F = -kTln\left(\int D(E)\exp\left[\frac{-E_{Config}}{kT}\right]\exp\left[\frac{-E_{vib,har}}{kT}\right]\exp\left[\frac{-E_{vib,anh}}{kT}\right] dE\right).$$ (1.9)

While possible in this mathematical example, this separability is backed by theory and experimental evidence as well.

For the separable behavior, a key underlying assumption is that the average vibrational DOS does not depend on the energy of an inherent state minima. Thereby anharmonicity is avoided and the anharmonic approximation is not needed. This separation of vibrations from energy dependence allows for the decoupling of the vibrational and configurational parts from the canonical partition function, and full separation is possible come manipulation for the Helmholtz free energy.

For experimental evidence, Smith *et al.* reported direct *in-situ* measurements of the vibrational spectra of strong and fragile metallic glasses in the amorphous, liquid,

and crystalline phases in the vicinity of T_g. For both strong and fragile glasses, less than 5% of the total excess vibrational entropy was found in the glass and liquid phases over the crystal.[30] This provides experimental evidence that the excess entropy of metallic glasses is almost entirely configurational in origin, validating early theories that the glass transition is purely configurational.[31]

Through PEL assumptions, once separated, these components can be treated and analyzed independently.

Vibrational Component

The vibrational component is characterized by phonon frequencies and the phonon density of states. In the PEL, phonon frequencies arise from the curvature in the landscape along the various directions of the configuration space surrounding the local potential energy minimum. For 3N particles, there are 3N-6 independent configurational coordinates (the 6 degrees of freedom associated with center of mass motion and system rotation are not vibrational degrees of freedom). This curvature matrix is the second derivatives of the PE with respect to the coordinates (x_i, y_i, z_i where "i" labels particles) and can be described as a dynamic matrix. Through analysis of this matrix via diagonalization and eigenvalue determination, one attains the normal modes and phonon DOS, respectively. In effect, the phonon frequencies go to zero when the curvature of the PEL goes to zero (an inflection point).[28] From the phonon DOS, the phonon free energy and vibrational entropy are defined as seen in Smith *et al.*[30]

With the vibrational component separated and a focus drawn to phonons, this can be used, for example, to deduce the sound velocity in a material. The sound velocity of long wavelength phonons is determined by elastic constants. Sound velocities can be measured using ultrasonic transducers where the long wavelength vibrational modes are sampled, and elastic constants calculated. Elastic constants are represented by phonons that collectively move large groups of atoms in phase space. While useful, the separated vibrational component will not be addressed in this work. In effect, the configurational component takes focus, and experiments to determine the configurational contribution to the free energy are explored in Chapter 2 of the thesis.

Configurational Component

In the PEL, the configurational part of the partition function is a sum of configurational energies over all minima. When separable from vibrations, and as seen in

work by Smith *et al.*, the glass transition at T_g is described as a purely configurational event. Thus, if heated from a relaxed glass state, the resulting enthalpy associated with the glass transition is purely configurational.

When isolated from the vibrational component, the configurational enthalpy is actually representative of the potential energy of the system. This is achieved since all of the experiments are done at ambient pressure. Strictly speaking, specific enthalpy $h = e + pv$, and changes in specific enthalpy (with respect to a reference state) can be expressed as $\Delta h = \Delta e + p\Delta v$.[32] In our experiments at ambient p, the $p\Delta v$ term can be shown to be very small compared with Δe. As such, $\Delta h \sim \Delta e$ can be shown to be an excellent approximation (i.e., $p\Delta v$ is on the order of 10^{-3} compared to measured $d\Delta h$ values (Chapter 2). So $p\Delta v$ is neglectable to an accuracy of 0.1% or better. Assuming using all of v, where Δv is actually 10^{-2} of v.) In equilibrium at fixed T, kinetic energy is simply 1/2kT per degree of freedom. It follows that changes in configurational enthalpy (with respect to a reference state at fixed T) are equivalent to changes in the specific configurational potential energy of the system. This equivalence will be important throughout the discussion presented in Chapter 2 and is described in further detail in Appendix B.1.

A Gaussian Landscape and Thermodynamic Functions

The PEL is particularly useful for defining thermodynamic functions of amorphous materials. A widely used approach assumes a lack of energetic preference for atomic interactions or configurations. This results in a random spatial distribution of atomic configurations and random atomic interactions. Basically, the energy of inherent states is assumed to arise from a sum of random variables. This naturally gives rise to a Gaussian density of states (DOS) to represent the distribution of energies for the inherent state minima.[27, 28] When applied to the canonical partition function, this yields an integral over a Gaussian distribution. The derivation from the Gaussian DOS in the canonical partition function to the Helmholtz free energy (F), entropy (S), internal energy (U), enthalpy (H), and heat capacity (C_P) are carried out and described in Appendix A, and are summarized below.

$$F = +kT \ln \sqrt{2}\sigma - \frac{\sigma^4}{kT} \tag{1.10}$$

$$S = -k \ln\left(\sqrt{2}\sigma\right) - \frac{\sigma^4}{kT^2} \tag{1.11}$$

$$U = \gamma - \frac{2\sigma^4}{kT} \tag{1.12}$$

$$H = U = \gamma - \frac{2\sigma^4}{kT} \tag{1.13}$$

$$C_P = \frac{dU}{dT} = \gamma + \frac{2\sigma^2}{kT^2} \tag{1.14}$$

When applying the Gaussian DOS for the configurational contribution, the resulting equations for the total crystal and liquid heat capacities (configurational + vibrational contributions) are:

$$C_{P,x}(T) = 3R + aT + bT^2 \tag{1.15}$$

$$C_{P,l}(T) = 3R + cT + dT^{-2} \tag{1.16}$$

where 3R is the Dulong-Petit heat capacity, and the components with a, b, and c coefficients are anharmonic contributions. Within the liquid heat capacity equation there is a liquid-specific configurational term, "dT^{-2}," that arises from the Gaussian density of states assumption in the Gaussian Landscape Model; the last term of Equation 1.14.

Figure 1.5a fits experimental heat capacity with Equations 1.15 and 1.16. Assuming sufficient fit, enthalpy (Equation 1.13) and entropy (Equation 1.11) are plotted in Figure 1.5b and c, respectively. When inspecting the total entropy curve, an interesting phenomena appears; the Kauzmann Paradox. The Kauzmann Paradox arises in thermodynamic glass physics when comparing the total entropy of a liquid and crystal. At absolute zero, T = 0 K, the entropy of a solid phase should approach zero (Third Law of Thermodynamics). However, as seen in Figure 1.5c, when projected to 0 K, the SCL entropy extends below zero to negative values. Ostensibly, the liquid entropy would become negative and non-physical. But experimentally, the system arrests to a glass before this occurs. To this end, it is hypothesized the glass transition exists to circumvent this thermodynamic paradox. We discuss this apparent paradox in Chapter 2.

PEL theory provides a helpful picture to understand energetic states of glasses. But while providing a classical and fundamental approach to BMG thermodynamics, the Gaussian assumption leads to compounding problems as will be seen below.
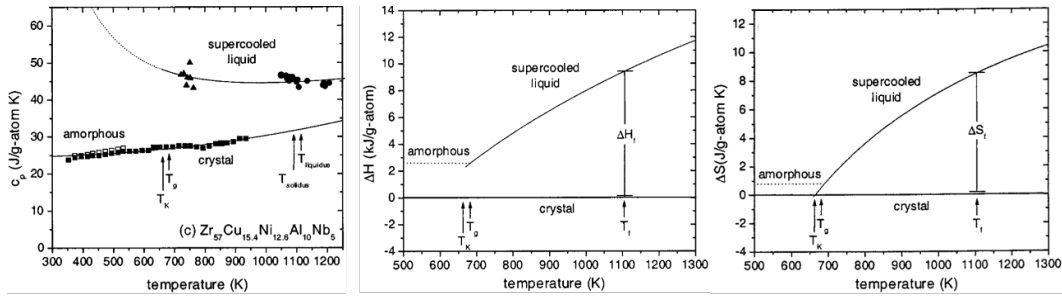
Figure 1.5: Thermodynamic Functions via the Gaussian Landscape. Heat capacity, enthalpy, and entropy are plotted in the first, second, and third components, respectively. Reprinted from [33] with the permission of AIP Publishing.

Issues Arise with the Gaussian Landscape

Upon greater inspection, the assumed Gaussian distribution of filled energy states is not representative of a glass system. This simplification describes the local potential energy distribution about each atom by assuming both a random spatial distribution and random interactions around the given atom. The resulting summation over multiple random atomic interactions leads to an assumption that the distribution is Gaussian at all energies. However, with these assumptions, multiple issues arise. In reality, a preferred and known absolute minimum is introduced at low temperatures; the crystalline state. Therefore, the potential energy of a configurational state must be bounded below, whereas a Gaussian distribution has no absolute lower bound. And while Equation 1.15 fits the glass and crystal heat capacity data (at temperatures where data are available) in Figure 1.5a, the SCL data varies widely from Equation 1.16 at low temperatures. The resultant T^{-2} dependence from a Gaussian DOS heat capacity induces a sharp upward curvature at low temperatures that does not well describe the SCL data.

Further compounding this issue of an approximate model, are inaccurate data. This data inaccuracy is three-fold. First, given BMGs have higher transition temperatures than traditional glasses, a Differential Thermal Analyzer (DTA) with a higher temperature range is necessary for measuring heat capacity, enthalpy, and related variables. Traditional glasses use a Differential Scanning Calorimeter (DSC), and this instrument reports high-quality heat capacity data which are then used to calculate further thermodynamic functions. This approach has been taken with BMGs using a DTA, but the different measurement method makes this more difficult and less accurate near T_g (Step Calorimetry). Choosing to measure heat capacity with a DTA leads to error, whereas directly reporting enthalpy is more accurate for this

apparatus. Thus, direct reporting enthalpy and calculating to heat capacity (by differentiation) is a necessary adjustment with a DTA.

Second, with the configurational dependence of glasses more recently established in 2017, the data in Figure 1.5 did not prioritize achieving a well-defined reference state. Without this reference state prior to measurement, each data point had a different energetic baseline value — leading to the wide vertical spread of SCL data in Figure 1.5a. Utilizing annealing for configurational and energy equilibration will lead to more consistent and precise measurements.

Third, for metallic glasses, there are limited data in the mid-range SCL due to the intervention by rapid crystallization. Additional data in this region could inform the proper curvature of the heat capacity equation. This region is particularly elusive to data measurement due to the center of the SCL having limited access from both above (under cooling below T_l), and from below (heating above T_g). Moving too far into this region for long times yields crystallization. Thus, a new method was required with heating rate, data sampling rate, and accuracy capable of acquiring data in this inaccessible region; to heat/cool and measure the material response before crystallization. In 2011, Rapid Capacitive Discharge Heating (RDH) was developed for this purpose. Since its inception, RDH has informed this data region for a number of alloys, and contributes to Chapter 2.[34, 35, 36]

These three shortcomings compound and create challenges when attempting to validate a Gaussian landscape model. There is the potential that the Gaussian DOS assumption leads to an apparent Kauzmann paradox as either an artifact of the failed Gaussian landscape model or from insufficient data to assess the model. As such, an improved experimental approach is required to properly assess the theory. The acquisition of better experimental data along with a test of the theory are explored in Chapter 2.

Kinetic Behavior in the PEL, Relaxations

Recalling the initial introduction of the PEL model, the energetics of atomic configurations were discussed, and the transitions between inherent states through excitations and relaxations were first introduced. This section will elaborate on these relaxations as how they enable sample equilibration.

In glass physics, atomic rearrangement has different features over key temperature regimes; the super cooled liquid and solidified glass. As determined by Johari and Goldstein, there are two distinguishable types of relaxations deemed α- and

β-relaxations.[37] α-relaxations (Maxwell relaxations) are primary relaxations associated with the irreversible rearrangement of atomic clusters. They describe atomic motion at higher temperatures, are non-Arrhenius, and describe vitrification and atomic motion arrest at T_g. α-relaxations are frozen-out below T_g, while β-relaxations remain operative. β-relaxations are secondary relaxations that describe more limited atomic motion that persists at lower temperatures. Such limited motion is often described as the rattling of the "cage" or "cage rattling" of neighboring atoms surrounding a given atom.[38] These β-relaxations tend to be more Arrhenius in character. With respect to the PEL, α- and β-relaxations both relate to movement between energy wells. Movements energetic enough to produce permutations of neighboring atom pairs are referred to as inter-basin hopping and are α-relaxations, while lower-energy intra-basin hopping between shallower local minima within a larger megabasin are β-relaxations. A series of β-relaxations may lead to less frequent α-relaxations.[39]

Both α- and β-relaxations are important to this discussion of structure and configuration because they enable structural rearrangements occurring at different temperatures. Annealing at or below T_g allows β-relaxations to occur without crystallizing. The active β-relaxations allow the glass to sample local regions of its state space to find a low-energy minima amongst the amorphous inherent structures. For anneals above T_g, α-relaxations take over and the material will ultimately crystallize given sufficient time dependent on the degree of atomic motion in the system. This time duration describes the metastability of the glass state. Metastability is relative to the relaxation time for configurational degrees of freedom. It can be quantified by the ratio of the time to crystallization to the Maxwell (configurational) α-relaxation time, $\tau_\alpha = \tau_M$. This ratio quantifies the ability of the glass sample to achieve configurational equilibrium prior to crystallization. It characterizes configurational equilibration of the glassy state, and therefore describes the applicability of thermodynamics. The Maxwell relaxation time near T_g is typically ~10 - 100 s and decreases rapidly with temperature above T_g.

The accessibility of both relaxations determines atomic mobility in the glassy/liquid states.[27] This in turn is related to Angell's Kinetic Fragility of the liquid, and is discussed below.
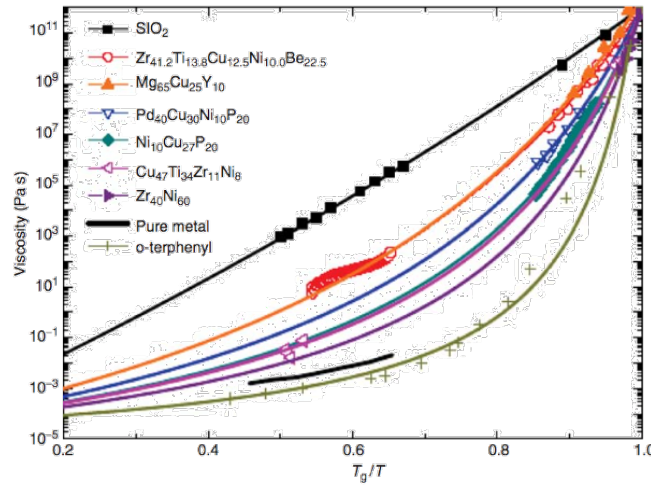
Figure 1.6: Angell Plot: Log Viscosity vs. normalized temperature. The slope as T_g is approached upon cooling indicates the Angell fragility parameter, m. Reprinted with permission from [40].

Kinetic (Angell) Fragility and Glass Quality

Kinetic (Angell) Fragility describes the rate of increase of atomic mobility as temperature increases above the glass transition temperature. It is closely correlated with the *deviation* of viscosity *from* simple thermally activated Arrhenius behavior. Arrhenius behavior (of atomic mobility or atomic diffusion) is characterized by a single activation energy:

$$k(T) = A \exp\left(\frac{-E_a}{RT}\right) \tag{1.17}$$

and viscosity, η:

$$\eta = A \exp\left(\frac{E_a}{k_B T}\right) \tag{1.18}$$

where k, R, A, E_a, k_B, and T are respectively the rate constant, universal gas constant, pre-exponential factor, activation energy, Boltzmann constant, and absolute temperature in Kelvin.[1, 41] In Figure 1.6, Arrhenius behavior corresponds to a straight line, whereas actual liquid viscosities exhibit an increasing curvature and deviation from an Arrhenius law. The Angell fragility parameter, m, quantifies this deviation and is defined as the slope of each curve as the glass transition is approached from above (Figure 1.6). Angell defined m as:

$$m = \left(\frac{\delta \log_{10} \eta}{\delta(T_g/T)} \right)_{T-T_g} \qquad (1.19)$$

and describes the extent of atomic diffusion near the glass transition via the derivative of the logarithm of viscosity with respect to (T_g/T).[2, 1]

Liquid fragility m plays a critical role in successful vitrification of a liquid.[8] "Strong" liquids with typical m < 50 have limited atomic mobility in the SCL region, and therefore often readily freeze into an amorphous phase. Their sluggish kinetics tend to yield lower critical cooling rates for glass formation that are advantageous for casting bulk samples, millimeters or centimeters in dimension. Most early BMG research focused on strong glass-forming liquids, and data for such systems dominate the metallic glass literature. However, "fragile" glass-forming liquids with typical m > 60 tend to crystallize more rapidly in the SCL region and therefore tend to be poor glass formers. They generally require higher critical cooling rates than can be achieved by common quenching methods, and therefore sample dimensions tend to be limited. Fragile glasses tend to crystallize more readily on reheating above T_g and thus require additional care in casting and testing. As such, published physical property data on fragile liquid glass formers are limited and such liquids have thus far been poorly characterized.[19]

Classical Theory Summary

The combination of metal and glass physics creates a multifaceted and interdisciplinary foundation. The PEL informs thermodynamic models, albeit with some drawbacks. There remain possible improvements in thermodynamic models and data collection, potentially in the elusive high-fragility regime. Even so, these foundations inform casting requirements and parameters such as composition and chemistry, thermodynamic and kinetic quenching conditions, methods, and more as described in the next section.

1.3 Formation Criteria

Casting a successful BMG requires fine chemical, thermodynamic, and kinetic control. This combines the traditional metallurgy and traditional glass physics established above. These controls summarized succinctly, BMGs are metal alloys that are quenched from the melt such that crystallization is avoided and the product is retained in the meta-stable amorphous state.
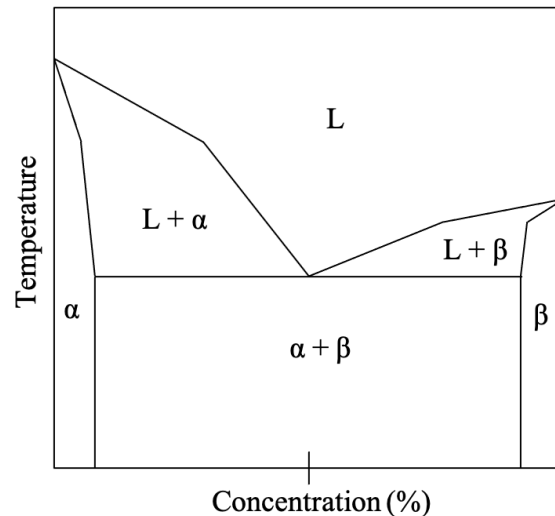
Figure 1.7: Representative Eutectic Diagram.

Chemistry Controls

In 2000, three factors were identified that inhibit crystallization for BMG formation; 1) multicomponent alloys of at least three elements, 2) atomic size mismatch of over 12% in the constituent atoms, and 3) negative heats of mixing between the three primary elements.[42, 43, 44] These factors stem from the "confusion" principle, preventing ease of atomic ordering, and energetic favoring of the liquid over the crystalline state, respectively. To promote application-specific properties in the cast glass, these factors prove useful. For example, one might emphasize an element, say Fe, for its magnetic properties. From there, adding two or more metallic elements or nonmetals with features that promote glass formation (e.g., useful atomic size mismatch or negative heats of mixing with Fe) provides a practical basis. However, while these rules are a useful starting point, many additional considerations are necessary for developing promising alloys for BMG formation.

Thermodynamic Factors — Eutectics

From a thermodynamic point of view, vitrification requires a quench of the over-heated alloy melt. The melt must be cooled through the supercooled region below the liquidus/solidus temperature, and down to the glass transition temperature before crystallization can occur, effectively freezing the atomic liquid in place as a glassy solid. Essentially, the undercooled liquid must be frozen while avoiding the nucleation and growth of crystalline phases.

In a typical phase diagram, this quench follows a vertical downward path from the equilibrium liquid to the low-temperature amorphous solid.[45] Below the liquidus curve, (T_l), the driving force for crystallization increases monotonically with undercooling $T_l - T$. Crystallization results in a drop in free energy which increases with the degree of undercooling $T_l - T$ until one reaches an undercooling $T_l - T_g$ at the glass transition. In a eutectic phase diagram, the eutectic composition has a characteristically depressed liquidus temperature compared to the melting points of the atomic constituents (Figure 1.7). Turnbull first pointed out the importance of the ratio T_g/T_l in achieving glass formation. In the literature, this ratio is referred to as the reduced glass transition temperature or Turnbull's parameter, t_{rg}. He noted that at a eutectic composition, this ratio tends to display a maximum (versus composition). Further, he pointed out that when this ratio reaches a critical value of ~2/3, easy glass formation is to be expected. This is now referred to as Turnbull's criterion.[8]

It is now well established that vitrification of metallic alloys is most easily achieved in multicomponent alloys with compositions located near deep eutectic features in the alloy phase diagrams. When choosing between eutectic systems, deeper eutectics where T_g/T_l exceeds ~0.6 have been found to allow for more stable undercooling of the liquid and easy formation of BMGs. Although not a strict rule, the Turnbull criterion is generally a useful and simple predictor of glass forming ability in metallic systems. The alloys discussed in this thesis are excellent examples of deep eutectic alloys where $t_r \sim 0.6$ or greater.

Kinetic Controls

When quenching an alloy from temperatures above melting, a crystal forms if the material is not cooled at a sufficient rate to beat crystallization. The kinetic aspects of glass formation are described by a Temperature-Time-Transformation (TTT) diagram. TTT diagrams show the kinetics of crystallization in a 2-dimensional space of temperature and log time (Figure 1.8). With respect to temperature, the resultant phases are broken into four zones — Liquid, Supercooled Liquid (SCL), and Glass, with Crystals grown in the SCL given sufficient time. The curved border between the SCL and crystal is referred to as the "crystallization nose" or "nose."[34]

At time zero, at the top left of Figure 1.8, two overall behaviors emerge, i) the melt is quenched fast enough such that crystallization is fully avoided and the sample is successfully vitrified (Figure 1.8; $-\dot{T}_{glass}$), or ii) any quench rate eclipsed by the
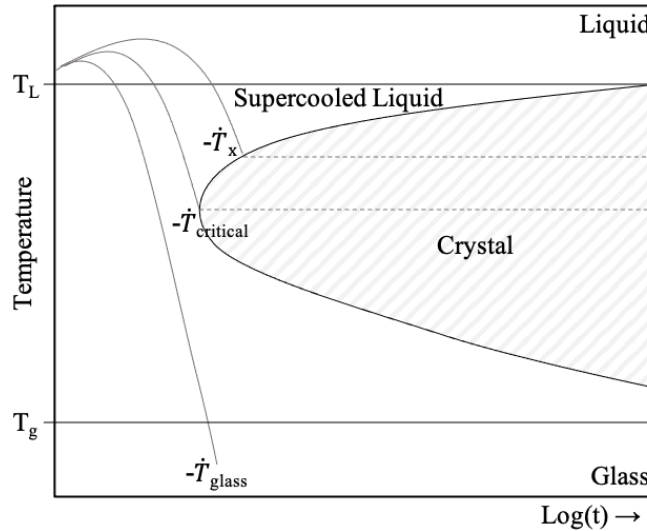
Figure 1.8: Representative Temperature-Time-Transformation (TTT) diagram where $-\dot{T}_{glass}$, $-\dot{T}_c$, and $-\dot{T}_x$ are cooling rates achieving a glass, the critical cooling rate, and a representative cooling rate where sample crystallizes, respectively.

crystallization nose is interrupted by nucleation given too long of a cooling time, and crystallization occurs within the sample (Figure 1.8; $-\dot{T}_x$). The cooling rate separating these two behaviors is defined as the critical cooling rate $-\dot{T}_{crit}$. In order to successfully vitrify the quenched melt, the crystallization kinetics of the sample need to be sufficiently sluggish or the casting method be sufficiently fast (i.e., quench rate faster than $-\dot{T}_{crit}$). Additionally, dependent on the regime of fragility, strong vs. fragile, the casting method and or sample dimensions must be selected accordingly.

Pre-Quench Controls

Additional factors that influence successful glass formation are overheating and fluxing. Overheated samples, samples taken at least 100°C over the liquidus temperature before quench, are found to exhibit better glass forming ability than those taken only slightly over their melting point.[5] This is presumably a result of melting any foreign particles such as oxides, etc.[8] Also, fluxing with boron oxide for long times increases glass-forming ability.[25] Both details are currently correlated with reduction of oxide-induced crystal nucleation sites. The former is believed to melt the oxides before quenching, and the latter to remove the oxides during alloying.[46]

While the underlying physics behind the benefit of overheating is not fully understood, Chapter 4 on a Ni-glass will address the effect of overheating on BMG embrittlement and its origin.

Method	Cooling Rate (K/s)	Sample Geometry	Sample Dimension
Splat Quenching	$10^5 - 10^6$	Circular foil	2-cm x 10-μm
Quartz Tube/Water	14	Rod or capillary	mm to needle
Injection Molding	10^2	Die cut	mm
Counter Gravity	$10^1 - 10^2$	Die cut	cm
Arc Melt/Suction	$10^1 - 10^2$	Rounded	cm
Air Quench	1 - 10	Any	Any

Table 1.1: Summary of method cooling rates and respective practical geometries and dimensions.[47, 48, 49, 50]

Methods Addressing Kinetic Quench Requirements

When selecting a quenching method, multiple parameters must be discussed; the cooling rate must be sufficiently fast ($> -\dot{T}_c$), and the required sample geometry and dimensions must be specified.

Cooling rates range from $10^5 - 10^6$ K/s for splat quenching, down to $1 - 10$ for air quenching. Table 1.1 column 2 summarizes common casting methods and their achievable cooling rates. For geometry, while fastest, splat quenching only yields 2-cm x ~10-μm thick foils; only practical for select uses. Common practical geometries include rods and capillaries through water-quenching in quartz tubes, and injection casting achieves cylinders, plates, bars, wedges, etc. via die-cut copper molds. Table 1.1 column 3 summarizes the geometries capable per casting method.

To achieve greater sample dimensions, stronger glasses with high Turnbull parameter (t_{rg}) and associated slower critical cooling rates make more methods accessible. However, when sample kinetics are sufficiently fragile, atomic diffusion must be suppressed at deep undercooling. The required faster critical cooling rate can be accommodated by employing smaller sample dimensions. Essentially, the rate of heat removable typically scales with the inverse square of sample thickness/diameter according to the solutions of the transient Fourier heat flow equation. Quartz-drawn capillaries are frequently used to achieve the smallest possible sample rod diameter for quenching ultra-fragile glasses. Table 1.1 column 4 summarizes the dimensions possible per casting method.

All these details work in concert to predict and achieve successful vitrification of a quenched melt. It is also noteworthy that more intricate net shaped samples are possible by use of post-casting methods that exploit the glass transition and BMG formability. These include thermoplastic forming (TPF) and additive manufacturing (3D printing) to build up more complex shapes.[51, 52] Thermoplastic forming takes

a pre-cast BMG rod, heated above T_g, and a force applied to induce flow into a mold. This method was used, for instance, to cast nanopatterned BMGs for a subcutaneous blood glucose biosensor.[21] A single BMG rod formed both the substrate and nonopillars ~200-nm in diameter.[21] 3D printing of BMG material deposits the molten alloy in sequential layers to form a 3D structure, where the cooling rate of individual layers is determined by the layer thickness. In both cases, the sample cools before crystallization intervenes and remains amorphous.

Description for Glass Quality — Glass Forming Ability

The natural interplay between heat removal rate and sample dimension gives rise to the synonymous metrics of critical casting thickness, critical rod diameter, and glass-forming ability (GFA). GFA is reported in terms of the maximum achievable fully amorphous rod diameter (or plate thickness). This is determined in practice by identifying amorphous characteristics (by XRD, DSC, electron microscopy, etc.) at increasing rod diameters until a detectable level of crystallinity is present (i.e., XRD peaks appear or a calorimetric T_g or T_x disappear).

Formation Summary — Taking Metallic Glass to the Bulk Form

Due to the collaborative nature of these factors, some alloy systems and compositions form glasses more readily than others. Tuning the aforementioned formation controls led early research to increase glass quality, qualified by max achievable sample thickness. These methods resulted in the growth from the first AuSi 10-μm foil to Bulk Metallic Glass, millimeters in dimension.

1.4   Transition Types and Melting Criteria

While initial descriptions of BMG transitions (T_g, T_x, T_m, T_l, T_s) in Section 1.1 are useful, further discussion is necessary to better support Chapters 2 and 3.

Transition Types — Thermodynamic Classifications

In 1933, Paul Ehrenfest proposed a classification system for phase transitions. Based on the thermodynamic free energy and other state variables, transitions are labeled by the lowest derivative for which the free energy exhibits a discontinuity at the transition (phase boundary); where the Gibb's free energy is a function of independent thermodynamic variables (T, P, H, c, etc.).[53] A transition that shows a discontinuity in the first derivative of the free energy is labeled a first-order phase transition, and similarly for a discontinuity in the second derivative; a second- or-

der phase transition.[54] In Ehrenfest's classifications, there could theoretically be third, fourth, and higher-order phase transitions, but only first- and second-order transitions are discussed here.

These discontinuities in free energy derivatives have physical meaning. Typical first-order transitions between solid, liquid, and gas have a discontinuity in the first derivative of free energy with respect to pressure. This translates to a discontinuous change in molar volume or density at the transition.[54] An example of a second-order transition is the ferromagnetic phase transition in iron and other metals where the derivatives are taken with respect to applied magnetic field strength, H. This transition shows a continuous change in magnetization across the phase boundary (first derivative), but reveals a discontinuity in magnetic susceptibility (second derivative).[45]

While useful, not all transitions fit into Ehrenfest's classification. For example, the superfluid transition in liquid He and other transitions are characterized by power law or logarithmic singularities in the second derivatives of the free energy (e.g., heat capacity, sususceptibility, etc.) at the critical temperature, as opposed to simple discontinuities.[45] These are often referred to as Lamda-transitions. Such transitions are unclassifiable by Erhenfest's classification scheme. Thus, these classifications were replaced by a similar but simplified naming convention that does account for these transitions.

Modern classifications use the same names as Erhenfest's historical convention, but with updated definitions. First-order transitions are now described as having a latent heat — energy per volume is either absorbed or released at a fixed temperature. Transitions between solid, liquid, and gas phases remain first-order in this classification. Second-order transitions are also called continuous or order-disorder transitions, and exhibit a decay in a correlation length across the critical point.[45] Examples include ferromagnetic, superconducting, and superfluid transitions.

But when compared mathematically, both naming schemes describe various phenomena in similar ways:

For first-order transitions, when $G(T, P)$ is continuous and $S = -(\delta G/\delta T)_P$ or $V = -(\delta G/\delta P)_T$ are discontinuous, there is a latent heat and/or density change, respectively. For a second-order transition, when $G(T, P)$ is continuous as well as $S(T, P)$ and $V(T, P)$, discontinuities in the second derivatives of $G(T, P, N)$ describe discontinuities in the response functions for heat capacity, isothermal compressibil-

ity κ, and the thermal expansion coefficient, α:[45]

$$C_P = T\left(\frac{\delta S}{\delta T}\right)_P \qquad\qquad = -T\left(\frac{\delta^2 G}{\delta^2 T}\right)_P$$

$$\kappa_T = -\frac{1}{V}\left(\frac{\delta V}{\delta P}\right)_T \qquad\qquad = -\frac{1}{V}\left(\frac{\delta^2 G}{\delta^2 T}\right)_T$$

$$\alpha = \frac{1}{V}\left(\frac{\delta V}{\delta T}\right) \qquad\qquad = -\frac{1}{V}\left(\frac{\delta^2 G}{\delta T \delta P}\right)$$

The liquid/glass transition as observed experimentally displays a continuous change in viscosity at T_g, an apparent jump in the volume thermal expansion coefficient and heat capacity.[55] These sudden observed changes at T_g are what make detection of the glass transition possible in a DSC or Thermomechanical analyzer (TMA). However, these changes are also observed to depend on heat/cooling rates. There has been an ongoing debate in the literature over whether the glass transition is a purely kinetic transition or whether there exists an underlying thermodynamic phase transition. Further, it is also known that the presence of disorder can broaden a first- or second-order phase transition. As a result, there has been further debate as to whether the glass transition might be viewed as a broadened first-order transition or how it might be described. The question of whether the glass transition is characterized by an underlying thermodynamic transition is explored in Chapter 2. Further context on identifying this transition as a type of melting transition is discussed there.

Additional Melting Criteria

In addition to the thermodynamic description of melting (a latent heat), two more criteria have been developed and described in the literature. The Lindemann and Born melting criteria focus on different aspects of melting — Lindemann on vibrational instability and Born on elastic rigidity loss. The Lindemann melting criterion indicates that melting occurs via a vibrational instability — such that a material will melt when the average amplitude of thermal vibrations exceeds some critical fraction of the interatomic distances.[56] Essentially the vibrations will cause motion greater than intermolecular interactions will support. The Born melting criterion focuses on the loss of elastic rigidity upon melting as quantified by the loss of a

finite shear modulus. Upon heating, a solid can no longer support shear stress; it has lost rigidity. In this approach, melting is viewed as a "rigidity catastrophe."[57]

Liquid/Liquid Transitions in Experiment and Computer Simulation

While common phase transitions occur between the three states of matter — solid, liquid, and gas — there also exist transitions within these states of matter, i.e., Intra-phase transitions. Such transitions may involve both ordered and disordered materials and occur when a solid-solid or liquid-liquid transition phase boundary is crossed within a phase diagram. An ordered solid can have various crystal or amorphous structures (polymorphism), an amorphous material can have multiple disordered structures (polyamorphism), and a liquid may exist in two distinct phases (liquid polyamorphism). Such transitions are identified by changes in thermodynamic or structural characteristics as one crosses the phase boundary. Primary polymorphism identifying tools include DSC and X-ray diffractometry, while Raman spectroscopy, thermomicroscopy, and other methods are used depending on the material.[58]

These transitions occur in solids and liquids. Notable examples are as follows. For solid-solid transitions, ice has 19 polymorphs, with three different amorphous structures.[59] The structures, identified via calorimetry and neutron powder diffraction, were formed using varying pressure and other techniques, and the phases have distinct structures and densities.[59] Liquid-liquid transitions are also observed, but lack distinct structural differences as found in solids. These transitions occur between states of disorder within the liquid phase and are often observed using thermal DSC scans. Recent research has established a liquid-liquid polymorphism as a key component in the pharmaceutical industry. Mannitol, a diuretic to reduce pressure inside the eye or around the brain, is the first pharmaceutical that utilizes a lower-energy polymorph for increased aqueous solubility for drug delivery.[60]

While the phrase "liquid-liquid" transition is generally limited to the liquid phase, polyamorphs may exist for any non-crystalline material; i.e., glasses, other amorphous solids, super-cooled liquids, as well as typical conventional liquids or fluids. So within the liquid-like amorphous-structured solid phase, glass-glass transitions are possible. While glass-glass transitions are often difficult to identify, discontinuous property changes are a strong indicator of a phase transition. For example, work by Ketkaew and Schroers *et al.* observed an abrupt mechanical glass-glass toughening transition. They saw notch fracture toughness displaying an abrupt change as

a function of a well-controlled fictive temperature (describing average glass structure).[61] Through this, they identified how to achieve the two glass states with different properties. The distinct ductility and hardness across the phase boundary were tied to control of the fictive temperature by annealing. This transition potentially underlies the relatively abrupt embrittlement observed during processing of BMGs.[61] Once discontinuous properties are identified, annealing, deformation, or other processing may be used to reproducibly create the two different phases. This method of discontinuous properties correlated with phase transition will be used in Chapter 4 to explore the underlying case of the embrittlement transition in Ni-based BMGs.

While discontinuous properties provide evidence of an intra-glass transition, the thermodynamics are particularly difficult to identify due to the metastability of the supercooled region. While experiments allow up to 20% undercooling of a BMG, the metastable samples crystallize rapidly the deeper the undercooling.[62] Thus, direct observation of evidence for a thermodynamic transition requires high-speed techniques such as Flash DSC (FDSC) or, alternatively, computational methods wherein much shorter time scales can be probed.

Experimental work has used FDSC to probe glass-glass transitions in the SCL. Schawe and Loeffler *et al.* identified two monolithic polyamorphs in Au-based quintary and quaternary BMGs.[63, 64] They used FDSC to access the heating rates necessary to melt the intermediate metastable phases within the SCL. They termed the two glass states a self-doped glass (SDG) and a chemical homogeneous glass (CHG), each with their own crystallization nose in a TTT diagram.[63] Shen *et al.* describes a secondary Metallic Glacial Glass (MGG) arising from a first-order transition in the SCL.[65] They probed a quaternary La-glass and report the MGG forming below the crystallization nose through FDSC.[65] It is important to note that generally, as the number of elements in a BMG decreases, the fragility increases. The FDSC works explored five- and four-element BMGs and found secondary glasses by utilizing high heating rates. However, it is hypothesized that within the elusive high-fragility regime, there may exist polyamorphs as secondary glass phases. To achieve successful analysis of high and ultra-high fragility samples, the sample kinetics require even faster methods than FDSC. In a collaboration with the author, An *et al.* used molecular dynamics to probe this metastable deep-undercooling regime for secondary glass phases in binary and single-element BMGs.

An *et al.* investigated pure Ag, and binary AgCu, and CuZr using Molecular
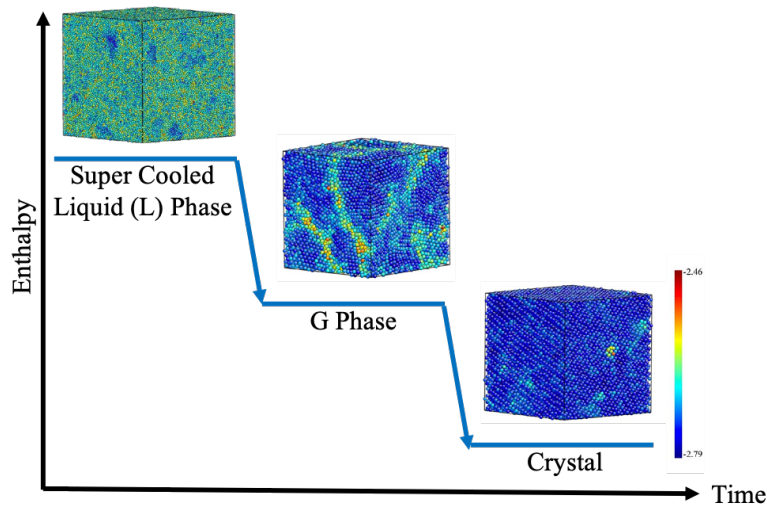
Figure 1.9: Energetic coordinate diagram for the traditional BMG phase (L glass), the secondary glass (G) phase, and the crystal of pure Ag. Figure recreated from [62].

Dynamics Simulations. They were the first to report and identify the heterogeneous G-phase, and define its first-order liquid-liquid transition to the traditional liquid-like L-phase metallic glass. This secondary glass phase, termed the G-phase, is a heterogeneous energetic metastable intermediate phase that lies thermodynamically between the traditional homogeneous SCL (L) glass and the equilibrium crystalline phase (Figure 1.9). It forms via a first-order freezing transition from the L-phase liquid with a latent heat and discontinuous entropy change. The transition was shown to be reversible, with the G-phase "melting" along a coexistence curve to the L-phase liquid. The heterogenous G-phase structure is composed of ordered core regions surrounded by disordered liquid-like regions with consistently higher configurational enthalpy (Figure 1.9). The core regions exhibit local short-range order on a scale of ~1-nm resembling nanocrystals, but with distinct curvature in the atomic planes along with stacking faults and point defects. The apparent size of the ordered cores varied with temperature and composition (in the case of alloys). The L-G transition is suppressed by the binary alloy systems with a reduced-ordered core size and heterogeneity length scale, along with a smaller latent heat for the L-G transition. The heterogeneity length scales were 4, 2, 1.8, and 1.5-nm for pure Ag, AgCu, Cu_7Zr_3, and Cu_2Zr, respectively. Core regions exhibit fcc/hcp and icosahedral short-range order for Ag and AgCu (fcc/hcp) versus CuZr (icosahedral) cases, respectively. The G-phase is predominantly disordered, where ordered cores

contribute only 25% to overall local structure. The more-ordered solid-like G-glass exhibits persistent long-range elastic rigidity with a finite shear modulus as compared with the more fluid-like L-phase. Compositionally, the G-phase shows the structural heterogeneity as independent of chemistry or chemical separation in pure Ag.[62] In the binary alloys, AgCu revealed similar average composition across the heterogeneous G-phase structure, but wider variance from the L-phase.[66] The CuZr alloys identified that chemistry is not correlated with the L-G transition, though there is some spatial heterogeneity over the whole sample.[67]

These secondary glass works provide an important broader context for the findings throughout this thesis. The details of the L-G transition as revealed in the simulation work are related to the experimental results of Chapters 2 - 4, and will be expanded on further there. The results of this thesis are compared back to the G-phase and MGG to represent the simulation and experimental works, respectively. These are described together, as it is hypothesized that the SDG of Schawe and Loeffler's work and the metallic glacial glass (MGG phase) of Shen's work are essentially equivalent to the An *et al.*'s G-phase. Throughout the thesis, the primary and secondary glasses will be referenced by the terms L-, traditional-, and liquid-like glass/phase, and G-, ordered-, or solid-like glass/phase, respectively.

1.5 Motivation

This introduction has provided a summary of the important theoretical concepts and experimental background related to the nature of the glass transition in general and metallic glasses in particular. In addition, each section outlined particular shortcomings, inaccuracies, or a lack of sufficient understanding. These now become the motivations for this thesis:

1. Insufficient data both at high fragility and in the SCL yield a limited understanding of metallic glasses;

2. Current thermodynamic methods collect data from a non-equilibrium state, yielding erroneous data;

3. Inaccuracies of the Gaussian Landscape model in PEL theory require a new DOS representation to accurately describe data;

4. Incomplete understanding of BMG embrittlement;

5. Uncertainty of how the secondary G-phase glass manifests across experimental glass fragility.

Chapter 2 addresses motivations 1 - 3 with analysis of ultra-high fragility $Pt_{80-X}Cu_XP_{20}$ in a well-established ground state. The work presents a systematic experimental investigation of the configurational thermodynamics of the undercooled liquid as one approaches the glass transition. By accurate direct measurements of the liquid configurational enthalpy as a function of temperature, we are able to accurately determine the thermodynamic state functions of the undercooled liquid as the glass transition is approached. We find that the traditional Gaussian PEL model fails to describe the configurational thermodynamics of these ultra-fragile liquids. With increasing fragility, the glass transition becomes progressively sharper and remarkably evolves into an apparent discontinuous first-order phase transition with a latent heat and discontinuous change in configurational entropy. In this high-fragility limit, the glassy phase appears to display first-order "melting" in much the same manner as crystals melt.

Chapter 3 addresses motivation 5 by investigating the mechanics, structure, and thermodynamics on either side of the anneal-induced transition proposed in $Pt_{80-X}Cu_XP_{20}$ (Chapter 2). Hardness data reveal the G-phase grows on quenching in ultra-fragile glasses, but on annealing in high-fragility glasses. X-ray diffraction report amorphous behavior across both phases (as-cast and anneal samples) in all compositions. Thermodynamically, the onset of the glass-melting transition is observed in 20 K/min room temperature to melt DSC scans in the most ultra-fragile sample, X = 14. This is further supported by high-speed infrared imaging of rapid capacitive heating, where a melting (cooling) front is observed before interruption by recalescence. These show Chapter 2's configurational enthalpy glass-melting transition in traditional thermodynamic scans, further supporting this glass-melting transition.

Chapter 4 addresses motivations 4 and 5 with a kinetically stronger glass system, $Ni_{71.4}Cr_{5.64}Nb_{3.46}P_{16.5}B_3$ (Ni208) with $m \sim 54$, and its observed embrittlement transition. This work identifies previously unreported round inclusions that share properties with the secondary glass in works by An *et al.* and Shen *et al.*; inclusions maintain the same composition but are 25 - 28% harder than matrix, and high-resolution TEM identifies a heterogeneous structure in the inclusions with SAED. The inclusions are correlated with the embrittlement transition and suppression via overheating, for they are only present in embrittled samples across multiple heat

treatment types. In effect, this chapter explores how the second glass phase in high-fragility PtCuP may extend to a stronger glass system.

Chapter 2

THE EMERGENT FIRST-ORDER PHASE TRANSITION IN ULTRA-FRAGILE $Pt_{80-X}Cu_XP_{20}$ BULK METALLIC GLASS

2.1 Abstract

The following chapter reports the experimental configurational thermodynamics of a highly-fragile near-eutectic $Pt_{80-X}Cu_XP_{20}$ BMG system. When X is decreased from 27 to 14, samples maintain bulk glass-forming ability, display increasing fragility to the ultra-fragile regime (X < 17), and show an increasingly sharp glass transition. A generalized equation is proposed and utilized for configurational thermodynamic data fitting and analysis. At X < 17, evidence of a first-order melting transition is observed. The specific configurational enthalpy versus temperature curve displays a sudden discontinuous increase or latent heat at a well-defined glass-melting temperature, T_{gm} across the $Pt_{80-X}Cu_XP_{20}$ composition landscape. When analyzing configurational entropy, at low X, the Kauzmann temperature merges with the glass transition temperature. Below T_{gm}, ultra-fragile samples comply with the third law of thermodynamics; i.e., entropy falls and approaches that of the crystalline eutectic solid at the low-temperature limit, thereby averting the Kauzmann paradox. Configurational enthalpies of the equilibrated liquid are measured directly and relative to well-defined crystalline reference state. The $Pt_{80-X}Cu_XP_{20}$ alloy system displays a first-order melting transition from a low-temperature solid-like glass to a liquid-like phase as one progresses from a strong to a fragile metallic glass system.

2.2 Introduction

As described in the overall introduction to this thesis, there are a number of short-comings in existing metallic glass thermodynamic theory. This chapter aims to address these shortcomings by focusing on the high- and ultra-high-fragility regime, providing an accurate thermodynamic description with a well-established reference state, proposing and utilizing a new, non-Gaussian approach to thermodynamic data fitting, and utilizing methods that provide more accurate data in the ΔT data gap of the liquid. Together, this work aims to discover what lies beneath when accurate thermodynamics are utilized.

First, a high kinetically fragile metallic glass system that retains bulk glass-forming

$Pt_{80-X}Cu_XP_{20}$ (at. %)	Fragility, m	T_g (K)	T_S (K)	T_L (K)	h_m (J/g)	GFA (mm)
$Pt_{66}Cu_{14}P_{20}$	>90	504	828.9 (1.0)	879.4 (1.0)	67.7	1.5-2
$Pt_{64}Cu_{16}P_{20}$	>90	504	827.8 (1.0)	877.5 (1.0)	68.7	3
$Pt_{62}Cu_{18}P_{20}$	>90	505	816.9 (0.5)	864.1 (0.5)	71.8	4
$Pt_{60}Cu_{20}P_{20}$	85	505	825.6 (1.0)	833.7 (1.0)	67.8	6-7
$Pt_{57}Cu_{23}P_{20}$	73	505	823.8 (0.2)	827.9 (0.2)	68.5	15
$Pt_{53}Cu_{27}P_{20}$	60	506	819.5 (0.1)	840.1 (0.1)	67.5	27

Table 2.1: $Pt_{80-X}Cu_XP_{20}$ glass system property variances with composition.[68] Heating rates utilized are noted in parenthesis in K/min.
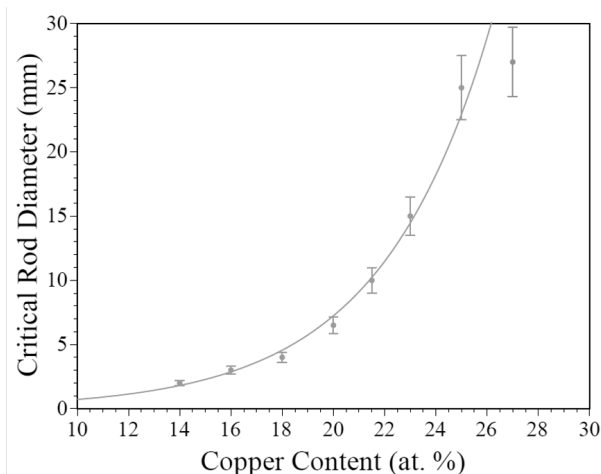
Figure 2.1: Visualization of critical rod diameter variance with copper content, X. Reproduced from Na *et al.*[68]

ability at high fragility is required. This maintained bulk glass formability will allow the application of traditional equilibrium thermodynamics and testing while supporting the high-fragility regime.

$Pt_{80-X}Cu_XP_{20}$; A Tune-able High-Fragility Bulk Glass

Due to the difficulty in casting bulk high-fragility glasses, their properties have remained predominantly unmeasured. However, in 2015, Na *et al.* at Glassimetal Technologies discovered a bulk glass-forming high-fragility BMG system. This $Pt_{80-X}Cu_XP_{20}$ system displays widely varying and tunable fragility with alloy composition while maintaining bulk glass-forming ability. The already high-fragility eutectic composition ($m = 73$ for X = 23) increases in fragility as the Cu content

of the alloy decreases.[10] The *m* reported for ultra-fragile compositions is in fact a lower bound, as the viscosity becomes highly non-Newtonian and crystallization becomes strain-rate sensitive. This makes the measurement of viscosity inaccessible at the lower Cu content when using traditional rheometric methods (TMA etc.). Table 2.1 denotes how composition adjustment dramatically alters Angell fragility, heat of fusion, and GFA with little to no change in the glass transition temperature, T_g, or melting temperatures. When X < 17, fragility apparently extends into the ultra-fragile m > 90 regime, and remarkably, GFA remains at the bulk scale (rods of several mm diameter) as visualized in Figure 2.1. This allows for use of traditional bulk calorimetric methods and traditional testing (ultrasonic testing, viscosity measurement, etc.).

Experimental Configurational Thermodynamics

The thermodynamic models and treatments described in Section 1.2 will be applied here. Combined with further underlying assumptions described in Appendix B.1, this chapter uses PEL separability to focus on configurational thermodynamics of a fragile metallic glass system.

When studying configurational components of thermodynamic functions, well-equilibrated crystal and glass states are imperative. In the PtCuP system, glass reference states are achieved through extended annealing at times several orders of magnitude greater than the α (Maxwell) configurational relaxation time; annealing of 15 hours for X = 18 - 27, and 3 hours for X < 17 due to their ultra-high fragility. These give the PtCuP alloys sufficient time to configurationally relax, thereby establishing an equilibrium distribution of inherent state configurations. This in turn justifies the application of thermodynamic relations between state variables (specific heat, entropy, enathalpy, etc.)

Establishing a well-defined crystalline reference state at fixed T is essential, for configurational enthalpies are measured as heats of crystallization and heats of fusion relative to this crystalline reference state. This method used here describes the evolution of structure energies at varying temperatures. In the PtCuP system, the crystalline eutectic solid contains three crystalline phases (Pt_7Cu, Pt_5P_2, Cu_3P), each with distinct compositions from the liquid. This multi-phase eutectic solid acts as the well-defined thermodynamic configurational ground state in the present work.

This present work assures high-quality thermodynamic data by modifying a tradi-

tional approach. In place of commonly reported heat capacity measurements and subsequent integration to obtain enthalpy, $h(T)$, liquid enthalpy is directly measured using the crystalline reference-state approach. In traditional glass calorimetry, heat capacity is assumed to be an equilibrium property of the liquid in the absence of crystallization, but BMG heat capacities are typically measured relative to the crystal. Utilizing the present approach, liquid configurational enthalpy is reported as the heat of crystallization of the supercooled liquid state at a given temperature. This assumes that the vibrational contributions to the enthalpy of the liquid and crystal are approximately equal, and thus cancel in the vicinity of the glass transition temperature as has been experimentally demonstrated by Smith *et al.* and discussed in Chapter 1.

Appendix B.1 describes the underlying assumptions and approximations used in this work. In effect, the reported enthalpy is a direct measure of the difference in potential energy across the liquid-crystal transformation at a given T. This difference is then assumed to be purely configurational, so $h_{LX}(T) = h_C(T)$. Thus through direct measure of h_{LX}, h_c is determined. The reader is directed to Appendix B.1 for a detailed summary of how these assumptions are used to arrive at these simplifying conclusions.

Thermodynamic Theory and Analysis

Given the shortcomings of the Gaussian PEL DOS, this present work uses a more generalized approach. Equation 2.1 is introduced to describe the configurational enthalpy of the liquid. Introducing an alloy-dependent "isenthalpic" temperature, θ_h, a high-temperature enthalpy limit, $h_{LX}(\infty) = h_C(\infty)$, and an exponent n as a generalized thermodynamic fragility index:

$$h_c(T) = h_c(\infty)\left[1 - \left(\frac{\theta_h}{T}\right)^n\right]. \tag{2.1}$$

$$s_c(\phi) \propto s_c(\phi_0) - C(\phi_0 - \phi)^{\left(\frac{n+1}{n}\right)}, \tag{2.2}$$

here C is a normalization constant and ϕ_0 is the limiting value of potential energy in the high temperature limit, $T \to \infty$. Also, in this case, $n = 1$ describes the Gaussian distribution. The subsequent analysis will describe how this equation provides a new view of the Kauzmann paradox at high n (or equivalently, high m).
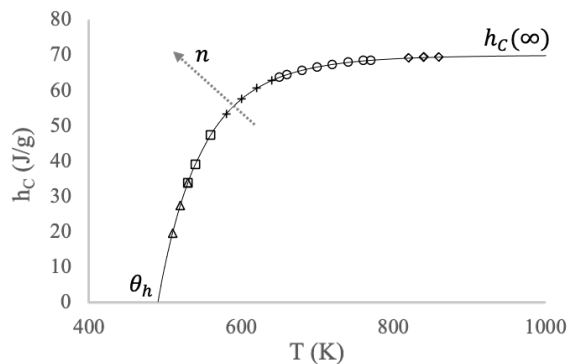
Figure 2.2: Representative h_C plot identifying $h_C(\infty)$ and θ_h terms, and depicting n-dependent curvature. Methods and respective temperature ranges are indicated by the data symbols; i.e., isothermal holds (triangle), constant heating rate (square), rapid discharge heating (plus sign), successive cyclic undercoolings (circle), melting of crystallized samples (diamond).

In effect, the experimental results of this chapter on a high-fragility BMG system demonstrate that the glass transition becomes increasingly sharper and apparently evolves toward a first-order "melting transition" in the limit of an ultra-fragile liquid. In this limit, a glass melts in much the same manner as crystals melt — with an accompanying latent heat, entropy of fusion, etc.

2.3 Methods

The overall approach records the configurational enthalpy via the heat of crystallization at various temperatures in the glass system. In order to measure the configurational enthalpy about the glass transition, methods with various thermal histories are required. Isotherms and low heating rate scans were used to measure the low-temperature heat of crystallization in the low ΔT region, and fast scans via rapid capacitive discharge heating yield mid-ΔT crystallization data. Undercoolings report high-temperature heat of crystallization, and h_C is reported at decreasing temperatures with successive undercooling cycles. All samples are reheated to the equilibrium melt following crystallization and the enthalpy of fusion is reported. These data regions are depicted in Figure 2.2 and a detailed description of each method is outlined below. Together, these methods yield the configurational enthalpy curve of the liquid relative to the enthalpy of the crystallized eutectic sample.

Sample Preparation

Samples were cast by water quenching the molten alloys in quartz tubes. The alloys are initially melted and equilibrated in a furnace at 900°C, well above the melting temperature. The sample is then quickly transferred from the furnace and quenched into a water bath. For compositions X = 18 - 23, rod samples were cast in 3-mm fixed-diameter quartz tubes. For X = 14 and 16, samples were quenched in long, tapered, drawn quartz capillaries up to 1-mm in diameter. Fluxing was not required to obtain fully amorphous samples in the PtCuP system. For all DTA runs, the end of a sample rod was made flat for good thermal contact. Each sample was cut to 30 - 60 mg for optimal signal-to-noise ratio. Samples were cleaned with 3 rinses and 1 ten-minute sonicated bath each of acetone and ethanol. Once dried, the samples were weighed and placed flat-side down in a lidded alumina pan in the DTA.

Differential Scanning Calorimetry; $h_C T$ Measurement Methods

The calorimetry work reported here was done using a calibrated Netzsch 404C F3 DTA with separate calibrations for each constant heating rate reported. A sapphire standard was used for calibration. All samples were annealed at T_g as the first step to establish a well-defined thermal history and initial sample equilibrium state. Anneal duration was dependent on fragility; 18 < X < 27 for 15 hours, and 3 hours for X < 17. The error in the measured enthalpy changes for the runs was established through the measured variation of the enthalpy of fusion. Each DTA run melted the sample, and the standard deviation across these runs was determined as the instrumental error at ± 1.5 J/g.

Isothermal Holds

After annealing at T_g, samples were heated at 2 K/min to a range of temperatures above T_g in the ΔT region and held isothermally at a fixed T until crystallization occurred. Post crystallization, the samples were subsequently heated at 10 K/m through the melting transition. Isothermal hold temperatures ranged 232 to 252°C or 505 to 525K. Specific enthalpies of crystallization and fusion were recorded and added to the $h_C(T)$ plots. Isothermal runs minimize thermal lag effects in the calorimeter, allowing the instrument to reach stable steady-state conditions with a well-defined signal baseline. In turn, this permits a very consistent and most accurate determination of the heat of crystallization. However, due to the slow heating rate to approach the isothermal hold temperatures and the finite time required to achieve

steady-state, accurate heat of crystallization data above 252°C or 525K could not be obtained since crystallization intervenes before steady-state is achieved in the DTA. Thus, to measure the heat of crystallization further into the ΔT region, one must switch from the isothermal protocol to a constant heating rate protocol following initial annealing at T_g.

Constant Heating Rate

After the annealing step, samples are heated at a constant heating rate through crystallization and melting using a large range of rates, including 0.1, 0.5, 1.5, 3, 5, 8, 10, 15, and 20 K/min. This broad range assured the transition from isothermal crystallization conditions to constant heating conditions was well explored, and the heat of crystallization (or equivalently the configurational enthalpies) across a range of temperatures was recorded. The shift in crystallization onset with temperature is in part due to the instrumental lag (transient instrumental response) at higher heating rates. Heating rates at and below 5 K/min are preferred for better sample equilibration and reduced thermal lag within each run. The lower the heating rate, the sharper the DTA time and temperature resolution achieved for the heat of crystallization. Calibration runs of the melting transition of Sn at various heating rates were used to correct for instrumental thermal lag effects. Tin's melting point at 231.9°C is optimally located very near the PtCuP T_g of ~ 230°C, thereby providing an optimal correction for transient instrumental effects. The correction runs are included in Appendix B.3. In general, 20 K/min heating rates are commonly used in DSC and DTA studies reported in literature, but thermal lag effects are seldom accounted for. By directly accounting for transient instrumental broadening and temperature shift of the exothermic crystallization DTA signal, we are able to improve the temperature resolution in our $h_{LX}(T)$ measurements. Basically, we more precisely determine the sample temperature during the liquid-crystal transformation.

Cyclic Undercooling

As- cast samples are cycled repeatedly (heating and cooling) from below T_g through crystallization and melting (T_m + 150K) at 5 K/min in the DTA. The number of cycle steps is limited only by the number of programmable steps in the DTA. This method allows for the collection of crystallization data over a wide range of temperatures in the undercooled region. Successive undercoolings yield the crystallization event at progressively lower and lower temperatures, thereby enabling collection of heat of

crystallization data in the upper range of the ΔT region of the h_C curve.

Melting

Heating through melting of the crystallized sample was carried out after each crystallization run to assure a complete liquid-crystal transformation had occurred. Any additional heat release events were investigated for structural differences via XRD. The heat of fusion was determined for each sample following each crystallization transformation.

Rapid Capacitive Discharge Heating

Rapid capacitive discharge heating (RDH) was used to measure data in the mid-ΔT region. The system uses ohmic dissipation with 15-kJ capacitive discharge heating on rod samples 3-cm in length and ranging from 3 to 5-mm in diameter. Samples were uniformly heated at heating rates up to $\sim 10^5$ K/s by fully discharging a capacitor bank from various charging voltages to vary the energy deposited in the sample rod. The sample is clamped between two copper electrodes. Temperature was measured with the Impac series 5 non-contact high-speed pyrometer with a 5 μs time resolution. A FLIR SC-4000 infrared camera was combined with the RDH system for infrared images of coupled eutectic growth (see Figure 2.5). The infrared camera functions with 256,000 pixels and frame rates up 1,300 frames/s.

Data Analysis; h(T)

For each of the methods listed above, the heat flow signal is recorded as a function of temperature and or time (for isothermal segments). Configurational enthalpy is calculated as the area beneath the exothermic crystallization curve and the enthalpy of melting is calculated as area under the endothermic melting transition.

Additional Methods

Additional methods that provided supporting information for the thermal analysis are included here. Viscosity was measured via Beam Bending in a Perkin-Elmer Thermo Mechanical Analyzer. X-ray diffraction scans were completed with a Bruker D2 Phaser diffractometer. The shear modulus was measured using ultrasonic transducers in the pulse-echo configuration. 25-MHz quartz transducers were used to determine the shear sound velocities on 3-mm diameter rods. Density was measured via wet/dry mass measurement in the Archimedes method.

2.4 Results and Discussion

While many properties of the PtCuP alloy family are detailed in Table 2.1, the supercooled liquid must first be verified to be in metastable configurational equilibrium in order to apply equilibrium thermodynamic relationships in the analysis of data. Configurational relaxation takes place with a characteristic time scale given by the Maxwell relaxation time of the liquid. In turn, this can be determined from the viscosity of the liquid along with knowledge of the liquid high-frequency shear modulus. For X = 23, at T_g, time to crystallization onset is observed as $t_{LX} > 10^6$ s ($\sim$ 1 wk). This establishes the samples as metastable liquids, where the initial anneal times are sufficiently short to avoid nucleation and growth of crystalline phases. Before subjecting samples to thermal analysis, the achieved metastable equilibrium state must be verified further. Viscosity data are used to assess the extent of liquid configurational relaxation prior to crystallization. These data, in combination with the shear modulus, were used to estimate the Maxwell configurational relaxation time for the undercooled liquid, $\tau_\alpha = \tau_M = \eta(T)/G$, with G $\sim$ 32 GPa measured ultrasonically. Initial isothermal holds reported crystallization peak times, t_{peak}. The X = 23 data for t_{peak} and τ_α are illustrated in Figure 2.3a, where they are the top and bottom curves, respectively. When compared, the ratio of t_{peak} and τ_α quantifies the extent of liquid relaxation toward metastable configurational equilibrium prior to crystallization. With this ratio ranging from 10^3 to 10^6 for X = 23 and 20, it indicates that h_{LX} is representative of a configurationally relaxed undercooled liquid in metastable equilibrium prior to the onset of crystallization. It follows that the measured heat of crystallization is characteristic of the transformation of an equilibrium liquid to an equilibrium crystalline sample. This knowledge is applied to the remainder of the PtCuP glass system.

Along with an established metastable configurational equilibrium, the crystallization behavior of this system is important to defining a reference state for configurational thermodynamics. Initial observation of crystallization in the PtCuP system reports a sharp exothermic peak with rapid onset and decay. The peak shape is uniform across isothermal runs as plotted on a logarithmic time scale when normalized to peak height and peak time (Figure 2.3b). The crystallization event completes in a time, Δt_{LX}, much shorter than the preceding incubation period; $\Delta t_{LX} \ll t_{LX}$. The peak and transformation times follow simple scaling behavior, which implies a single crystallization event/mechanism. This is further verified by a pyrometer visualization of Rapid Capacitive Discharge where a single crystallization front is recorded. See the discussion accompanying Figure 2.5.
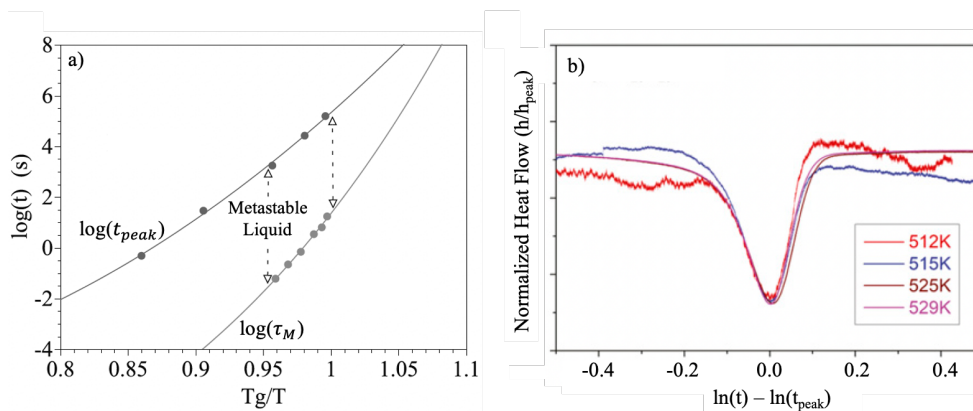
Figure 2.3: t_{peak} to $\tau_\alpha = \tau_M$ defined metastable liquid region (a), and normalized DTA scans displaying uniform peak shape (b). Reprinted with permission from [68].

Further evidence of a single sharp crystallization event comes from XRD analysis. As described in the Methods section, each run underwent multi-hour anneals, crystallization (isothermally or under constant heating rates), and then reheating and melting. XRD scans were carried out on the samples after each thermodynamic step and thermodynamic event. At slower heating rates, some samples expressed a second but smaller exothermic peak during reheating between the initial large crystallization event and melting. XRD results indicated a fully amorphous sample up to the initial crystallization event, and revealed no new crystalline diffraction peaks after the smaller second event (Figure 2.4). Thus the crystallization event at 240°C describes full crystallization. Further, with XRD showing no change in structure after the smaller second exothermic peak, it is believed that this excess heat release is due to coarsening of the microstructure produced by the primary/initial event.

Now that the equilibrium nature of the metastable liquid is validated and crystallization behavior understood, the enthalpy measurements from each method take focus. First, particular notes on data collection are described before greater trends are discussed across compositions and fragility. As discussed above, the isothermal holds have a clean sharp peak, but present a secondary peak between $320 - 340$°C. This second peak is also observed in slow constant heating rate scans. However, this second peak merged with the primary peak for heating rates above 1 K/min. When present, the excess heat release peak is assumed due to relaxation or coarsening as was done for the isotherms. And in both cases, the second Δh_C was added to the first to equal the reported h_C. The h_{LX} onset temperature data are adjusted according to the Sn melting corrections in Appendix B.3 and the raw data are included in
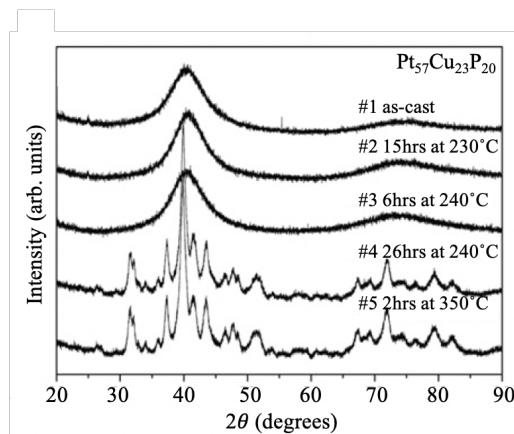
Figure 2.4: XRD post each thermodynamic step and transition for X = 23. Reprinted with permission from [68].

No other heat release events are detected in other scan segments. The isothermal scan and constant heating rate data compose the lower-temperature data within the ΔT region just above the glass transition.

A third set of DTA scans include cyclic undercooling data. Here, the as-cast samples underwent forty heating/cooling cycles from 200 to 900°C at 10 K/min. Undercooling increased with successive cool-reheat cycles. This deepening of undercooling is assumed due to the dissolution of heterogeneous crystal nucleants through cycled overheating of the melt. Maximum undercooling was achieved to 365°C, which is ~180°C below the eutectic temperature, T_E, taken as the average between the solidus and liquidus temperatures. The undercooling data fill in the h_C curve from just above the nucleation nose to ~50°C below T_E.

Melting data were collected for every scan during reheating, and describe the configurational enthalpy at the melting point, $h_C(T_E)$. These are the highest-temperature data on the h_C plots.

Measurements via rapid capacitive discharge contribute $h_{LX}(T)$ data to the mid-ΔT region. Figure 2.5a plots the T vs. t data. It visualizes the ultrafast heating to 350°C, configurational relaxation and stabilization at ~312°C, and rapid recalescence. Recalescence achieves 505°C which is below but near T_E. The ultrafast pyrometer data (Figure 2.5b) reveal a single crystallization event via coupled eutectic growth. The singular growth front proceeds at ~1.5-cm/s. This very high growth rate suggests short-range chemical order for the crystal phases may already present in the liquid, therefore mitigating the need for chemical partitioning along the advancing
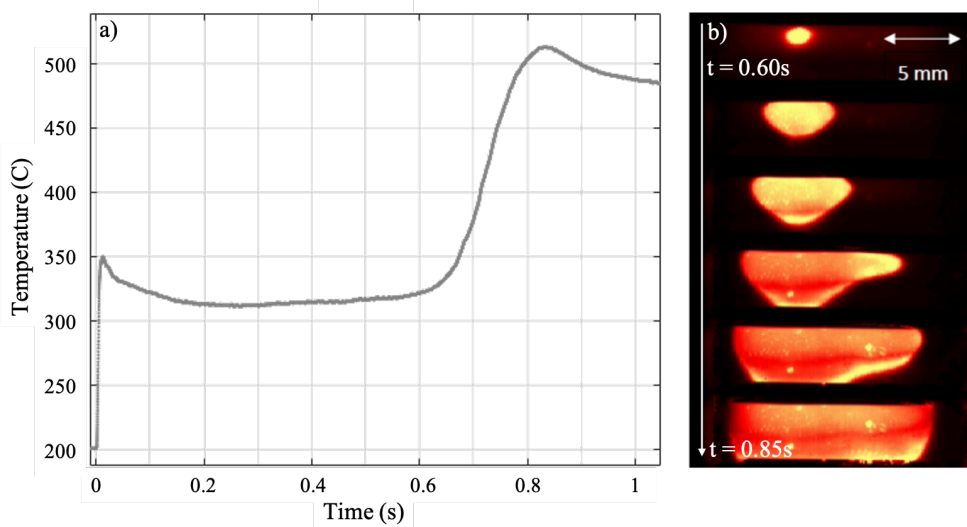
Figure 2.5: Rapid heating profile of the X = 20 sample. a) Temperature vs. Time profile shows rapid heating on recalescence. b) Ultrafast pyrometer from t = 0.6 -– 0.85s. Reproduced with permission from [68].

crystallization front, and further explains the small Δt_{LX}. The temperature increase on recalescence was used to estimate the heat release as 52 J/g and was reported on the h_C plot along with the other calorimetric data.

With the data collected from the aforementioned methods, $h_C(T)$ plots are constructed first for 18 < X < 27, while a further discussion will be made for X < 17. Figure 2.6a-d compiles the configurational enthalpy data for these compositions. These data are fit with Equation 2.1 (99.4% correlation) with fitting parameters listed in Table 2.2. From Figure 2.6a-d, the curvature of h_C increases from the fragility index, n, rising along with increasing Angell fragility, m. In X = 18, the isotherm and constant heating rate data report different behaviors in the low-temperature region of the h_C curve. The two data sets have different slopes, but are more vertical than that for the stronger, higher X glasses. In fact, the temperature-corrected constant heating rate data suggest a vertical jump at 551K, indicative of a potential latent heat. This separation from the low T h_C data in X = 20 - 27 marks the higher fragility samples as worth greater inquiry. This will be included in the discussion on X = 14 and 16 samples.

For better comparison, the 18 < X < 27 data were plotted on axes normalized by the isenthalpic temperature (θ_h) and the high temperature limit of enthalpy ($h_C(\infty)$). Figure 2.7 collects the Pt alloy data on one plot and highlights the
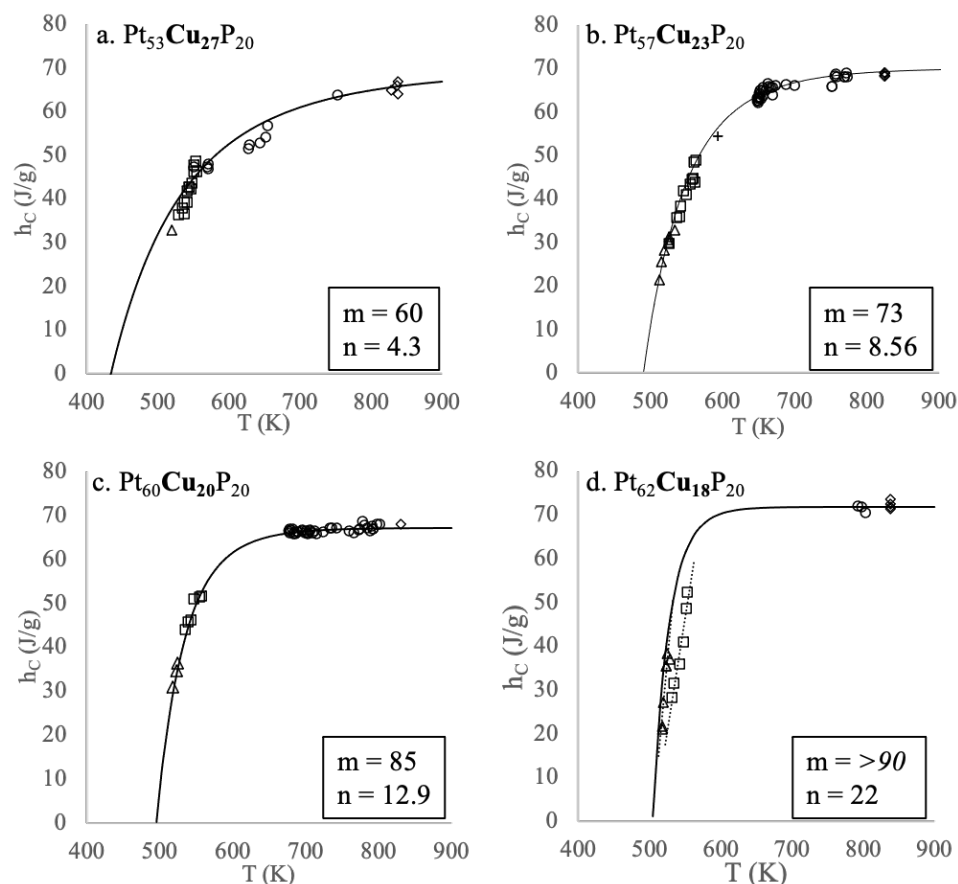
Figure 2.6: h_C data plotted per method and composition. Method key matches that of Figure 2.2. Reproduced with permission from [68].

$Pt_{80-X}Cu_XP_{20}$ (at. %)	$H_c(\infty)$ (J/g)	θ_h (K)	n	m	$T_K(*)$ (K)	$\frac{h_R}{h_C(\infty)}$
$Pt_{66}Cu_{14}P_{20}$	67.9	561.1*	-19.2*	>90	562.1*	0.383
$Pt_{64}Cu_{16}P_{20}$	68.5	560.5*	-28.3*	>90	560.7*	0.360
$Pt_{62}Cu_{18}P_{20}$	72.4	508.3	25.7	>90	517.4	0.360
$Pt_{60}Cu_{20}P_{20}$	68.3	492.2	13.3	85	511.4	0.341
$Pt_{57}Cu_{23}P_{20}$	70.2	484.8	8.36	73	505.5	0.334
$Pt_{53}Cu_{27}P_{20}$	69.9	433.6	4.3	60	472 ± 10	0.266

Table 2.2: Fitting parameters for configurational enthalpy (Equation 2.1) curves in Figure 2.6a-d. Reproduced with permission from [68].
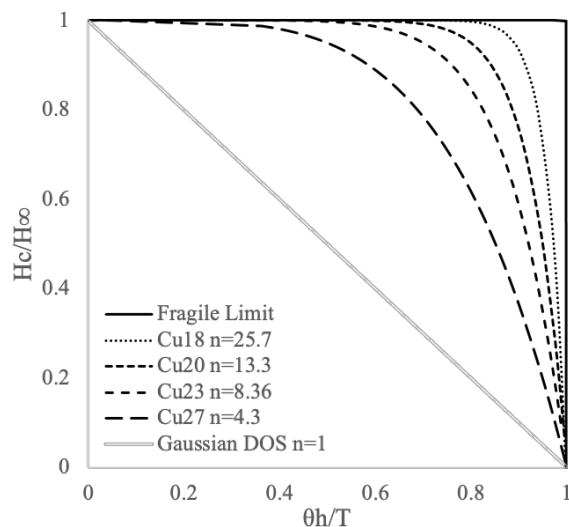
Figure 2.7: Fully normalized h_C plot for composition and n comparison. Method key matches that of Figure 2.2. Reproduced with permission from [68].
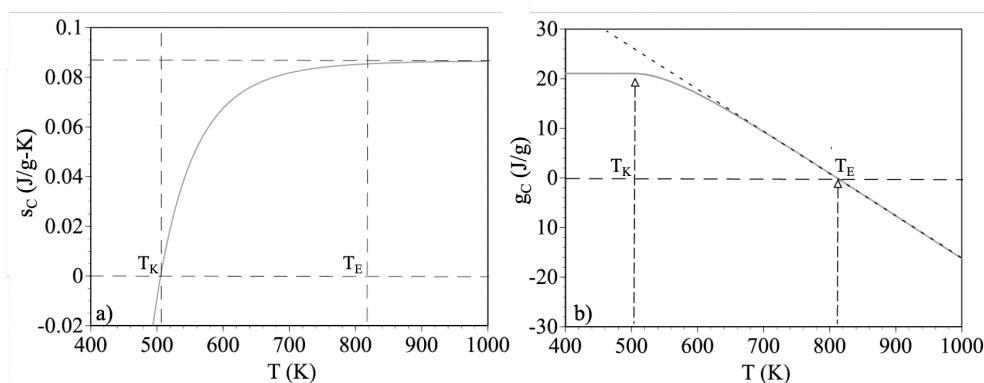
Figure 2.8: Specific configurational entropy (a) and specific configurational Gibb's free energy for $Pt_{57}Cu_{23}P_{20}$. Reprinted with permission from [68].

increase in curvature from n, with increasing fragility, *m*. The plotted *n*'s for PtCuP system increase from $n = 4.3$ and are included in the figure key. Projected at higher fragilities is the fragile limit; the case in which n goes to infinity. In this case, the configurational enthalpy approaches a heavy-side step function and implies possible first-order transition behavior. For context, recall the Gaussian PEL enthalpy Equation 2.1 is described by $n = 1$. The Gaussian enthalpy is superimposed on Figure 2.7 and demonstrates, as expected, that the experimental data deviate greatly from this model. This further demonstrates the Gaussian model inaccuracy and the need for an accurate equation to describe the measured thermodynamics. With 99.8% correlation, Equation 2.1 is a prominent contender.

With the now complete specific configurational enthalpy curves and the excellent analytic fits provided by Equation 2.1, the enthalpy can be integrated to achieve configurational entropy and free energy. The fit of Equation 2.1 to the thermodynamic data was used to analytically compute the specific configurational entropy, $s_C(T)$, and specific configurational Gibb's free energy $g_C(T)$. By integration, the expression of $s_C(T)$ is:

$$s_C(T) = \Delta s_F(T_E) + \int_{T_E}^{T} \frac{h_C(\infty)}{n} \theta_h^n dT T^{n+2} = \Delta s_F(T_E) - \frac{n h_C(\infty) \theta_h^n}{n+1} \left(\frac{1}{T^{n+1}} \right) \Big|_{T_E}^{T} \quad (2.3)$$

where the integration constant is the measured entropy of fusion $\Delta s_F(T_E)$ at the eutectic temperature, T_E. From the configurational entropy, the Kauzmann temperature, T_K, is determined using $s_C(T_K) = 0$ where Δs_F is reported in normalized dimensionless units of $h_C(\infty)/\theta_h$. Figure 2.8a reports the specific configurational entropy for X = 23.

$$T_K = \frac{T_E}{\left[1 + \left(\frac{n+1}{n} \Delta s_F \left(\frac{T_E}{\theta_h} \right)^{n+1} \right) \right]^{\frac{1}{n+1}}}. \quad (2.4)$$

For X = 23, T_K = 505.5K, very close to the calorimetric onset T_g of 505K. Further, it is close to the rheologic T_g onset of 501.5K. To this end, the experimentally defined T_K is effectively indistinguishable from the thermodynamic and rheological glass transition temperatures. The remaining Kauzmann temperatures for the other compositions are listed in Table 2.2 and can be compared with the calorimetric glass transition temperatures reported in Table 2.1.

To attain the Gibb's free energy, we recall that at ambient pressures, the "Pv" term can be ignored (compared with h_C and T_s terms). Therefore $g_C(T) \sim h_C(T) - T s_C(T)$. We assume at T_K the glass configurationally freezes, where below T_K, $s_C(T) = 0$, and $g_C(T) = h_C(T_K)$. From these fits, below T_K, entropy becomes negative (subensemble), suggesting the system runs out of configurational states when frozen at T_K. In Figure 2.8b, $g_C(T)$ remains linear with respect to T down to deep undercooling. This suggests configurational freezing sets in only at very deep liquid undercooling and agrees with the Turnbull approximation for modest undercooling.[8, 69]
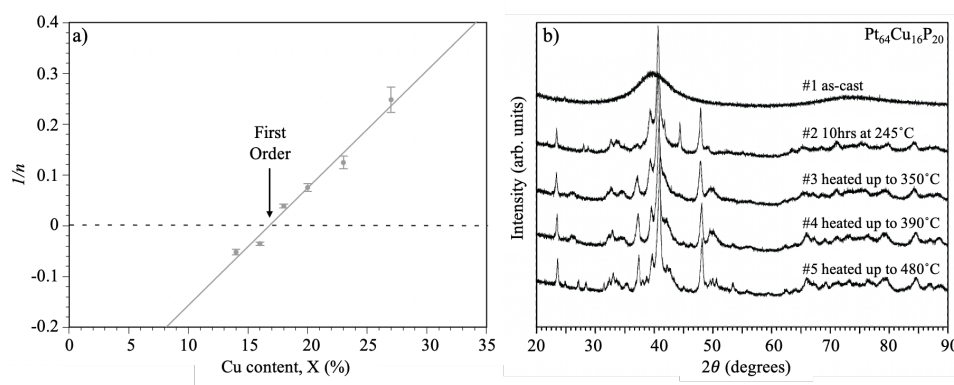
Figure 2.9: Variation of effective glass transition width, $1/n$, with copper content (atomic %) (a). XRD plots for X = 16 (b). Reprinted with permission from [68].

At T_K, the entropy and enthalpy have different behaviors. While the configurational entropy reaches zero at T_K, the configurational enthalpy remains finite. This leaves a residual enthalpy, $h_R = h_C(T_K)$, above that of the crystallized eutectic reference state. This residual enthalpy is calculated relative to the high temperature limit of enthalpy and reported in Table 2.2 under $h_R/h_C(\infty)$. h_R represents the heat of crystallization of a fully ordered ideal glass at T_K, where the configurational enthalpy of the ideal glass lies T_R above that of the crystalline state.

The analysis for $18 < X < 27$ has revealed promising results for configurational freezing and a residual enthalpy, but when comparing the fitting parameters in Table 2.2 to copper content, X, a separation of character occurs at X $\sim$ 17. With n as the thermodynamic fragility parameter of Equation 2.1, $1/n$ represents the relative glass transition (half) width. When $1/n$ is plotted against copper content, X, Figure 2.9a uses a simple linear fit that suggest that n diverges at X $\sim$ 17. This divergence implies the glass transition passes through a critical point and becomes a first-order freezing transition at X = 17, and thus makes the lower copper content samples of particular interest.

When compiling the configurational enthalpy data, the Sn heating-rate onset temperature corrections were utilized. The data for X = 14, 16 from the various methods are summarized in Figure 2.10. When T_C is temperature corrected for the heating rate shift for X = 14 and 16, a clear vertical step emerges. This discontinuous step is a latent heat and indicative of a first-order glass-melting transition. The onset temperature is defined as T_{gm}, effectively the melting temperature of the low-temperature "solid like" glass. For X = 14, T_{gm} = 533K, $\sim$30 K above the nominal calorimetric onset T_g, and the latent heat of the transition is determined to be $\sim$27

Figure 2.10: Specific configurational enthalpy for X = 14 and 16. X = 14 an 16 data and limits plotted with dot-dash and solid lines, and dotted and dashed lines, respectively. Reproduced with permission from [68].

J/g. For composition X = 16, a slightly smaller step discontinuity of ~20 J/g occurs at a somewhat higher T_{gm} = 548K. Both curves display behavior of a latent heat and a first-order glass-liquid melting transition.

These latent heats of ~20 - 30 J/g combine with the data in Figure 2.6a-d to reveal an impressive trend. Between X = 14 and 16, a trend is observed that with increasing X comes an increase in T_{gm} and a decrease in Δh_C. This trend continues into X = 18 as mentioned briefly earlier, and even further in X = 27. Where Figure 2.6a displays a previously overlooked but apparent small vertical jump in configurational enthalpy at 651K. These data and trends are visualized in Figure 2.11. As X traverses the composition range through 14, 16, 18, and 27, T_{gm} and Δh_C are 533, 548, 551, and 651K, and 27, 20, 23.7, and 15.7 J/g, respectively. The absence of the glass-melting transition from X = 20 and 23 samples is attributed to the lack of available data in the mid-ΔT region where the suggested discontinuity would occur. For if the trend is forecast to X = 20 and 23, T_{gm} is anticipated where only RDH measurements can be captured.

Returning to focus on X = 14 and 16, in addition to the enthalpy jump at T_{gm}, Figure 2.10 shows the opposite curvature at low temperatures compared to the 18 < X < 27 compositions. This curvature change makes the current form of Equation 2.1 no longer appropriate. Fortunately, Equation 2.1 can be modified with the gained
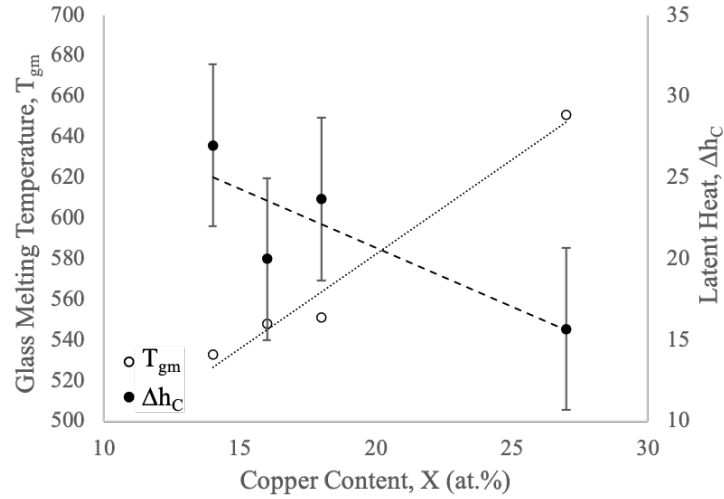
Figure 2.11: An emerging trend with the glass-melting transition. As fragility increases (decreasing X), T_{gm} decreases and Δh_C increases (filled and unfilled circles, respectively). This reveals a larger glass-melting transition in ultra-fragile metallic glasses.

knowledge of the additive residual enthalpy and put into a power law form;

$$\frac{(h_C(T) - h_R)}{(h_C(\infty) - h_R)} = \left(\frac{T}{\theta_h}\right)^n. \tag{2.5}$$

This new equation describes the approach to melting of the glass from below the first-order transition and intersects with the enthalpy of fusion at T_{gm}. With this modified equation, the fitting parameters have shifted as well. θ_h now represents the temperature where the low-temperature $h_C(T)$ curve crosses $h_C(\infty)$, or equivalently (when n is very large) where $h_C(T)$ for the low-temperature solid-like glass crosses the enthalpy of fusion of the eutectic crystalline solid. The n parameter now has a negative sign, which describes the glass freezing. Finally, $h_C(T)$ uses the ideal glass h_R as the natural zero for this adjusted glass enthalpy. With increasing n, Equation 2.5 approaches a heaviside step function from below θ_h. In Figure 2.10, X = 14 and 16 are fitted with the results $n = -19.2$ and -29.2, respectively. The fitting parameters are included in Table 2.2.

The curves in Figure 2.10 predominantly fit isothermal scan data for the ultra-fragile samples below T_{gm}. For X = 14 and 16, the residual glass enthalpies approach h_R of ~26.0 J/g and 24.5 J/g, respectively. The temperature dependence of h_C below T_{gm} suggests that the equilibrium solid-like glass is a configurationally excited state. However, the potential of slow kinetics limiting relaxation and equilibration of
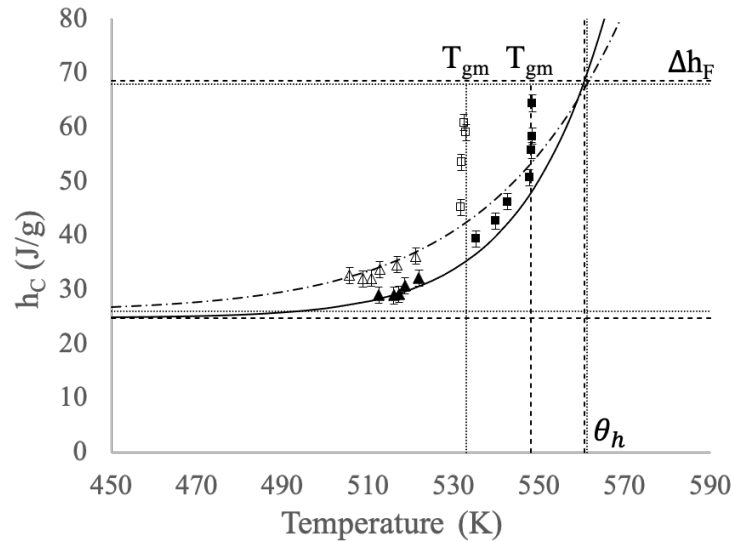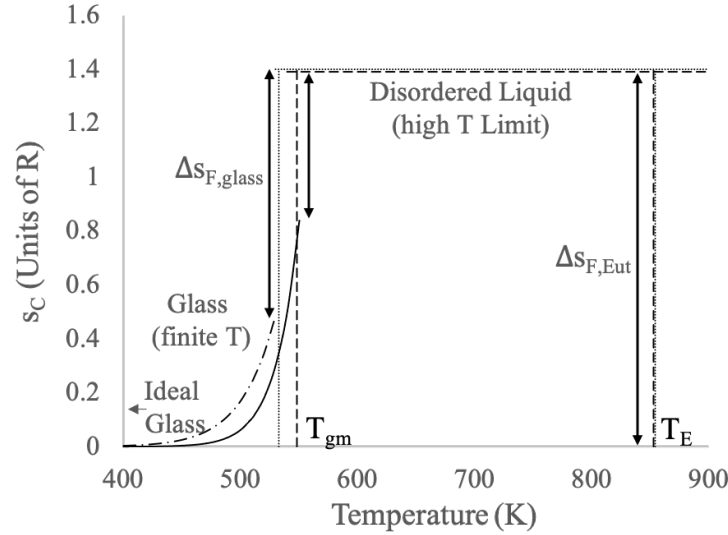
Figure 2.12: Specific configurational entropy for X = 14 and 16. X = 14 and 16 data and limits plotted with dot-dash and solid lines, and dotted and dashed lines, respectively. Reproduced with permission from [68].

the glass below T_{gm} is unlikely. Particularly since the data were collected under isothermal conditions with anneal times exceeding the Maxwell relaxation time by orders of magnitude. Therefore, with assuming the data represent a well-equilibrated glass, Equation 2.5 can be used to compute the configurational entropy.

Using the fits of Equation 2.5, the entropy is calculated by integration of $\Delta h/T$ from low-temperature where $s_C = 0$ to temperature T_K^*. T_K^* describes an "inverse" Kauzmann temperature. In effect, this temperature is where the glass configurational entropy extrapolates to the entropy of fusion of the crystalline eutectic alloy, i.e., where $s_C(T_K^*) = \Delta s_F$. The configurational entropy for X = 14 and 16 is plotted in Figure 2.12. The equation for T_K^* is summarized as follows:

$$T_K^* = \theta_h \left[\frac{(n-1)(h_C(\infty) - h_R)\theta_h}{n h_C(\infty) T_E} \right]^{1/(n-1)}. \tag{2.6}$$

T_K^* functions as an upper bound for the glass-melting temperature and is slightly lower for X = 14 than for X = 16, implying a more restrictive upper bound on the highest fragility sample tested.

For the overall specific configurational entropy as a function of T, a piece-wise continuous function is constructed as shown in Figure 2.12. The piece-wise plot combines the fits of measured latent heat of glass-melting at T_{gm} and the entropy of

fusion of the crystalline eutectic. The figure shows $s_C(T)$ in units of the gas constant, R, for X = 14 and 16. Within the above assumptions, for X = 14, the configurational entropy at T_{gm} is 0.0308 J/gK or 0.533 R. Equation 2.5 provides a description of glass entropy from T = 0K to T_{gm}. With the curvature present in the ultra-fragile X = 14 and 16 samples, the equilibrium glass configurational entropy never becomes negative, but rapidly approaches that of the crystallized eutectic solid as T falls below T_{gm}. For the solid-like glass, the configurational entropy, $s_C(T)$, at T = 0K vanishes within uncertainty of $\sim \pm 0.03R$. Thus, within the stated uncertainties, the Kauzmann paradox is resolved where $s_C(T)$ obeys the third law of thermodynamics for the solid-like glass phase. Effectively, the solid-like glass behaves much like a crystalline solid but with a smaller heat of formation for configurational excitations per Equation 2.5.

It is important to recall that phonon/vibrational contributions to the total entropy have been excluded from this analysis (as these are assumed to be roughly equal for both the glass and crystalline states in the temperature range of interest). While crystallization data technically include contributions arising from anharmonic differences between the glass and crystalline states, they are apparently small by comparison to configurational differences. This is understood because anharmonicity displays a "T^2" contribution to the enthalpy of crystallization, but the high n values are in stark contrast to this potential contribution. Therefore, Equation 2.5 and high n values strongly suggest that these anharmonic contributions are relatively small and realistic to exclude. Therefore configurational degrees of freedom are expected to dominate the temperature dependence of specific enthalpy below T_{gm}.

In effect, the ordered glass can be viewed as a configurationally ordered solid, but with an infinite unit cell. It makes sense that this configurationally ordered glass has a distinct configurational ground state enthalpy, h_R, differing from that of the eutectic crystalline solid. As discussed in Section 1.4, allotropes and polymorphic crystals have ordered phases with phase-specific ground state energies. This is a reasonable extension to a fully ordered solid-like ideal glass state as well.

2.5 Summary and Conclusion

The $Pt_{80-X}Cu_XP_{20}$ system was a key part of this thesis research, and demonstrates several prominent results. The homogeneous liquid exerts a single sharp crystallization event following coupled eutectic growth. This crystallization produces a well-defined crystalline reference state and allows for a direct and accurate measure of

the liquid enthalpy relative to that reference state. Before testing, the $Pt_{80-X}Cu_XP_{20}$ system achieves a verified configurationally relaxed metastable state. The incubation time before crystallization, t_{LX}, exceeds the Maxwell relaxation time, $\tau_\alpha = \tau_M$ by several orders of magnitude, thus indicating the required metastable equilibrium of the liquid is achieved before crystallization onset. Together, these features allow an accurate assessment of the metastable equilibrium configurational enthalpy of the liquid in reference to the crystalline eutectic solid. These features justify the application of classical thermodynamics to compute the state functions of the liquid phase.

The thermodynamic functions obtained from this work revealed the specific configurational enthalpy departs drastically from the $1/T$ temperature dependence expected in the PEL Gaussian model. In actuality, $n = 1$ represents the Gaussian Landscape model in Equation 2.1, but the magnitude of n is much larger for the reported high-fragility and ultra-high fragility PtCuP samples. With Equation 2.1 and its modification to Equation 2.5, this implies the density of inherent states approaches a simple exponential behavior for $W(\phi)$ and is not Gaussian (see discussion in Chapter 1). With Equation 2.1, with increasing n, we see a divergence in heat capacity at $T = \theta_h$. Similarly, the glass transition approaches first-order melting behavior as $1/n$ approaches zero. For X = 14 and 16, one observes clear evidence of a latent heat and first-order melting behavior of a solid-like glass to a fluid-like state. Equation 2.5 accounts for the residual enthalpy as one approaches the melt transition at T_{gm} from below. Within measurement error and the assumptions of this work, a discontinuous enthalpy (latent heat) is observed at a well-defined temperature T_{gm} for X = 14 and 16 compositions. This provides distinct evidence of a first-order melt transition of this ordered ideal glass to a disordered liquid state where the liquid appears to be in its high-temperature limit just above T_{gm}. For configurational entropy, the solid-like glass follows a power law up to T_{gm}, but approaches zero (within error) as temperature approaches zero. Thus, within the error and the assumptions of this work, the ultra-fragile liquid averts the Kauzmann paradox through a first-order freezing transition, and the configurational entropy obeys the third law of thermodynamics below the glass freezing temperature.

Ultra-fragile glasses demonstrate a distinct latent heat and glass-melting transition temperature where a solid-like glass melts to a liquid-like phase. It is important to note that both of these phases are non-crystalline (Figure 2.4). As X increases, however, the latent heat decreases while the melting temperature increases. The

first transition is most clearly established for the X = 14 and 16 samples, but further inspection of X = 18 and 27 reveal a possible continuation of the trend seen at lower X. While T_{gm} continues to increase, the latent heat gets smaller, making the transition more difficult to discern for the stronger, higher Cu-content glasses. Furthermore, T_{gm} moves into the ΔT data gap, where existing methods either do not allow measurements, or data are very difficult to collect (requiring RDH), and so limited data exist. This explains why this possible transition is not identifiable in higher Cu X = 20 and 23. In effect, these data identify the glass-melting transition across the $Pt_{80-X}Cu_XP_{20}$ composition landscape, and provide evidence that this transition may exist in both stronger and highly fragile glasses.

These claims of a configurationally ordered glass are supported by Molecular Dynamics (MD) results by Berthier *et al.* and An *et al.* Berthier *et al.* have reported ultrastable (configurationally relaxed) atomic glasses that exhibit first-order melting on rapid heating through T_g.[70, 71, 72]These glasses are prepared by simulation of layered atomic deposition onto heated substrates (near T_g). This allows for a degree of configurational relaxation not thought possible on cooling of a monolithic liquid.[70, 71] Bethier's MD simulations showed a first-order melting front propagation similar to direct melting of crystals and similar to the results reported here for the PtCuP system. The MD analysis concluded the first-order melting arose from the highly-ordered low configurational enthalpy ultrastable glass. It is believed that the present work observes a similar highly-ordered low configurational enthalpy/entropy ultrastable glass in the ultra-fragile $Pt_{80-X}Cu_XP_{20}$ samples.

Further, the findings in this work are connected to the metastable structural and energetic intermediate G-phase glass state in An *et al.*'s works described in Section 1.4. It is believed the PtCuP metastable configurational equilibrium solid-like glass state is equivalent to the G-glass phase glass state reported from the MD simulations, while the fluid-like phase in the X = 14, 16 case is equivalent to the L-phase glass/liquid identified by An *et al.* The presence of the glass-melting transition provides a natural starting point to explore mechanical and other characteristic properties on either side of the first-order glass-melting transition. Attempts to follow this line of investigation are reported in the next chapter where the possible connection to the G-glass (and L-glass) is further strengthened.

Chapter 3

CHARACTERIZATION OF THE SECONDARY GLASS PHASE IN ULTRA-FRAGILE $Pt_{80-X}Cu_XP_{20}$ BULK METALLIC GLASS

3.1 Abstract

Work in Chapter 2 and Shen *et al.* describe a secondary G-phase glass-forming on annealing.[68, 65] The results discussed in this chapter pinpoint a divergence in formation mechanism at ultra-high fragility, uncaptured by these previous works, while showing additional evidence for the glass-melting transition.

After the discovery of the first-order glass-melting temperature T_{gm} as discussed in Chapter 2, characterization between the as-cast and configurationally relaxed and equilibrated reference glass state (annealed) were completed. Evidence suggests a divergence of formation criteria for the secondary glass phase at ultra-high fragility. This evidence arises from a hardness cusp and cusp shift at X = 18. The hardness jump in high X but not low X indicates different structures from annealing in high X, but consistent structures at low X. As such, ultra-fragile samples achieve the secondary glass on quenching, but less fragile samples see the secondary glass forming with annealing. When samples were explored for amorphous behavior, both as-cast and annealed samples showed no crystallinity. However, while all samples suggest ordering via a reduced FWHM of the amorphous band, high-X samples tend to order more. This is consistent with high-X samples growing the secondary phase on annealing and low-X samples quenching in the secondary phase for a smaller ordering effect. Finally, multifaceted evidence of a glass-melting transition is collected across multiple works. Chapter 2 introduced the glass-melting transition at T_{gm} as manifested in configurational enthalpy. The current work uses DSC scans at 20K/min to reveal the onset of glass-melting in the ΔT region. While the transition does not complete in the allotted time before crystallization intervenes, rapid capacitive discharge studies allow visualization of the same effect, collecting further evidence for a glass-melting transition of the secondary glass phase.

3.2 Introduction

This work serves as an extension to a key finding of the previous chapter; annealed ultra-fragile $Pt_{80-X}Cu_XP_{20}$ displays an emergent latent heat as a glass-melting transition of a secondary glass phase. Both Chapter 2 and work by Shen *et al.*

characterized a secondary glass as grown and present in annealed samples.[68, 65] However, An *et al.*'s work on ultra-fragile pure Ag revealed the secondary glass (G-phase) forms on quenching or isothermal evolution in the moderately undercooled melt. This suggests a transition point in the fragility landscape, across which the secondary glass forms via different mechanisms. The present work explores properties across this potential fragility-dependent formation mechanism. Properties are explored as a function of fragility to determine if heat treatments lead to different behavior.

This work will use the $Pt_{80-X}Cu_XP_{20}$ system to characterize the difference between the as-cast and configurationally relaxed and equilibrated reference glass state (annealed). All measurements are completed across the fragility range available to the $Pt_{80-X}Cu_XP_{20}$ system. In this study, X includes 14, 18, 20, 21.5, and 23. Given this is the same alloy system as in Chapter 2, readers are referred to Section 2.2 for the advantages of using the $Pt_{80-X}Cu_XP_{20}$ high-fragility BMG system.

The existing reports of secondary glass formation include a number of marked differences between the two glass phases. Particularly, while both glass phases are amorphous or non-crystalline, the works by Shen and An report a 20 and 30% increase in hardness on transforming from the typical L-glass to the MGG or G phases, respectively.[65, 62] Shen also describes the T_g of their MGG as 18K higher than the traditional (L-phase) as-cast glass T_g.[65] As such, these properties will be explored via Vicker's indentations, X-ray diffraction, and DSC thermal scans across the sample processing conditions and fragility landscape.

3.3 Methods

Sample Preparation

Samples were cast by water quenching in quartz tubes. Compositions X = 18 – 23 were produced in 3-mm fixed-diameter tubes. The X = 14 sample was quenched in quartz-drawn capillaries up to 1mm in diameter. Fluxing is not necessary to produce the glass for these samples. Samples were sectioned from the cast rods to 4 and 8-mm lengths for the 3-mm diameter and capillary pieces, respectively. The samples were then cleaned before the next sample preparation steps. Sample cleaning procedure included 10 minute sonication in baths of acetone and ethanol with three rinses with the respective solvent before each sonication. Half the specimens were then annealed at T_g for 15 hours in a horizontal tube furnace (X = 18 – 23) or 3 hours in a Perkin Elmer DSC 7 (X = 14). The ultra-fragile X = 14 was annealed in the DSC due

to higher available temperature control. Once cleaned, all samples were embedded in epoxy pucks where the puck height is < 9mm to enable mounting in the XRD sample holder. The pucks were ground at 400 grit until flat. Subsequent polishing went from 400-grit to 1 μm grain size. Grinding and polishing were completed with a Buehler autopolisher (ecomet 3 variable speed grinder-polisher equipped with an automet 2 power head). X = 18 – 23 samples were stood on end for a 3-mm diameter exposed polished surface. X = 14 samples were laid on their side for a 1 x 8-mm exposed cross section along the length of the rod. This provides sufficient surface area for X-ray scans and indentations. Once polished, the surface was wiped with isopropyl alcohol using a kim wipe to assure no debris was present.

X-Ray Diffraction

A Panalytical X'Pert Pro was utilized for all XRD scans. X = 18 – 23 samples underwent 1-hour scans, and X = 14 samples 7-hour scans. The longer scan time was utilized to achieve better signal to noise ratio due to the smaller sample size. Given XRD samples were cast in carbon-based epoxy pucks, once mounted with putty, the puck was masked-off with corning glass coverslips (thickness 2 18x18, cat no. 2855-18) to block the carbon puck diffraction maxima at 26, 42–45, 50 and 54 °(2θ). Figures 3.2 and 3.3 show no carbon puck background peaks. A figure of this layout is included in Appendix Figure C.1.

Vicker's Hardness and Optical Imaging

Hardness indentations were completed in a LECO LV810AT Oprical Scope and Hardness Tester using a 4.903N force and 5s dwell time. Indentations averaged around 50-μm across. Indentations were completed with the sample embedded in the epoxy puck to assure a level surface for accurate indentations. General surface images were captured before indentation at 10x magnification. Apparent topography contrast was most visible, if not *only* visible, at 10x magnification.

Differential Scanning Calorimetry

A Perkin Elmer DSC 4 was utilized for all thermal scans. Summary scans are displayed from 100°C through melting. This starting point is chosen to remove the consistent errors at temperatures < 100°C arising from transient effects on heating to remove any confusion for the reader. Scans from room temperature through melting (600-700°C) at a 20 K/min constant heating rate were utilized. A background scan was conducted with a sapphire reference immediately before the test run. This
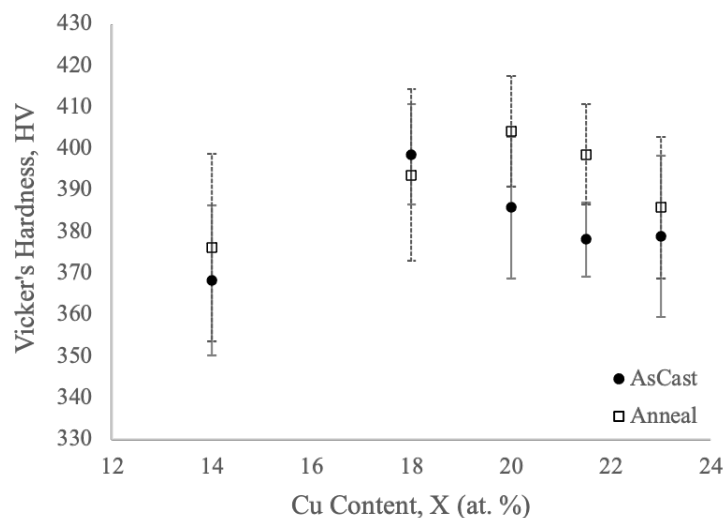
Figure 3.1: Vicker's Hardness data varying with composition and heat treatment. Solid and dotted error bars are for as-cast samples and annealed samples, respectively.

background scan was taken as the baseline and removed. Analysis utilized the Sn onset temperature corrections from Table B.1. These corrections were carried out on a Netzsch DTA 404C, and are assumed to approximate corrections at 20 K/min for the Perkin Elmer DSC 4 data.

Rapid Capacitive Discharge Heating

Rapid capacitive discharge heating (RDH) was used to measure data in the mid-ΔT region. The system uses ohmic dissipation with 15-kJ capacitive discharge heating on rod samples 3-cm in length and ranging from 3 to 5-mm in diameter. Samples were uniformly heated at heating rates up to $\sim 10^5$ K/s by fully discharging a capacitor bank from various charging voltages to vary the energy deposited in the sample rod. The sample is clamped between two copper electrodes. Temperature was measured with the Impac series 5 non-contact high-speed pyrometer with a 5 μs time resolution. A FLIR SC-4000 infrared camera was combined with the RDH system for infrared images of coupled eutectic growth (see Figure 2.5). The infrared camera functions with 256,000 pixels and frame rates up 1,300 frames/s.

3.4 Results and Discussion

The as-cast and annealed samples were first explored using hardness measurements. Vicker's hardness measurements in Figure 3.1 suggest an apparent annealing effect

		Cu_{14}	Cu_{18}	Cu_{20}	$Cu_{21.5}$	Cu_{23}
As	HV Ave	368.27	398.58	385.80	378.10	378.92
Cast	HV Stdev	18.13	12.11	17.02	8.83	19.39
Anneal	HV Ave	376.21	393.59	404.23	398.58	385.80
at T_g	HV Stdev	22.5	20.65	13.33	12.11	17.02
	%ΔHV	2.16%	-1.25%	4.78%	5.42%	1.81%

Table 3.1: Vicker's Hardness (average and standard deviations) with nearrest neighbor (nn) distance in Angstroms for $Pt_{90-X}Cu_XP_{20}$ compositions. Column headers are abbreviated with Cu_X values.

at high X (lower fragility "*m*"), but, within standard error, there is no discernible effect at low X (ultra-fragile). The standard error is taken as the standard deviation from 25 independent indentations. For X = 20, 21.5, and 23, average hardness values increase from 385.80, 378.10, and 378.92 HV to 404.23, 398.58, and 385.80 HV, respectively. These samples experience, on average, a ~4% increase in hardness. This increase is not as great as that reported in other multi-phase glass works that report an ~20 - 25% jump from the computational L-glass to the G-glass by An *et al.*, and 20% for the as-cast to MGG phase by Shen *et al.*[62, 66, 67, 65] But interestingly, the ultra-fragile samples that exhibited the first-order glass-melting transition in Chapter 2 do not show any significant increase in hardness (any variance is well within experimental error). Where the glass-melting transition occurs in the X < 18 samples in the configurational thermodynamics study, a cusp is observed in hardness at X = 18 for as-cast samples. This cusp persists in the annealed samples, but appears to shift from X = 18 to 20. This cusp shift suggests X = 18 is some sort of structural transition point, where the annealed structure is quenched-in on casting for the ultra-fragile low-X compositions. This similar transition point (composition and fragility (m > 90) suggests the low-X as-cast samples undergo the same anneal-induced transition as the high-X samples, but transform instead during the quench. This suggests the as-cast and anneal states at low X are both in the same glass state. Indentation data are summarized in Table 3.1.

To investigate this behavior and potential evolution during annealing, X-ray diffraction scans were conducted on both the as-cast and annealed samples. XRD scans report amorphous behavior across composition in both sample systems; the as-cast and annealed scans are displayed in Figures 3.2 and 3.3, respectively. The full width at half maximum (FWHM) of the amorphous band is utilized to determine if ordering/structural change of the glass occurs during annealing. A narrowing of the
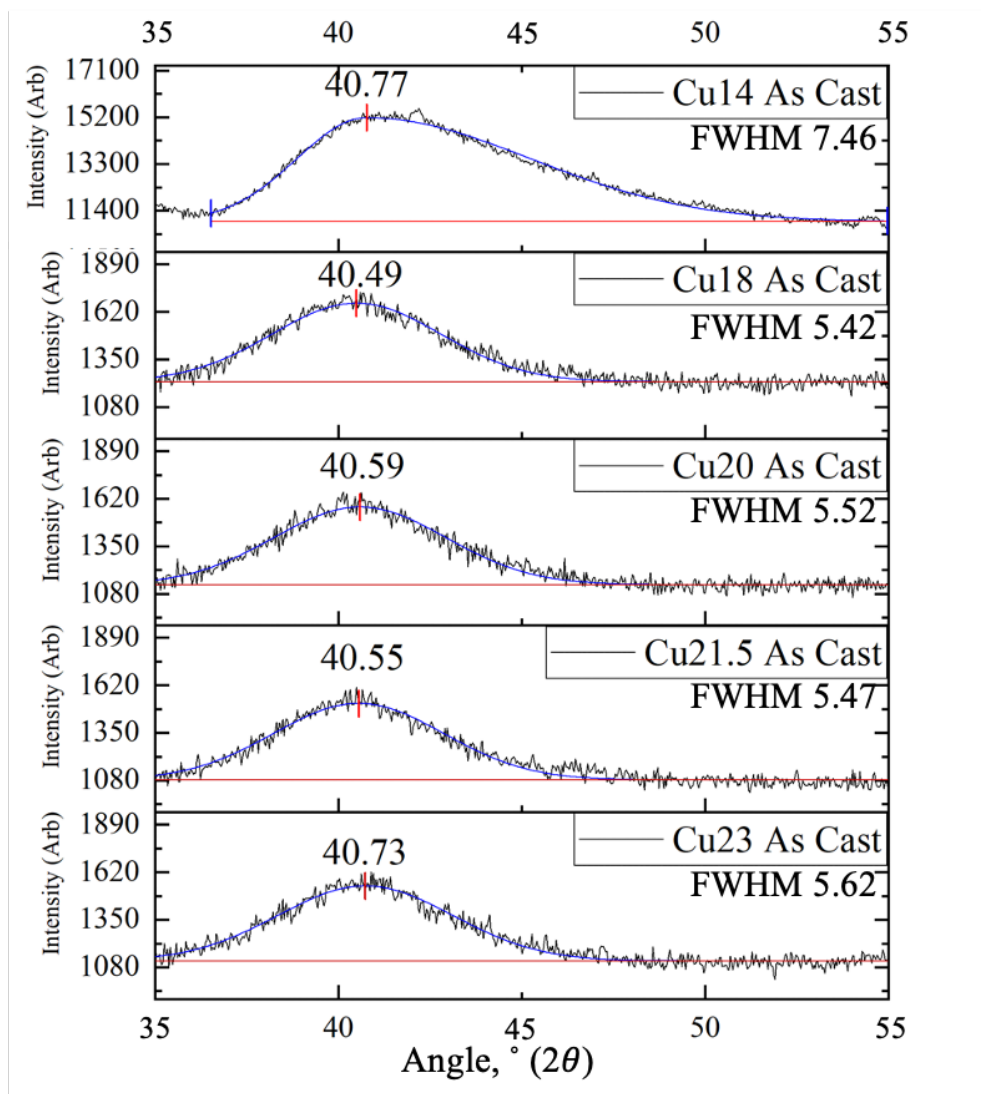
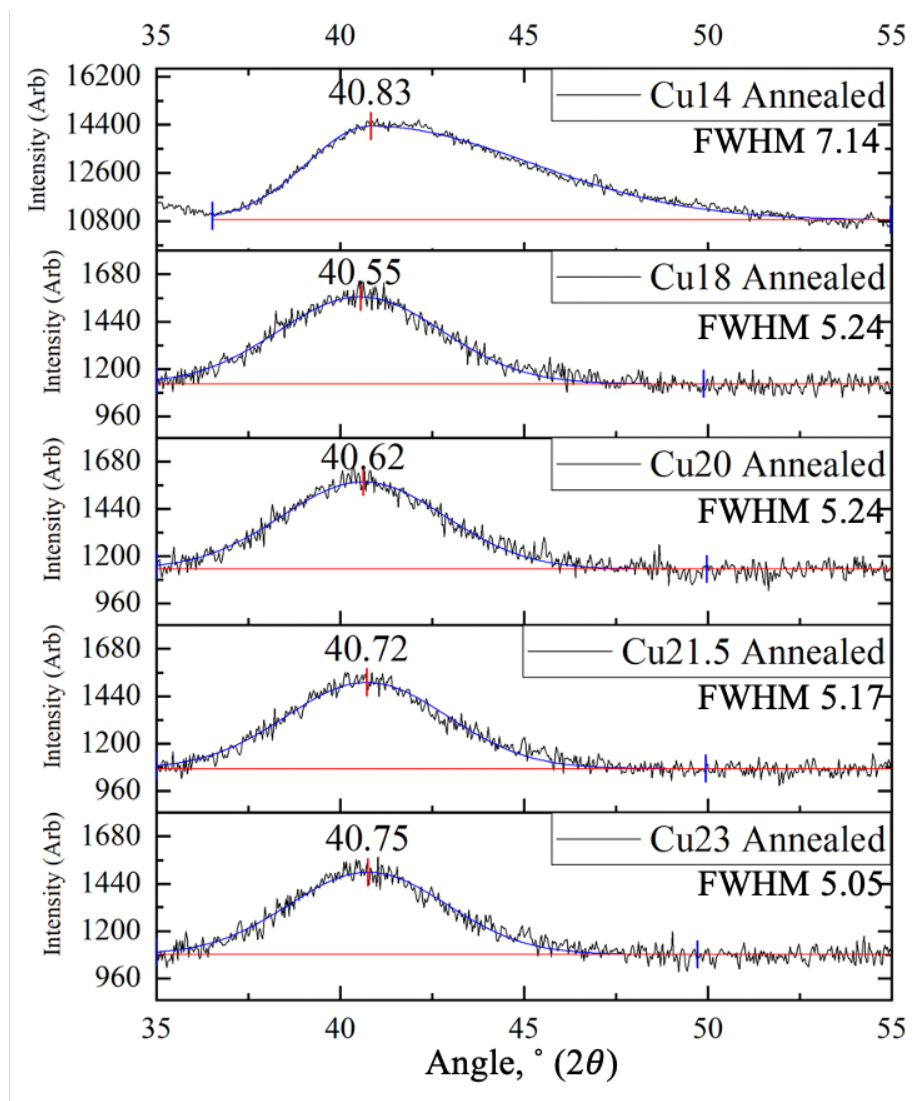Figure 3.2: As-cast X-Ray diffraction scans for X = 14 – 23. Samples increase in X from top to bottom.

Figure 3.3: Annealed X-Ray diffraction scans for X = 14 – 23. Samples increase in X from top to bottom.

		Cu_{14}	Cu_{18}	Cu_{20}	$Cu_{21.5}$	Cu_{23}
	Peak (°2θ)	40.771	40.448	40.558	40.548	40.727
As	FWHM	7.459	5.417	5.522	5.471	5.623
Cast	d (Å)	2.213	2.228	2.223	2.225	2.150
	nnd (Å)	2.722	2.740	2.734	2.736	2.725
	Peak (°2θ)	40.827	40.548	40.622	40.721	40.747
Anneal	FWHM	7.143	5.243	5.238	5.175	5.047
at T_g	d (Å)	2.210	2.225	2.221	2.216	2.214
	nnd (Å)	2.728	2.736	2.732	2.725	2.723
	ΔPeak (°2θ)	0.139%	0.148%	0.084%	0.427%	0.049%
%	ΔFWHM	-4.234%	-3.198%	-5.140%	-5.418%	-10.237%
Change	Δd	-0.133%	-0.142%	-0.081%	-0.407%	-0.047%
	Δnnd	-0.133%	-0.142%	-0.081%	-0.407%	-0.047%

Table 3.2: Vicker's Hardness (average and standard deviations) with nearest neighbor (nnd) distance in Angstroms for $Pt_{80-X}Cu_XP_{20}$ compositions. Column headers are abbreviated with Cu_X values.

amorphous band and therefore a decrease in FWHM suggest ordering of the amorphous system, in analogy to how crystal grain growth yields narrower peaks. The high-X compositions show a 5 - 10% decrease on annealing, while the low-X (X $\leq$ 18) samples show a 3 - 4% decrease (Table 3.2). This suggests that the high-X samples undergo a greater ordering effect with annealing that could contribute to their observed larger hardness increase. This further supports the idea that the low-X samples are already predominantly in the G-phase solid-like glass following initial casting.

In continued analysis of the XRD data, the estimated nearest neighbor distance (nnd) and its relative change are quantified to determine if the atomic environment changes on annealing over the range of X. These changes are reported in Table 3.2. To calculate an "effective" nearest neighbor distance, the d-spacing of the first diffraction maxima is calculated from the peak angle by rearranging the Bragg equation from

$$n\lambda = 2d \sin \theta, \tag{3.1}$$

to

$$d = \frac{n\lambda}{2 \sin (\theta/2)}. \tag{3.2}$$

Where *d* is the plane spacing, *n* the diffraction order, λ the radiation wavelength, and $\theta/2$ the angle from the surface normal.[3] The nearest neighbor distances, *nnd*, may then be estimated using the "Debye" formula where *nnd* = 1.23d and are reported in Table 3.2.[73] The estimated nearest neighbor distances all decrease on annealing, but do not show an obvious trend between the low- and high-X compositions.

Given the ultra-fragile samples display a different hardness response to annealing, thermodynamic scans via Perkin Elmer DSC 4 were utilized to investigate their thermal response. It is important to note that the thermal scans in this chapter follow a different protocol than those in the previous chapter. All samples in Chapter 2 were annealed at T_g then immediately heated. Since those samples were not returned to room temperature before heating, the thermal trace was not captured near T_g, and the normal heating response associated with the ΔT region was not observed. Figures 3.4 and 3.5 show the 20 K/min thermal scans from 100°C through melting at ~600°C. The inset (c) of each figure highlights the ΔT region and its peculiarities arising in the case of the annealed samples, and in particular, in the ultra-fragile X = 14 sample.

In Figure 3.4, the as-cast X = 18 sample shows a typical jump in apparent heat capacity beginning at ~230°C and ending at ~250°C. This is the normal thermal signature of the glass transition generally seen in an as-cast metallic glass. The annealed sample, however, shows a sharper glass transition accompanied with an enthalpy recovery peak.[74, 75] Enthalpy recovery is typical of a glass relaxed near T_g then reheated as discussed by Busch *et al.* In the case of X = 14 in Figure 3.5, similar to X = 18, one observes a typical rise in heat capacity at T_g for the as-cast sample. The annealed sample also shows an enthalpy recovery peak as in the X = 18 case. For the annealed sample, however, a second new peak emerges beyond the enthalpy recovery peak in the ΔT region. The inset (c) highlights this region and not only shows the T_g heat capacity rise and enthalpy recovery, but also shows a well-defined second endothermic peak before the onset of crystallization. The author proposes this endothermic peak arises from the onset of the first-order glass-melting transition equivalent to the transition at T_{gm} described in Chapter 2 (see Figure 2.10). The onset of melting during the scan is apparently interrupted by crystallization of the melting solid-like glass, which causes the overall DSC signal to turn sharply exothermic. Since crystallization interrupts this melting transition, the true size of the apparent melting peak is much larger than visualized in the figure, and the t_{peak} temperature would be shifted higher. Even so, the unusual endothermic

Figure 3.4: Thermal (DSC) scans for X = 18 at 20K/min. Scan of as-cast sample (a) and annealed sample (b). The glass transition peak in the anneal sample is enlarged (c). Transition temperatures are printed in Table 3.3.
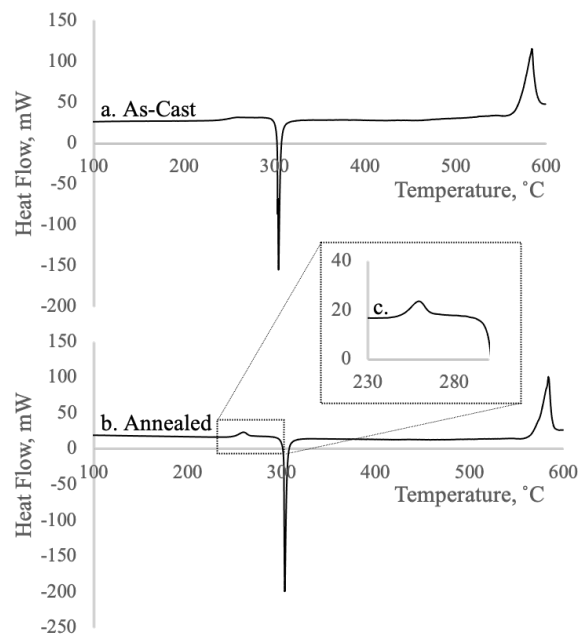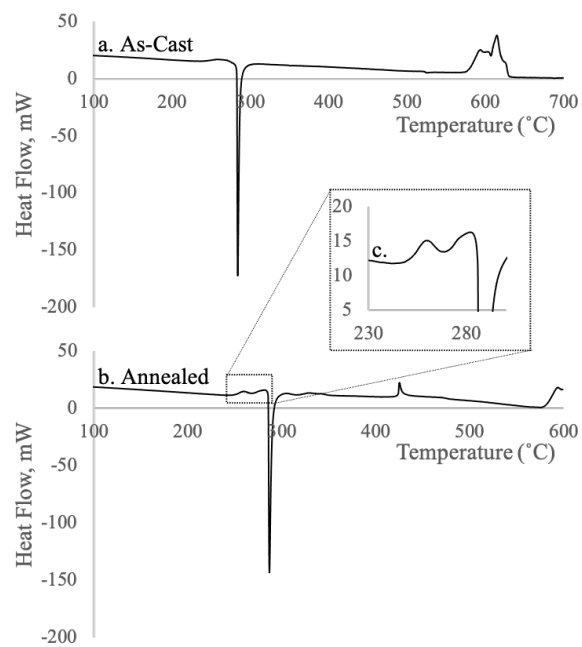

Figure 3.5: Thermal (DSC) scans for X = 14 at 20K/min. Scan of as-cast sample (a) and annealed sample (b). The glass transition peak and glass-melting transition are enlarged (c). Transition temperatures are printed in Table 3.3.

		T_g (K)	T_{gm} (K)	T_x (K)
Cu_{14}	As-Cast	241.04	-	282.81
	Anneal	250.53	270.60	285.68
Cu_{18}	As-Cast	239.24	-	302.39
	Anneal	249.49	-	302.17

Table 3.3: Temperatures and enthalpy values for X = 14 and 18 thermodynamic scans. Temperatures before correction by -11K from Table B.1.

behavior is a strong indicator of the onset of the glass-melting transition. When this representative T_{gm} is compared to that from Chapter 2's ultra-fragile configurational enthalpy plots (Figure 2.10), a similar temperature emerges. Chapter 2 reports T_{gm} at 533K = 260°C for X = 14. Figure 3.5c indicates the approximate T_{gm} peak at 270°C, but corrects to 259°C utilizing the transient correction for the 20 K/min heating rate (Table B.1). This suggests promising evidence that these DSC scans capture at least the onset of configurational melting in the ultra-fragile glass.

Further investigation of this phenomenon requires suppressing crystallization so that the apparent melting transition can be observed separately. Based on the work in Chapter 2, one would expect that using a higher heating rate for the annealed X = 14 sample could prove useful. As such, the RDH method was employed to heat the annealed sample at very high rates. Such RDH data were displayed earlier in 2.5. Figure 2.5 highlighted crystallization by coupled eutectic growth present from t = 0.60 - 0.85s. However, a previously overlooked phenomenon from t = 0.10 - 0.60s is related to the melting onset in Figure 3.5c. Given that melting is an endothermic phenomenon, one expects a cooling behavior on melting when the solid-like low-temperature glass phase is rapidly heated above its glass-melting point, T_{gm}. Under such conditions, the overheated solid-like phase will absorb heat as it melts, thereby cooling until the temperature reaches T_{gm}. In the overheated solid-like phase, the melting front would appear as a cooling front as it traverses the sample. In fact, snapshots of such a cooling front were captured via high-speed pyrometer and are compiled with the temperature-time trace (purple) in Figure 3.6ab. When these snapshots are compared with the thermal trace and glass-melting behavior as discussed in Chapter 2, consistent behavior is observed. That is, following rapid heating of the solid-like phase far above its T_{gm}, a spontaneous cooling front propagates across the sample prior to the onset of crystallization. This is immediately followed by crystallization at 0.60s just as melting (the cooling front)
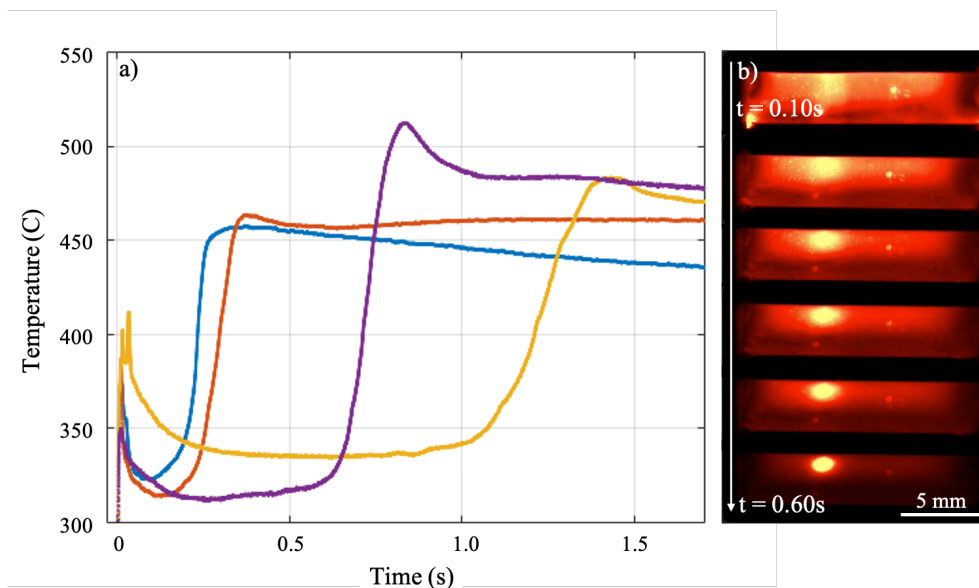
Figure 3.6: Ohmic heating via rapid capacitive discharge. Temperature traces versus time across various energy releases (a) and the accompanying ultrafast thermal camera images from t = 0.1 - 0.6s for the purple trace.

completes. At t = 0.60s crystallization by coupled eutectic growth takes over and the behavior follows that already displayed Figure 2.5b. Multiple RDH thermal traces were collected using the pyrometer at higher RDH energy inputs. At the higher energy inputs (see yellow curve in Figure 3.6a), a T_{gm} peak behavior emerges followed by further overheating of the X = 20 annealed sample (solid-like phase) to 410°C. This overheated solid-like phase then melts and cools back toward T_{gm} as the sample absorbs the latent heat of fusion on melting. The initial heating peak reaches ~400°C, cools to 385°C due to enthalpy recovery, then finally heats to 410°C as the RDH energy discharge is completed. This is followed by dramatic cooling to ~335°C as the overheated solid-like phase melts. Cooling by ~75°C of the overheated solid-like phase corresponds to excess heat absorption of ~3 kJ/mole (assuming an average estimated heat capacity of the overheated solid-like phase is ~40 J/mole-K as suggested by the results of Chapter 2), or roughly 20 J/g in the case of PtCuP at X = 20. With the latent heat only 2.7 kJ/mol, the excess 3 kJ/mol is sufficient to adiabatically melt the entire solid-like glass phase. This peak pattern also mirrors that observed by DSC in Figure 3.5c. Due to the much lower heating rate, the annealed sample is far less overheated in the case of the DSC work, so the melting rate is much lower and thus interruption by crystallization is observed.

One additional observation worth noting is that a peculiar topography arises when
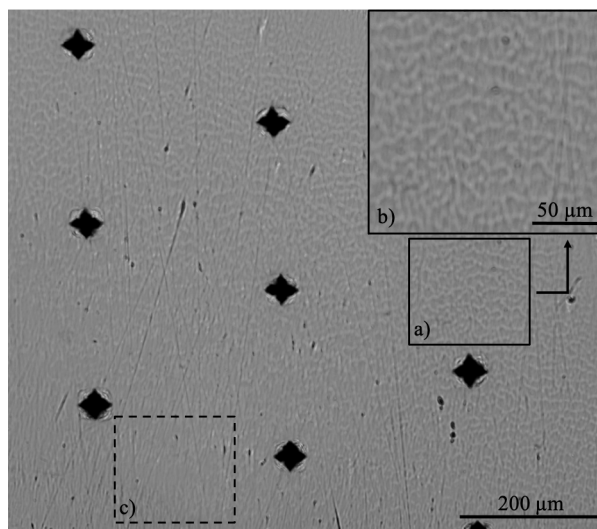
Figure 3.7: Peculiar topography for X = 18 annealed for 24 hours.

the X = 18 is annealed for longer time; i.e., 24 hours, but still within the incubation crystallization time t_{LX} and several orders of magnitude above the Maxwell relaxation time τ_α. Pictured in Figure 3.7ab, this topography shows a structural heterogeneity on the order of 10's of microns compared to the typical surface highlighted in 3.7c. This heterogeneous topography covers roughly half the sample and spreads from the center toward one edge. The scale of this heterogeneous pattern is significantly smaller than the Vicker's diamond (50-μm across), so accurate hardness measurements of the lighter and darker regions were not possible at this indent resolution. However, it is hypothesized that the lighting contrast is from a minor hardness-induced height difference revealed on polishing. This topography is visible at 10x magnification through a single wavelength (green) optical scope. The topography is not readily visible at 20 or 40x. While of a greater length scale, the author believes it is worth noting that this heterogeneity bears a similar resemblance to the G-phase structure in An *et al.*'s Ag, CuAg, and CuZr works.[62, 66, 67] This topography is distinct from typical crystalline dendritic growth.

3.5 Summary and Conclusions

Existing published works describe a secondary glass phase that forms during annealing.[68, 62, 65] The present work investigates the properties on either side of the believed heat treatment-induced transition for as-cast and annealed $Pt_{80-X}Cu_XP_{20}$ samples. Vicker's hardness presents an annealing effect at high X as a ~ 4% hardness increase, but shows no discernible difference on low-X (ultra-fragile) samples

on annealing. When observing the hardness data over the composition range, a cusp in hardness is present at X = 18 for as-cast samples, but shifts to X = 20 once annealed. This shift on annealing and the accompanying HV annealing effect indicate X = 18 as an apparent transition point. Prior work on the same alloy system reported a distinct latent heat present at compositions with X < 18.[68] This marks this composition range as where the glass transition evolves toward a discontinuous melting transition.

X-ray diffraction reveals fully amorphous character in both as-cast and annealed samples across all compositions. In all cases, the glass appears to order during annealing resulting in a narrower and sharper primary amorphous band. This effect is more noticeable at high X with a 5 – 10% decrease, while low X samples see only a 3 – 4% decrease (FWHM). This smaller change combined with the hardness data suggest that, at low-X, the solid-like low-temperature glass phase is quenched in during casting and further orders on annealing. Where, for high X, the traditional glass phase is quenched, and annealing yields a more ordered glass phase.

Thermodynamically, both ultra-fragile X = 18 and 14 present the glass transition's characteristic rise in heat capacity, and the annealed samples display a recovery enthalpy. X = 14 shows an unusual additional endothermic peak above the glass transition that is interrupted by the rapid onset of crystallization. This is attributed to the onset of a melting transition of the solid-like phase. This interpretation is consistent with the results of Chapter 2, where a discontinuous configurational enthalpy jump (latent heat) is observed for X < 18. Further, an apparent solid-like phase melting front is captured with high-speed pyrometer video during rapid capacitive discharge heating measurements.[68] Through multiple methods and the results presented in Chapter 2, the case for a first-order glass-melting transition appears to be well established in the ultra-fragile metallic glass PtCuP system.

Chapter 4

EMBRITTLEMENT TRANSITION IN NI-BASED BULK METALLIC GLASS AS EVIDENCE OF THE G-PHASE GLASS

The author recommends the figures of this chapter be viewed electronically for assured visual clarity.

4.1 Abstract

$Ni_{80-X-Y}Cr_XNb_YP_{16.5}B_3$ alloys report an embrittlement transition that has historically been related to composition.[76] More recent works identified overheating as a mechanism to suppress the embrittlement transition in $Ni_{71.4}Cr_{5.64}Nb_{3.46}P_{16.5}B_3$ (Ni208). After a wide range of fragile-regime glasses in $Pt_{80-X}Cu_XP_{20}$ revealed a secondary glass phase and its glass-melting transition, the author explores Ni208 for the secondary glass phase in this stronger glass. This work connects the secondary glass phase to sample embrittlement in $m \sim 54$ Ni208 via secondary glass inclusions.

Cross sections of notch fracture toughness samples reveal inclusions present only in embrittled samples, suggesting the overheating treatments suppressed embrittlement by suppressing inclusion growth. Hardness reports a 25 - 28% increase from the matrix to inclusion, similar to previously reported hardness jumps from the primary to secondary glass.[65, 62, 66, 67] EDS in SEM and TEM revealed compositional equivalence between the matrix and inclusions. Structural analysis via TEM, SAED, and XRD reveal and explore a "cloudy" heterogeneous structure similar to what is seen in computational reports on the secondary glass, albeit at a larger scale.[62, 66, 67] SAED reveals the inclusion as a mixed ordered-disordered phase, but XRD clarify the inclusions as predominantly amorphous. This sheds light on how the secondary glass may present in stronger glasses while informing the long-lasting question on how overheating suppresses sample embrittlement — by suppressing inclusion growth. Further explorations are necessary into this sample system for the secondary glass, but these results provide a prominent foundation.

4.2 Introduction

The preceding chapters revealed a glass-melting transition in the full range of fragilities accessible to the $Pt_{80-X}Cu_XP_{20}$ glass family. Identified via configurational en-
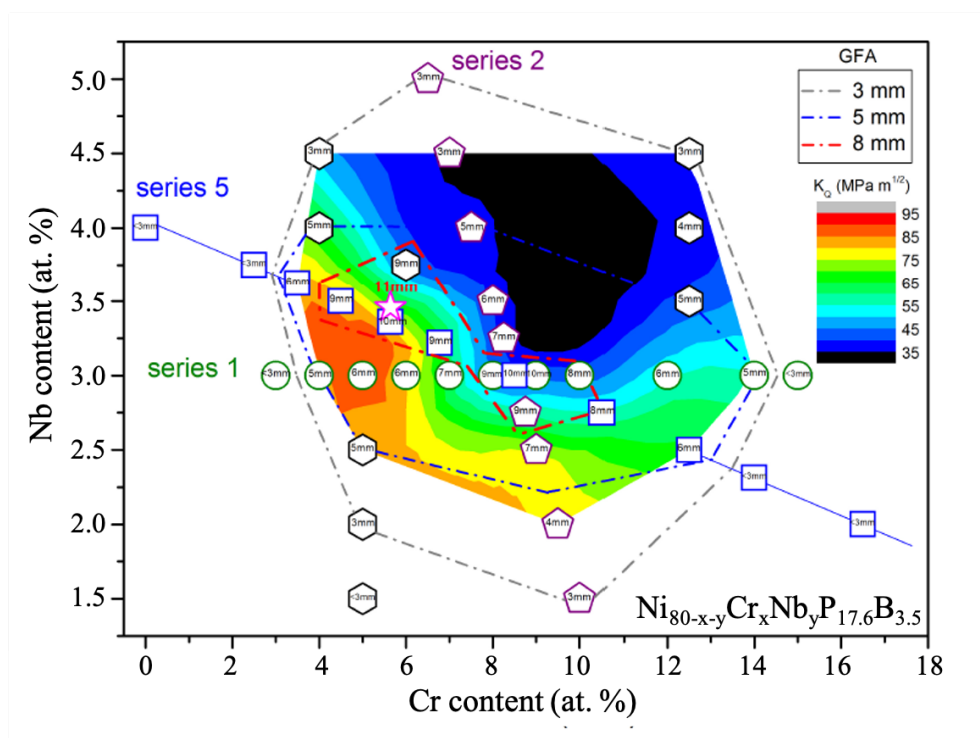
Figure 4.1: Superimposed dashed and color contours of GFA and Notch Fracture Toughness (K_Q), respectively, on the Ni alloy composition landscape. Figure D.1 in Appendix D visualizes a color contour for GFA for additional clarity. Please see the electronic version for assured visual clarity.

thalpy and traditional heating scans, fragilities of $m = 60$ to over 90 were explored. While informative of the elusive fragile regime, the author now investigates whether this second phase is present in stronger glasses and how it presents.

In determining a strong glass worth study, an odd phenomenon in a Ni-based BMG system piqued the author's interest. $Ni_{80-X-Y}Cr_XNb_YP_{16.5}B_3$ exhibits an embrittlement transition with m ranging from 54 to 77. Numerous studies have explored potential underlying factors to this embrittlement, but this author hypothesizes the presence of the secondary glass and its increased hardness could play a critical role. This introduction will briefly summarize the current understanding of the embrittlement transition in the $Ni_{80-X-Y}Cr_XNb_YP_{16.5}B_3$ glass family and will serve as context behind this work's search for the secondary glass in $Ni_{71.4}Cr_{5.64}Nb_{3.46}P_{16.5}B_3$ (Ni208).

Multiple studies investigated the underlying factors behind the embrittlement transition. First, a composition map along the $Ni_{80-X-Y}Cr_XNb_YP_{16.5}B_3$ landscape was probed for notch fracture toughness (K_Q) and glass forming ability (GFA). Figure
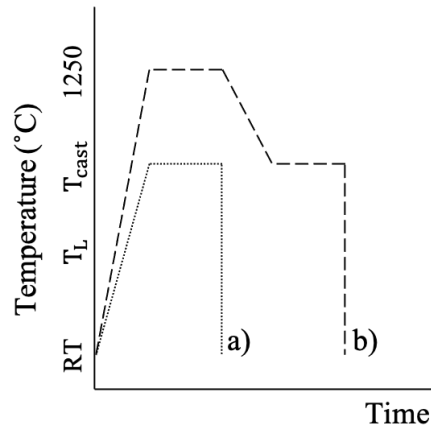
Figure 4.2: Visual representation of the two casting methods. Direct casting from casting temperature T_{cast} (a), versus overheating to the toughening temperature T_{tough} before cooling to and quenching from the casting temperature T_{cast} (b).

4.1 summarizes these findings with a color contour for K_Q and a dashed contour for GFA. These properties display overlapping maxima and minima across the composition landscape. A steep drop off is observed, where traversing the compositional landscape reduces both GFA and K_Q, switching the sample from tough and ductile to brittle. This sudden change in properties makes this a composition region of interest. In the desire to probe stronger glasses for the second glass phase, the strongest glass in the NiCrNbPB system, Ni208, is a worthy pursuit. In addition to its fragility of $m \sim 54$, its location in the GFA vs. K_Q vs. composition landscape is promising for transitionary properties. Ni208 is marked by the star in Figure 4.1 near peaks in both GFA and K_Q. Further, this composition is uniquely placed near the transition between high and low GFA and K_Q, such that small variances lead to large property changes. So while this first work correlated embrittlement to GFA and composition, a second study explored a more direct link to embrittlement in Ni208.

A patent by Na *et al.* with Glassimetal Technologies compared thermal treatments to probe the embrittlement transition in Ni208.[10] The samples were subjected to two thermal treatments: direct casting and overheating before casting. In both cases, the casting temperature, T_{cast}, describes the temperature of the sample just before quenching to room temperature. The two pathways are visualized in Figure 4.2. Path (a) indicates the direct casting method. The sample is heated above the liquidus to T_{cast}. Path (b) heats the sample above the liquidus and casting temperature to an overheating temperature of 1250°C and held to attain equilibrium.
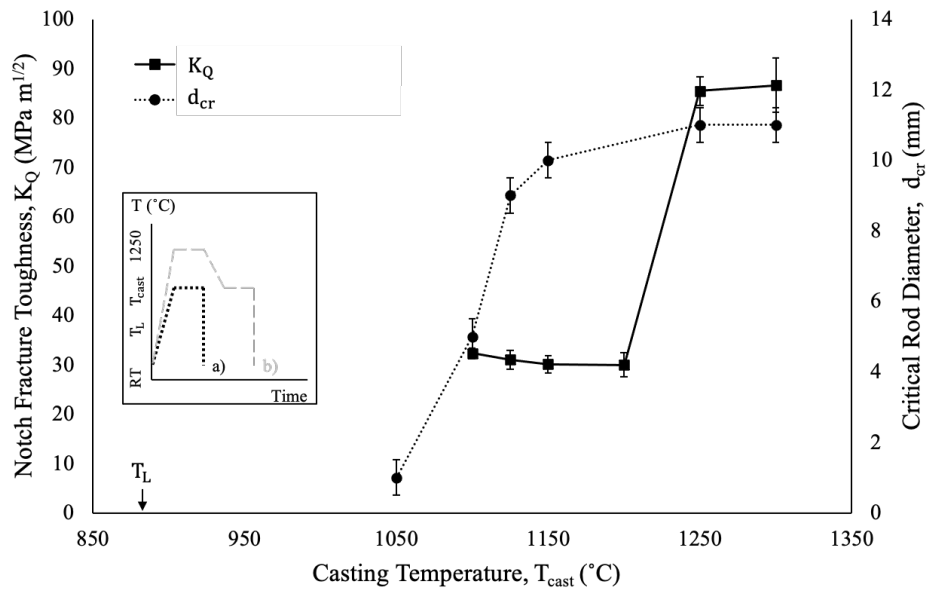
Figure 4.3: Notch fracture toughness K_Q and critical rod diameter d_{cr} under the direct casting method.[10]
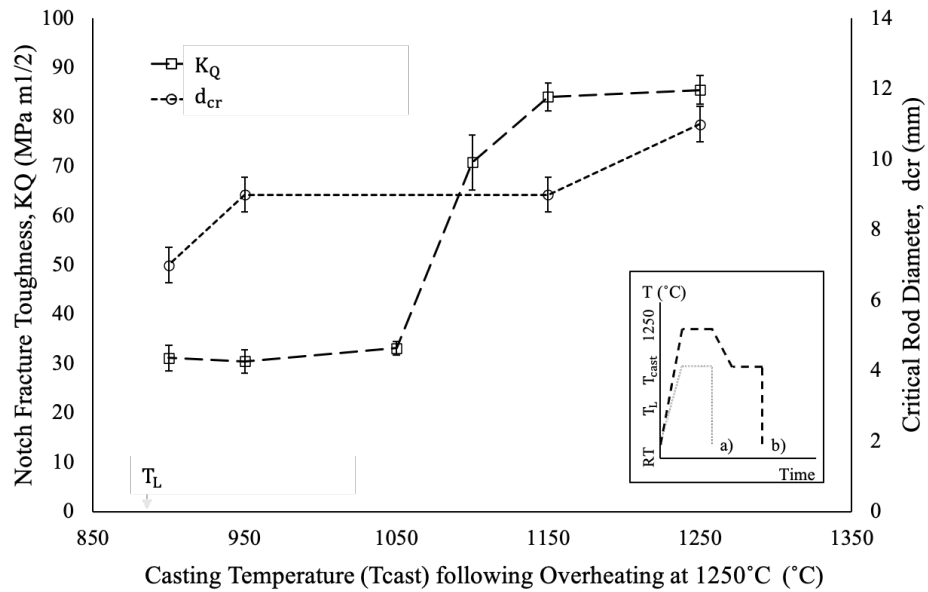

Figure 4.4: Notch fracture toughness K_Q and critical rod diameter d_{cr} under the overheating casting method.[10]

Post equilibration, the sample is cooled slightly to the casting temperature before quenching. Throughout the text, these methods are referred to as "cast T" or "direct-cast," and "overheating," respectively.

K_Q and critical rod diameter d_{cr} (mm) were measured on as-cast samples for each casting condition. Figures 4.3 and 4.4 summarize these data. The respective thermal treatment pathway is bolded in the inset. All samples are 3-mm diameter rods as required for the ASTM standard for notch fracture toughness. When focusing on the direct casting method, Figure 4.3 reveals a 65% drop in K_Q from 1250 to 1200°C, and a 55% decrease in d_{cr} from 11 to 5mm across 1250 to 1100°C. These data describe 1250°C as a critical toughening temperature, T_{tough}. When $T_{cast} > T_{tough}$ the sample exhibits tough behavior. The overheat method for Figure 4.4 utilizes T_{tough} as an overheating temperature. This determined if overheating above T_{tough} would have an effect on K_Q and d_{cr}. While the overheated samples saw similar 63% and 36% drops in K_Q and d_{cr}, they occurred at lower temperatures of 1050 and 900°C, respectively. The GFA minimum from overheated samples only fell to 7mm, maintaining a higher GFA across all casting temperatures compared to the direct-cast samples.

The thermal treatment effect on K_Q is visualized by direct comparison of Figures 4.3 and 4.4. The overheated samples in Figure 4.3 display embrittlement suppressed to lower temperatures. This shifts the embrittlement transition by 150°C from 1200 (Figure 4.3) to 1050°C (Figure 4.4). As for the underlying cause, it is important to note that in both cases, this embrittlement is not related to crystal formation; d_{cr} remains well above the 3-mm sample diameter for all K_Q. In search of the embrittlement cause, the work of this chapter probes cross sections of the exact K_Q samples from Figure 4.3 and 4.4 for evidence of a second glass phase. With previous chapters indicating heat treatments (as-cast versus anneal) yielding different properties related to the secondary glass, the Ni208 casting condition-related embrittlement is a promising space to investigate the possible secondary glass phase.

4.3 Methods

Sample Preparation and Ni208 Caveat

The samples utilized in this work are the exact samples tested in Figure 4.3. Cross sections were taken off the non-fractured ends of the rods to avoid potential phase separation resultant from the fracture energy. Samples were cleaned before subsequent steps. Sample cleaning procedure included 10 minute sonication baths each

of acetone and ethanol with three rinses with the respective solvent before each soni-cation. Once cleaned, all samples were embedded in epoxy pucks such that the puck height is < 9mm to fit in the XRD sample holder. The pucks were ground at 400 grit until flat. Polishing stopped when inclusions were visible at 1200-grit. Grinding and polishing were completed with a Buehler autopolisher (ecomet 3 variable speed grinder-polisher equipped with an automet 2 power head). Samples were stood on end for a 3-mm diameter exposed polished surface. Once polished, the surface was wiped with isopropyl alcohol on a kim wipe to assure no debris was present.

Sample Caveat: Properties of $Ni_{71.4}Cr_{5.64}Nb_{3.46}P_{16.5}B_3$ (Ni208) are assumed sim-ilar enough to the those of $Ni_{70.4}Cr_{5.64}Nb_{4.46}P_{16.5}B_3$ (Ni210) given their almost equivalent compositions. T_g, T_m, and m were not measured directly for Ni208 due to defunct equipment by the time of sample study. Ni210 properties are summarized in Table D.1.[8]

Vicker's Hardness and Optical Imaging

Hardness indentations were completed in a LECO LV810AT Oprical Scope and Hardness Tester using 4.903N force and a 5s dwell time. Indentations averaged around 50-μm across. Indentations were completed in the epoxy puck to assure a level surface for accurate indentations. General surface images were captured at 10x magnification. The topography contrast is most-visible, if not *only* visible, at 10x magnification.

Inclusion Area Percent Calculation

Two methods were employed for establishing the analysis surface. For T_{cast} = 1100, 1125, and 1150°C, the respective images in Figure 4.5 capture areas representative of each sample's overall inclusion prevalence. These images were then used to calculate a representative percent. For samples where inclusions were more sparse (T_{cast} = 950 and 1200°C), optical images were taken in a raster pattern across the full sample surface and compiled into a mosaic in Adobe Photoshop. The full image of the 3-mm cross-section surface was calculated over. With the analysis surface established, a stark contrast was achieved between the inclusion and matrix areas. ImageJ was then utilized to count the respective dark (inclusions) and light (matrix) areas, and a percent over the full analysis area was calculated.

Scanning Electron Microscopy and Energy-Dispersive X-ray Spectroscopy

Samples were examined on a ZEISS 1550VP field-emission scanning electron microscope (SEM, Carl Zeiss Microscopy GmbH, Jena, Germany) equipped with an Oxford X-Max Si-drift-detector energy dispersive X-ray spectrometer (EDS) system. SmartSEM and AZtec software packages were used for imaging, mapping, and EDS analysis. Analysis used a 5-kV accelerating potential, operating at a magnification of 10kx. Given the inclusions are not discernible in SEM, indentations were used to assure SEM imagaing and EDS analysis were completed in the correct locations. Due to Covid-19 restrictions, SEM was conducted by Celia Chari, and nano-indentations for inclusion mapping were conducted by Seola Lee.

High-Resolution Transmission Electron Microscopy for Energy-Dispersive X-Ray Spectroscopy and Selected Area Electron Diffraction

Samples were marked by arrays of nanoindentations, imaged optically at 10x, and maps were composed to assure TEM samples were cut at the correct location (matrix-inclusion interface). The lamellae were prepared using the ex-situ FIB lift-out technique on an FEI Dual Beam FIB/SEM. The samples were capped e-CPt/I-C prior to milling. The TEM lamella thickness was <100-nm. The samples were then imaged with a FEI Tecnai Osiris FEG/TEM operated at 200kV in bright-field (BF) TEM mode followed by composition analysis via energy dispersive X-ray spectroscopy (EDS) and selected area electron diffraction (SAED). Due to COVID-19 constraints, samples were sent out to EAG Laboratories for TEM analysis and its sample preparations.

X-Ray Diffraction (XRD) and Crystallinity Calculation

XRD analysis was completed with 1 hour scans on a Panalytical X'Pert Pro. Given the samples are cast in carbon-based epoxy pucks, once mounted with putty, the puck was masked-off with corning glass cover slips (thickness 2 18x18, cat no. 2855-18) to remove the carbon peaks at 26, 42-45, 50 and 54 °(2θ). To assure all puck peaks were removed, a 3-mm hole was drilled through a cover slip and aligned with the sample. A figure of this layout is included in Appendix Figure C.1.

The crystallinity percentages were calculated from relative peak area over total area under the XRD scan between 35 and 55 °(2θ). The calculation baseline was established as the minima of each scan.
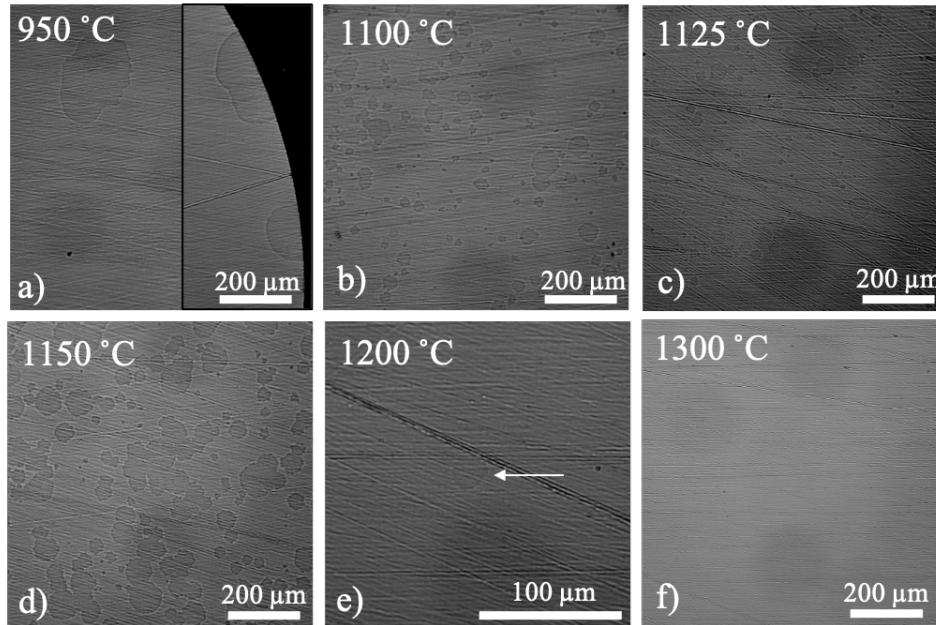
Figure 4.5: Visualized inclusions on 1200-grit polished cross-sections of direct-cast samples. Please see the electronic version for assured visual clarity. Inclusion area percentages for a-f: 4.05, 11.90, 5.74, 34.87, 0.12, and 0.00%, respectively. Note: there are three artifactual repeated smudges in each image.

4.4 Results and Analysis

Cross sections were prepared from the exact direct-cast samples from Figure 4.3. Post-polish, inclusions were visible of varying size and prevalence across each sample surface. These inclusions are visualized in Figure 4.5a-f, ordered by increasing casting temperature. Inclusions are only present in brittle samples, with no inclusions visible in the tough samples. Relative coverage areas were calculated across each sample surface. Inclusion area percentages report 4.05, 11.90, 5.74, 34.87, and 0.12% for 950, 1100, 1125, 1150, and 1200°C, respectively. The 1300°C sample has no visible inclusions given the limits of the visualization method; i.e., inclusions are discernible down to $\sim 5\text{-}\mu m$. Thus 0.00% inclusion area is reported within this limitation. The overheated samples of Figure 4.4 also only saw inclusions in the brittle samples, but these samples are not further included in this discussion. In addition to d_{cr} sustaining well above the sample size, these inclusions are anticipated to be amorphous due to the inclusion shape. The inclusion-matrix interface is distinctly rounded and not angular or dendritic, like would be observed for crystal growth. The inclusions appear to grow radially and merge together, best highlighted in Figure 4.5d. It is believed these inclusions could be related to the second glass
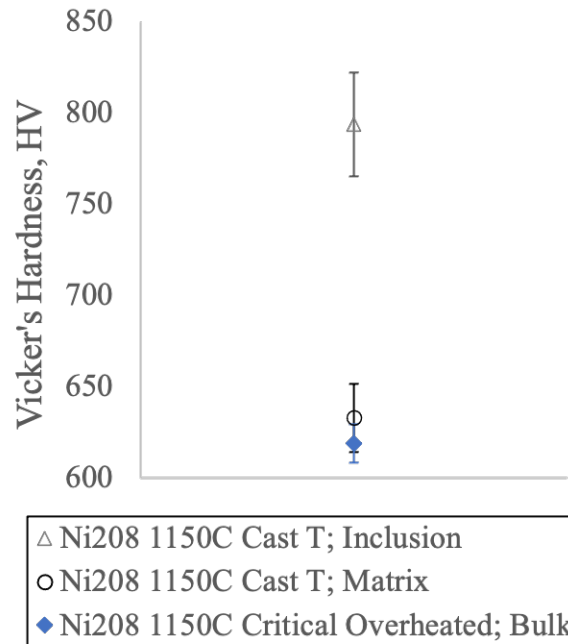
Figure 4.6: Vickers hardness micro indentations ($\sim 50\mu m$) across the heat treatment-induced surfaces of $T_{cast} = 1150°C$ Ni208.

phase, as they require the same unique lighting conditions as the peculiar surface topography in the long-annealed $Pt_{62}Cu_{18}P_{20}$ sample in Figure 3.7. This marks these inclusions as worth further exploration — starting with comparison to known properties of the second glass phase.

The most established property difference between the two glass phases is hardness. Previous works report a $20 - 30\%$ increase in hardness from the primary to a secondary glass. For the present work, micro-scale Vicker's Hardness diamonds were indented into three sample types/locations: the inclusion, matrix, and bulk. The inclusion region is indeed the notable inclusions visualized in Figure 4.5. The "matrix" refers to the sample surface outside of the inclusion area in brittle samples, and the "bulk" refers to the tough samples were there are no visible inclusions. The matrix and bulk are probed to determine if the matrix is a different glass than the bulk. In choosing a sample, the inclusion and matrix regions must be of sufficient size to support multiple 50 micron indentations in each, as well as a bulk sample. The mid-range 1150°C samples achieve all criteria when both aforementioned casting methods are utilized. The direct-cast method has sufficiently-sized inclusions in the matrix (Figure 4.5d), and the overheated sample has no inclusions and exists with only the "bulk." The data are plotted in Figure 4.6 where the matrix and

bulk samples report averages of 632.99 and 619.16 HV, respectively, but overlap within error. However, the inclusions report an average of 793.38 HV; a 25.34 and 28.14% increase from the matrix and bulk, respectively. These data suggest the matrix and bulk are equivalent glasses, and that the inclusions grow within the bulk glass. Further, these inclusions show strong similarities with the reported character difference between the two glass phases, showing promising early evidence of the inclusions as a second glass phase.

Next, composition analysis on the matrix and inclusion was completed with an Energy Dispersive X-ray Spectroscopy (EDS)-equipped Scanning Electron Microscope (SEM). With the inclusions not visible in SEM (see Figure D.4a), indentations were utilized to validate the analysis location in the sample. Figure 4.7 depicts the matrix and inclusion composition maps across the NiCrNbPB composition with inset percent prevalence (by eV counts). The central bright/dark spot is the indentation and any color variance is assumed erroneous. The composition variance between the matrix and inclusion is negligible at this resolution, varying a maximum of 0.28% in Cr. Thus the Ni208 matrix and inclusions are compositionally equivalent, as described across the other secondary glass works.[62]

Given the computational work of An *et al.* observed a structural difference between the two glasses (L and G), with the secondary glass as a heterogeneous form, high-resolution transmission electron microscopy (TEM) was utilized for improved visualization, composition analysis, and diffraction of the Ni208 matrix-inclusion interface. Figure 4.8 summarizes these results. Since inclusions are only visible under optical microscopy and not discernible in SEM, the inclusion-matrix interface locations were mapped against nano-indentation arrays to assure locations were probed accurately (see Figure D.4).

The high-resolution TEM image in Figure 4.8a visualizes the matrix-inclusion interface, with the matrix on the top left and the inclusion on the bottom right. The interface runs across the image from the bottom left to the top right. The inclusion presents as a "cloudy" region with varied contrast. The darker regions between the "clouds" appear equivalent to the matrix, and the "clouds" present brighter. With the interface not angular as would be expected in traditional crystals, a connection is drawn to the heterogeneous G phase of An *et al.*[62, 66, 67] Composition was then probed across various regimes to add a higher-resolution analysis than that provided by SEM. EDS was completed on the areas marked i-iv on Figure 4.8a and are reported graphically in Figure 4.8b. While the averages vary slightly between
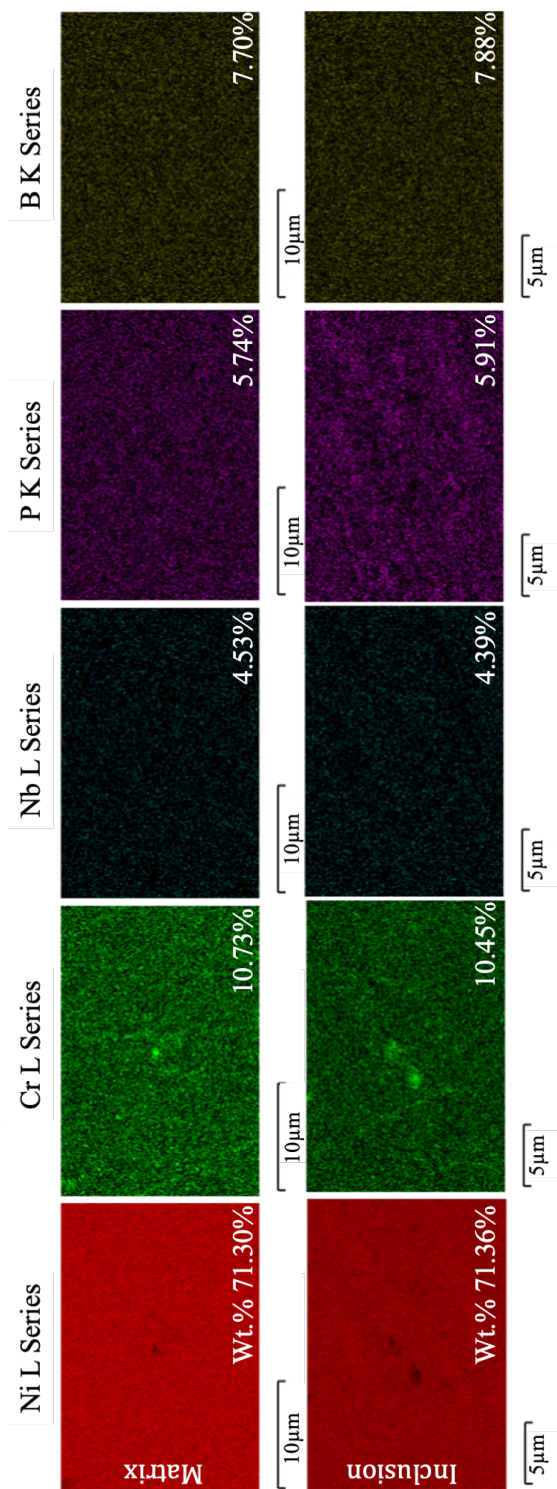
Figure 4.7: SEM EDS across the matrix and inclusion. The bright central dot is artifactual at the indentation location. Displayed sideways for sufficient resolution. Please see the electronic version for assured visual clarity.
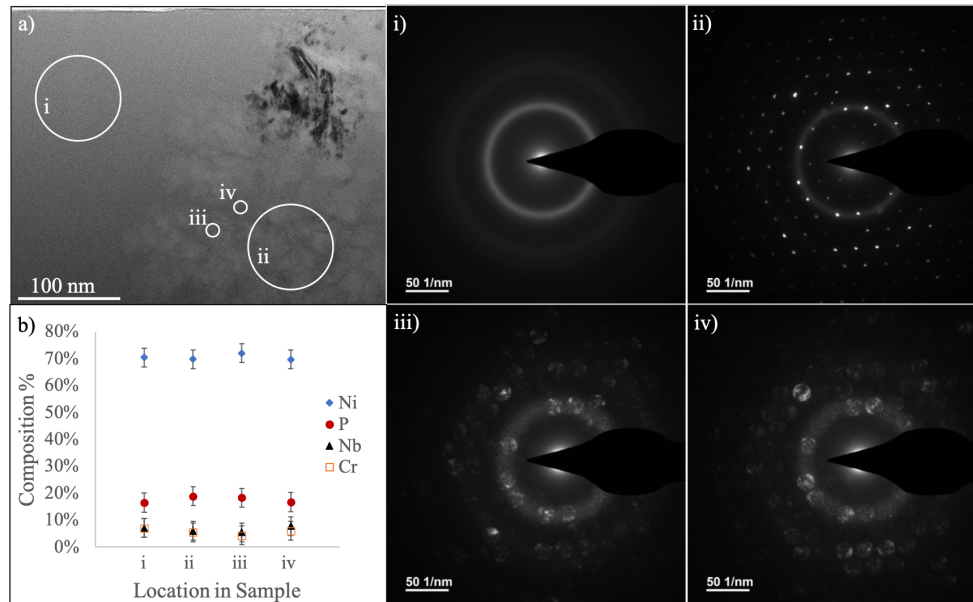
Figure 4.8: Bright-field TEM image of the matrix-inclusion interface (a) with labeled locations (i - iv) for diffraction patterns. EDS completed on locations (i-iv) reported the composition % calculated via eV counts in b. Please see the electronic version for assured visual clarity.

sections, all variance is within error. Thus the compositions are equivalent, and TEM provides additional high-resolution verification of computational equivalence as seen in the An *et al.* G-phase. However, the selected area electron diffraction (SAED) patterns in Figure 4.8i-iv — labeled with respect to the SAED location — reveal an interesting structural story. The matrix acts as expected, revealing amorphous bands in i. However, the remaining locations in the general inclusion (ii), as well as specifically in a "cloud" (iii) and between "clouds" (iv), reveal mixed order and disorder. While the ordered regions of An *et al.*'s G-phase report curved planes in fcc/hcp or icosahedral environments, it is not clearly discernible that this is the cause of the diffraction patterns of ii-iv.[62, 66, 67] There is some concern about whether the samples were altered by the energy of the focused ion beam (FIB) used to prepare the TEM cross sections. With the hypothesis that this secondary phase more readily crystallizes, this could potentially be a snapshot as it moves toward crystallization.

To better understand if the sample preparation for TEM altered the samples, X-ray Diffraction via a Panalytical X'Pert Pro was conducted on all cross sections of the direct-cast samples (from Figure 4.5). These samples experienced the same sample preparation as the optical imaging and HV indentation samples. Figure 4.9 visualizes
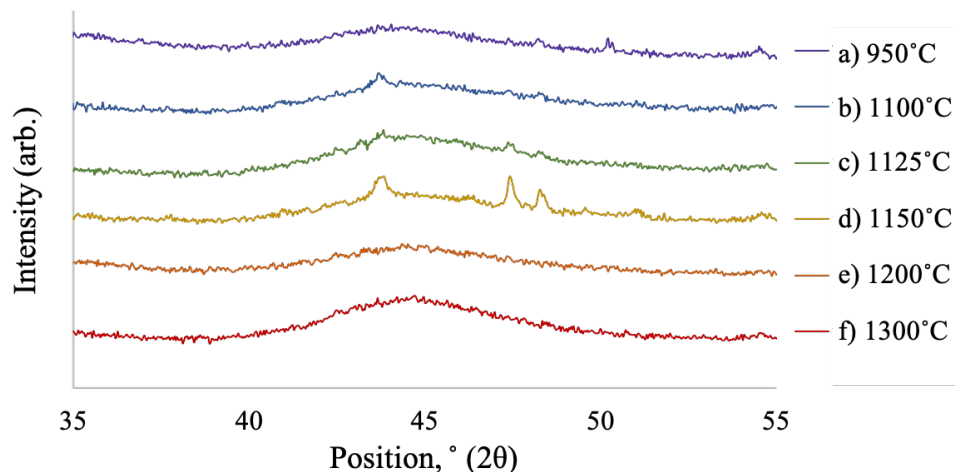
Figure 4.9: XRD for samples cast utilizing the direct casting method. Labels are adjacent to their respective scans and labels a-f correlate to the labeled cast temperature surfaces in Figure 4.5.

the hour-long XRD scans from $35 < 2\theta < 55$. This region was chosen to focus on the amorphous band. No peaks appear in the tough 1300°C scan (f), nor in two of the five brittle scans (950 and 1200°C for a and e, respectively). However, three minor peaks arise at 44, 46.5, and 48 ° (2θ) in the brittle 1100, 1125, and 1150°C samples (Figure 4.9b-d). These peaks are relatively minor, however, such that a dominant amorphous band remains clearly visible for all samples. This raises a question on whether the diffraction peaks arise from the inclusions, and if the inclusions are partially or entirely crystalline. The degree of crystallinity, or crystallinity percent, was calculated from the scans to compare with the aforementioned inclusion area percentages. Taken as the percentage of area under the peaks relative to that under the overall amorphous band, these data are reported along side K_Q and inclusion area percent in Figure 4.10. The crystallinity percentages are 0.00, 2.74, 2.74, 6.41, 0.00, and 0.00% for T_{cast} = 950, 1100, 1125, 1150, 1200, and 1300°C direct cast samples, respectively. When compared to the inclusion area, while the crystallinity does increase with inclusion percent, the crystallinity is distinctly lower in all cases. This informs that the inclusions are not fully crystalline, but do have some relationship to crystallization. However, further analysis is required to determine the type of crystalline ordering, to what extent, and how it may relate to a possible heterogeneous G-phase glass.

Importantly, the relation of inclusion area percent to K_Q is worth note. When even
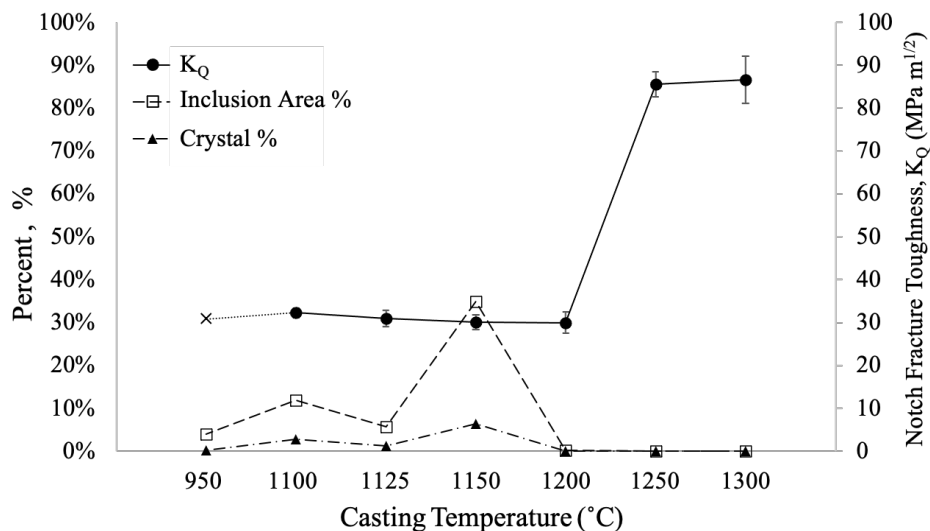
Figure 4.10: Hardness across inclusion, matrix, and bulk samples for $T_{cast} = 1150°C$.

a small 0.12% of inclusions are present (but 0.00% diffraction peaks), the Ni208 system embrittles. This brittle behavior persists for all samples hosting inclusions. So, as the inclusions are further investigated for their structure, it is clear they play a key role in the embrittlement transition. The author hypothesizes the inclusions have harder, lower toughness regions that lead to lower global toughness values. Discussions and analysis on critical defect size have been implemented, but are limited due to the lack of K_C data. Assumptions were possible, but were too extensive to justify defense of the conclusions. However, while the detailed origins of global embrittlement have been explored here, no clear conclusions have been drawn, leaving open questions for future works.

While there is promising HV and composition data, the microscopic structure of the inclusions needs greater understanding. While the inclusions are apparently at least partially amorphous, they also appear to contain nanocrystals as well. It is not clear, for example, whether the inclusion is initially fully amorphous on formation then subsequently partially crystallizes during its growth, if partial crystallization occurs at the outset of inclusion formation, or whether TEM sample preparation altered the inclusion structure. These efforts provide a promising starting point for future investigations on formation of the second glass phase in strong metallic glass systems, like the present Ni-based alloys.

4.5 Summary and Conclusions

Previous works report an embrittlement transition in the $Ni_{80-X-Y}Cr_XNb_YP_{16.5}B_3$ BMG system. The most recent study ties this embrittlement to the pre-casting thermal history of the metallic glass samples, specifically in the $Ni_{71.4}Cr_{5.64}Nb_{3.46}P_{16.5}B_3$ alloy (Ni208). When overheating above a critical toughening temperature, T_{tough}, during processing, embrittlement is suppressed even at lower subsequent casting temperatures. Based on the observations in this chapter, the author hypothesizes this embrittlement is due to the presence of harder secondary glass phase inclusions, and that the presence or absence of the inclusions is related to the liquid thermal history prior to casting of the glassy sample.

This work explored the cross sections of the Ni208 study samples. Inclusions are found present only in the brittle samples, and are believed to be a secondary glass phase. Visible in green-light optical imaging at 10x magnification, these inclusions vary in size, prevalence, and location across the reported casting temperatures. Inclusions display a 25 - 28% hardness increase from the surrounding glassy matrix, similar to that reported for multiple secondary glasses.[65, 62, 66, 67] The matrix around the inclusions and the bulk (when no inclusions are present) report equivalent hardness, which suggests they are the same glassy phase. Thus, it is assumed the inclusions form and grow from the undercooled liquid during the casting and quenching process.

The structure and composition were explored via SEM with EDS, TEM with EDS and SAED, and XRD. SEM EDS reports compositional equivalence between the inclusion and matrix, where analysis was focused on one region at a time. High-resolution TEM on the interface revealed a "cloud-like" structure reminiscent of the G-phase in Qi*et al.*'s work on pure Ag, albeit at a significantly larger scale (tens or hundreds of nanometers). Composition analysis via EDS across numerous regions reports equivalent averages within error. SAED revealed the expected amorphous behavior in the matrix, but a mixed amorphous-partially crystallized behavior in the inclusion. The curved planes in fcc/hcp- and icosahedral- like stacking in the Ag and AgCu versus CuZr compositions reported by An *et al.* could be the cause of these mixed results, but the nanocrystals observed in the Ni-alloy are at a significantly larger length scale than the heterogeneities reported in the MD work. In fact, there is possible concern that the FIB lift-out technique for the TEM lamellae sample preparation may have altered the secondary glass phase and induced nanocrystal formation. To address this concern, XRD was completed on the polished 3-mm

sample cross sections. XRD scans reported three relatively minor diffraction peaks in three of the investigated brittle samples. Assessing the crystallinity using area percentages based on X-ray, the crystalline regions are believed to be at most a small portion of the overall inclusions. Thus, the inclusions are primarily amorphous. Further, when only 0.12% inclusions (and 0.00% crystallinity) were present, the sample embrittles by a 65% reduction in apparent fracture toughness. This verifies the effect of inclusion presence on embrittlement, and that overheating samples prior to casting suppresses embrittlement by suppressing inclusion formation and growth. While further study is required to verify if these inclusions as initially formed are in fact a fully amorphous secondary glass for this Ni-BMG system, the present work provides a promising starting point from which to continue the study.

C h a p t e r   5

CONCLUDING REMARKS

5.1   Conclusions

The three final chapters presented in the thesis draw direct links to the second glass phase described in Chapter 1, Section 1.4. The combined works establish experimental evidence for two distinct glassy phases across the spectrum of strong to high- and ultra-high fragility metallic glass forming liquids.

Given that the secondary glass was first identified computationally in ultra-high fragility Ag and binary AgCu and CuZr, experiments initially pursued the same high fragility regime. Configurational thermodynamics on the $Pt_{80-X}Cu_XP_{20}$ system (Chapter 2) employs accurate direct measurements of the anneal-equilibrated liquid configurational enthalpy as a function of temperature. This reveals an apparent first-order glass-melting transition with discontinuous enthalpy and entropy changes at the phase boundary, T_{gm}. The glass-melting transition is discernible across X = 14 - 27, except for those compositions where T_{gm} is in the inaccessible ΔT region (X = 20, 23). However, apparent melting is observed in X = 20 when the heating rate is sufficiently high (via rapid capacitive discharge heating imaged via ultra-fast pyrometer tracking and infra-red video as in Figure 3.6). Further, the utilization of a new DOS approach to describe configurational entropy and accurate data accumulation methods present a configurational entropy that vanishes in the low-temperature limit, averting the Kauzmann paradox.

With the configurational thermodynamics approach employed in Chapter 2 revealing the second glass phase behavior in annealed samples, mechanical, structure, and thermodynamic approaches were utilized to reveal distinct physical characteristics between the primary and secondary glasses (Chapter 3). The thermal treatments to achieve each phase were proposed as follows: as-cast samples produce the primary glass phase, whereas anneals achieve the secondary glass phase. However, HV data suggest that the secondary glass phase grows on annealing in highly fragile glasses, but is actually achieved on quenching for the ultra-fragile glasses. Structural data via XRD report similar findings, where FWHM of the amorphous band describes increased atomic ordering across all samples on going from as-cast to annealed, but to different extents. The high-fragility samples show a markedly greater ordering

effect compared to the ultra-fragile samples, further suggesting the secondary glass phase grows on annealing in the former samples, but is already present in the latter. Heating the sample at 20 K/min from room temperature through the melt verified that this melting transition is also visible using classical thermodynamic methods. The ultra-fragile annealed X = 14 sample shows an onset melting transition after T_g that is interrupted by crystallization. This T_{gm} is equivalent, within error, to that found for X = 14 in Chapter 2. These two studies on the high-fragility to ultra-fragile PtCuP alloys provide a promising multi-faceted foundation for the experimental observation of two distinct glass phases.

Finally, the Ni208 study on a hypothesized second glass phase-induced embrittlement transition extends the discussion to the kinetically strong glass forming liquid regime (Chapter 4). The work identifies roughly spherical, heterogeneously structured inclusions only present in brittle samples. These inclusions are ~30% harder than the glassy matrix phase, similar to the hardness jump reported between the computational L and G glasses.[62, 66, 67] The inclusions are connected to results of work presented in a prior patent that show that overheating the melt prior to casting a glassy sample suppresses the embrittlement transition. This work reveals that overheating apparently suppresses embrittlement by suppressing the formation and growth of inclusions. The heterogeneous inclusions are predominantly amorphous but also show formation of nanocrystals within the inclusion. It is unclear if the inclusions are entirely glassy upon initial formation and later partially crystallize, or contain some amount of crystallinity from the outset of formation. As such, it remains unclear if the inclusions can be identified with the G-phase observed in the MD simulation work of An *et al*.[62]

The thesis presents direct experimental evidence of a novel glass-melting transition, and presents a new solid-like glass phase. The evidence of the second glass phase extends from strong to ultra-fragile glasses, and validates the initial computational discovery. Paired with further computational and experimental studies, the second glass phase is further predicted across traditional glass systems.

5.2 Summary of Outcomes

These results were achieved following the motivations outlined in Section 1.5 (indicated by the numbers in parentheses). The PtCuP system of Chapters 2 and 3 provided a high-fragility and ultra-fragile glass system for the previously unexplored regime (1). A direct calorimetry study of configurational thermodynamics

was applied with a well-equilibrated glassy state (2), a new analytic expression to better represent the configurational enthalpy data was introduced (3), and an apparent glass-melting transition was revealed through improved accuracy of calorimetric data. This melting transition occurs across a range of fragilities and shows an apparent glass-melting temperature T_{gm} spanning the ΔT undercooled liquid region. This demonstrates that the inaccessible SCL regime requires further probing by RDH or FDSC. These motivations yielded both the glass-melting transition and a resolution to the Kauzmann paradox at ultra-high fragility. For stronger glasses, the embrittlement transition is connected to the secondary glass via grown inclusions in Chapter 4 (Figure 4.5). While these motivations proved very fruitful for this work, there remain further questions to address.

5.3   Future Work

The combined works of this thesis provide experimental evidence and support for the secondary glass phase. Specific details of An *et al.* and Shen *et al.* were emphasized and verified in these studies (i.e., hardness, latent heat and melting transition, heterogeneous structure, and composition equivalence). But in addition to these addressed and verified G-phase characteristics, An *et al.* also investigated the L-G transition through the lens of rigidity. They demonstrate that the L-G transition corresponds to the emergence of elastic rigidity from determining the shear modulus and the persistence of stress fields of each phase.[77] With an onset of rigidity from the L to G phase, the melting transition (G to L) is described as a loss of elastic rigidity. This is related to rigidity catastrophe described by the Born melting criterion as discussed in Section 1.4.

A future study is proposed to probe the rigidity loss on G-phase melting. The shear modulus can be measured with respect to temperature using ultrasonic methods and *in-situ* transducers. Following the methods utilized by Mary-Laura Lind in her 2008 Ph.D. dissertation, the shear modulus can be mapped versus temperature and time. With increasing temperature on as-cast and annealed samples, the decay of the shear modulus can be investigated. Further, observation of the evolution of the heterogeneous G-phase structure over temperature in high-resolution TEM, or using high-speed synchrotron X-ray methods would likewise shed valuable light on the structure and structural transformation that accompanies the G-glass-melting transition.

Additional pursuits could include a study on what underlies G-phase inclusion

formation and growth in strong metallic glasses. The images in Figure 4.5 visualize inclusion size, prevalence, and location. Inclusions predominantly present internal to the sample, but lie on the sample perimeter or container wall for others. In particular, the low cast temperature 950°C sample has most inclusions on the cross-section perimeter, with only a few internal. This suggests that the rigid container wall might be a preferred site for inclusion nucleation. This could be related to elastic rigidity. The rigid quartz wall present during quenching could serve as a rigidity-template for the the G phase per An *et al*.'s work. Internally nucleated inclusions might relate to slower cooling of the melt where the secondary glass forms just before the crystallization nose as per Shen *et al*.'s metallic glacial glass.

BIBLIOGRAPHY

[1] C. A. Angell. "Formation of Glasses from Liquids and Biopolymers". In: *Science* 267.5206 (Mar. 31, 1995), pp. 1924–1935. ISSN: 0036-8075, 1095-9203. DOI: 10.1126/science.267.5206.1924. URL: http://www.sciencemag.org/cgi/doi/10.1126/science.267.5206.1924 (visited on 09/25/2019).

[2] W. Klement, R. H. Willens, and Pol Duwez. "Non-crystalline Structure in Solidified Gold–Silicon Alloys". In: *Nature* 187.4740 (Sept. 1960), pp. 869–870. ISSN: 0028-0836, 1476-4687. DOI: 10.1038/187869b0. URL: http://www.nature.com/articles/187869b0 (visited on 09/25/2019).

[3] B. Fultz and James M. Howe. *Transmission electron microscopy and diffractometry of materials*. 4th ed. Graduate texts in physics. OCLC: ocn796932144. Heidelberg ; New York: Springer, 2013. 761 pp. ISBN: 978-3-642-29761-8.

[4] S. Bhattacharya. "Chapter 8 - Electrical Transport Properties of Ion-Conducting Glass Nanocomposites". In: *Glass Nanocomposites*. Ed. by Basudeb Karmakar, Klaus Rademann, and Andrey L. Stepanov. Boston: William Andrew Publishing, Jan. 1, 2016, pp. 181–214. ISBN: 978-0-323-39309-6. DOI: 10.1016/B978-0-323-39309-6.00008-0. URL: https://www.sciencedirect.com/science/article/pii/B9780323393096000080 (visited on 01/07/2022).

[5] Mark Telford. "The case for bulk metallic glass". In: *Materials Today* 7.3 (Mar. 1, 2004), pp. 36–43. ISSN: 1369-7021. DOI: 10.1016/S1369-7021(04)00124-5. URL: http://www.sciencedirect.com/science/article/pii/S1369702104001245 (visited on 11/07/2019).

[6] Yanbo Wang et al. "Corrosion performances of a Nickel-free Fe-based bulk metallic glass in simulated body fluids". In: *Electrochemistry Communications* 11 (Nov. 1, 2009), pp. 2187–2190. DOI: 10.1016/j.elecom.2009.09.027.

[7] Mehdi Jafary-Zadeh et al. "A Critical Review on Metallic Glasses as Structural Materials for Cardiovascular Stent Applications". In: *Journal of Functional Biomaterials* 9.1 (Feb. 27, 2018), E19. ISSN: 2079-4983. DOI: 10.3390/jfb9010019.

[8] W. L. Johnson, J. H. Na, and M. D. Demetriou. "Quantifying the origin of metallic glass formation". In: *Nature Communications* 7.1 (Apr. 2016), p. 10313. ISSN: 2041-1723. DOI: 10.1038/ncomms10313. URL: http://www.nature.com/articles/ncomms10313 (visited on 10/04/2019).

[9] Pol Duwez, R. H. Willens, and R. C. Crewdson. "Amorphous Phase in Palladium—Silicon Alloys". In: *Journal of Applied Physics* 36.7 (July 1965), pp. 2267–2269. ISSN: 0021-8979, 1089-7550. DOI: 10.1063/1.1714461.

URL: http://aip.scitation.org/doi/10.1063/1.1714461 (visited on 10/04/2019).

[10] Jong Hyun Na et al. "Bulk Nickel-Niobium-Phosphorous-Boron Glasses Bearing Low Fractions of Chromium and Exhibiting High Toughness". Pat. (Pasadena, CA). Inc. Glassimetal Technology.

[11] Xuelian Li et al. "Glass transition temperature of bulk metallic glasses: A linear connection with the mixing enthalpy". In: *Journal of Applied Physics* 101.10 (May 15, 2007), p. 103540. ISSN: 0021-8979, 1089-7550. DOI: 10.1063/1.2736345. URL: http://aip.scitation.org/doi/10.1063/1.2736345 (visited on 01/07/2022).

[12] Vladimir Novikov and Ernst Rössler. "Correlation between glass transition temperature and molecular mass in non-polymeric and polymer glass formers". In: *Polymer* 54 (Dec. 1, 2013), pp. 6987–6991. DOI: 10.1016/j.polymer.2013.11.002.

[13] J. S. Langer. "Shear-transformation-zone theory of deformation in metallic glasses". In: *Scripta Materialia*. Viewpoint set no: 37. On mechanical behavior of metallic glasses 54.3 (Feb. 1, 2006), pp. 375–379. ISSN: 1359-6462. DOI: 10.1016/j.scriptamat.2005.10.005. URL: https://www.sciencedirect.com/science/article/pii/S1359646205006196 (visited on 04/18/2022).

[14] T.G. Nieh et al. "Effect of surface modifications on shear banding and plasticity in metallic glasses: An overview". In: *Progress in Natural Science: Materials International* 22 (Oct. 1, 2012), pp. 355–363. DOI: 10.1016/j.pnsc.2012.09.006.

[15] Shantanu Madge. "Toughness of Bulk Metallic Glasses". In: *Metals* 5.3 (July 17, 2015), pp. 1279–1305. ISSN: 2075-4701. DOI: 10.3390/met5031279. URL: http://www.mdpi.com/2075-4701/5/3/1279 (visited on 04/18/2022).

[16] Christopher A. Schuh, Todd C. Hufnagel, and Upadrasta Ramamurty. "Mechanical behavior of amorphous alloys". In: *Acta Materialia* 55.12 (July 1, 2007), pp. 4067–4109. ISSN: 1359-6454. DOI: 10.1016/j.actamat.2007.01.052. URL: https://www.sciencedirect.com/science/article/pii/S135964540700122X (visited on 04/17/2022).

[17] P Lowhaphandu and J.J. Lewandowski. "Fracture Toughness and Notch Toughness of Bulk Metallic Glass". In: *Scripta Metall. et Mater.* 38.12 (1998), pp. 1811–1817.

[18] Lisa Kraemer et al. "Production of Bulk Metallic Glasses by Severe Plastic Deformation". In: 2015. DOI: 10.3390/met5020720.

[19] Douglas C. Hofmann. "Bulk Metallic Glasses and Their Composites: A Brief History of Diverging Fields". In: *Journal of Materials* 2013 (Jan. 10, 2013), pp. 1–8. ISSN: 2314-4866, 2314-4874. DOI: 10.1155/2013/517904. URL: https://www.hindawi.com/archive/2013/517904/ (visited on 09/25/2019).

[20] Douglas C. Hofmann et al. "Castable Bulk Metallic Glass Strain Wave Gears: Towards Decreasing the Cost of High-Performance Robotics". In: *Scientific Reports* 6.1 (Dec. 2016), p. 37773. ISSN: 2045-2322. DOI: 10.1038/srep37773. URL: http://www.nature.com/articles/srep37773 (visited on 09/25/2019).

[21] Emily R. Kinser et al. "Nanopatterned Bulk Metallic Glass Biosensors". In: *ACS Sensors* 2.12 (Dec. 22, 2017), pp. 1779–1787. ISSN: 2379-3694, 2379-3694. DOI: 10.1021/acssensors.7b00455. URL: https://pubs.acs.org/doi/10.1021/acssensors.7b00455 (visited on 04/17/2022).

[22] Douglas C. Hofmann et al. "Designing metallic glass matrix composites with high toughness and tensile ductility". In: *Nature* 451.7182 (Feb. 2008). Number: 7182 Publisher: Nature Publishing Group, pp. 1085–1089. ISSN: 1476-4687. DOI: 10.1038/nature06598. URL: https://www.nature.com/articles/nature06598 (visited on 05/12/2022).

[23] D. S. Burnett. "The Genesis solar wind sample return mission: Past, present, and future". In: *Meteoritics & Planetary Science* 48.12 (Dec. 2013), pp. 2351–2370. ISSN: 10869379. DOI: 10.1111/maps.12241. URL: https://onlinelibrary.wiley.com/doi/10.1111/maps.12241 (visited on 01/10/2022).

[24] A. Peker and W. L. Johnson. "A highly processable metallic glass: Zr41.2 Ti13.8Cu12.5Ni10.0Be22.5". In: *Applied Physics Letters* 63.17 (June 4, 1998). Publisher: American Institute of PhysicsAIP, p. 2342. ISSN: 0003-6951. DOI: 10.1063/1.110520. URL: https://aip.scitation.org/doi/abs/10.1063/1.110520 (visited on 04/17/2022).

[25] Michael Floyd. "Development of Ferromagnetic Metallic Glasses into Low Loss Power Transformer Cores". PhD thesis. Pasadena, CA: California Institute of Technology, 2018.

[26] Long Hou et al. "Electronic specific heats for amorphous and crystallized alloys". In: *SpringerPlus* 5.1 (Dec. 2016), p. 699. ISSN: 2193-1801. DOI: 10.1186/s40064-016-2335-x. URL: http://springerplus.springeropen.com/articles/10.1186/s40064-016-2335-x (visited on 09/25/2019).

[27] F. H. Stillinger. "A Topographic View of Supercooled Liquids and Glass Formation". In: *Science* 267.5206 (Mar. 31, 1995), pp. 1935–1939. ISSN: 0036-8075, 1095-9203. DOI: 10.1126/science.267.5206.1935. URL: https://www.sciencemag.org/lookup/doi/10.1126/science.267.5206.1935 (visited on 06/06/2020).

[28] Pablo G. Debenedetti and Frank H. Stillinger. "Supercooled liquids and the glass transition". In: *Nature* 410.6825 (Mar. 2001), pp. 259–267. ISSN: 1476-4687. DOI: 10.1038/35065704. URL: https://www.nature.com/articles/35065704 (visited on 10/04/2019).

[29] Frank H. Stillinger. "Supercooled liquids, glass transitions, and the Kauzmann paradox". In: *The Journal of Chemical Physics* 88.12 (June 15, 1988), pp. 7818–7825. ISSN: 0021-9606, 1089-7690. DOI: 10.1063/1.454295. URL: http://aip.scitation.org/doi/10.1063/1.454295 (visited on 06/06/2020).

[30] Hillary L. Smith et al. "Separating the configurational and vibrational entropy contributions in metallic glasses". In: *Nature Physics* 13.9 (Sept. 2017), pp. 900–905. ISSN: 1745-2473, 1745-2481. DOI: 10.1038/nphys4142. URL: http://www.nature.com/articles/nphys4142 (visited on 04/09/2022).

[31] Julian H. Gibbs and Edmund A. DiMarzio. "Nature of the Glass Transition and the Glassy State". In: *The Journal of Chemical Physics* 28.3 (Mar. 1958), pp. 373–383. ISSN: 0021-9606, 1089-7690. DOI: 10.1063/1.1744141. URL: http://aip.scitation.org/doi/10.1063/1.1744141 (visited on 04/17/2022).

[32] Philip M. Morse. *Thermal physics*. 2d ed. New York: W. A. Benjamin, 1969. 431 pp. ISBN: 978-0-8053-7202-1.

[33] S. C. Glade et al. "Thermodynamics of Cu47Ti34Zr11Ni8, Zr52.5Cu17.9 Ni14.6Al10Ti5 and Zr57Cu15.4Ni12.6Al10Nb5 bulk metallic glass forming alloys". In: *Journal of Applied Physics* 87.10 (May 15, 2000), pp. 7242–7248. ISSN: 0021-8979, 1089-7550. DOI: 10.1063/1.372975. URL: http://aip.scitation.org/doi/10.1063/1.372975 (visited on 10/04/2019).

[34] Georg Kaltenboeck et al. "Accessing thermoplastic processing windows in metallic glasses using rapid capacitive discharge". In: *Scientific Reports* 4.1 (Oct. 1, 2014). Number: 1 Publisher: Nature Publishing Group, p. 6441. ISSN: 2045-2322. DOI: 10.1038/srep06441. URL: https://www.nature.com/articles/srep06441 (visited on 04/18/2022).

[35] Georg Kaltenboeck. "Investigation of capacitive discharge heating of metallic glasses". PhD thesis. Pasadena, CA: California Institute of Technology, 2016.

[36] Marios D. Demetriou et al. "US Patent for Injection molding of metallic glass by rapid capacitor discharge Patent (Patent # 9,297,058 issued March 29, 2016) - Justia Patents Search". Pat. 9297058 (California Institute of Technology). URL: https://patents.justia.com/patent/9297058 (visited on 04/18/2022).

[37] Gyan P. Johari and Martin Goldstein. "Viscous Liquids and the Glass Transition. II. Secondary Relaxations in Glasses of Rigid Molecules". In: *The Journal of Chemical Physics* 53.6 (Sept. 15, 1970), pp. 2372–2388. ISSN:

0021-9606, 1089-7690. DOI: 10.1063/1.1674335. URL: http://aip.scitation.org/doi/10.1063/1.1674335 (visited on 06/06/2020).

[38] F. Caporaletti et al. "A microscopic look at the Johari-Goldstein relaxation in a hydrogen-bonded glass-former". In: *Scientific Reports* 9.1 (Oct. 4, 2019). Number: 1 Publisher: Nature Publishing Group, p. 14319. ISSN: 2045-2322. DOI: 10.1038/s41598-019-50824-7. URL: https://www.nature.com/articles/s41598-019-50824-7 (visited on 04/18/2022).

[39] Jörg Hachenberg et al. "Merging of the alpha and beta relaxations and aging via the Johari–Goldstein modes in rapidly quenched metallic glasses". In: *Applied Physics Letters* 92.13 (Mar. 31, 2008). Publisher: American Institute of Physics, p. 131911. ISSN: 0003-6951. DOI: 10.1063/1.2903697. URL: https://aip.scitation.org/doi/full/10.1063/1.2903697 (visited on 04/18/2022).

[40] R. Busch, J. Schroers, and W. H. Wang. "Thermodynamics and Kinetics of Bulk Metallic Glass". In: *MRS Bulletin* 32.8 (Aug. 1, 2007), pp. 620–623. ISSN: 1938-1425. DOI: 10.1557/mrs2007.122. URL: https://doi.org/10.1557/mrs2007.122 (visited on 04/18/2022).

[41] Victor Gold, ed. *The IUPAC Compendium of Chemical Terminology: The Gold Book*. 4th ed. Research Triangle Park, NC: International Union of Pure and Applied Chemistry (IUPAC), 2019. DOI: 10.1351/goldbook. URL: https://goldbook.iupac.org/ (visited on 04/18/2022).

[42] Mingwei Chen. "A brief overview of bulk metallic glasses". In: *NPG Asia Materials* 3.9 (Sept. 2011), pp. 82–90. ISSN: 1884-4049, 1884-4057. DOI: 10.1038/asiamat.2011.30. URL: http://www.nature.com/articles/am2011149 (visited on 10/04/2019).

[43] I. Gutzow, D. Kashchiev, and I. Avramov. "Nucleation and crystallization in glass-forming melts: Olds problems and new questions". In: *Journal of Non-Crystalline Solids* 73.1 (Aug. 1985), pp. 477–499. ISSN: 00223093. DOI: 10.1016/0022-3093(85)90370-9. URL: https://linkinghub.elsevier.com/retrieve/pii/0022309385903709 (visited on 06/06/2020).

[44] Akihisa Inoue. "Stabilization of metallic supercooled liquid and bulk amorphous alloys". In: *Acta Materialia* 48.1 (Jan. 2000), pp. 279–306. ISSN: 13596454. DOI: 10.1016/S1359-6454(99)00300-6. URL: https://linkinghub.elsevier.com/retrieve/pii/S1359645499003006 (visited on 06/06/2020).

[45] Brent Fultz. *Phase Transitions in Materials*. 2nd ed. Cambridge: Cambridge University Press, 2020. ISBN: 978-1-108-48578-4. DOI: 10.1017/9781108641449. URL: https://www.cambridge.org/core/books/phase-transitions-in-materials/654FD0332505DBF186363DE899CC80E7 (visited on 04/18/2022).

[46] Yanchun Zhao et al. "Overheating effects on thermal stability and mechanical properties of Cu36Zr48Ag8Al8 bulk metallic glass". In: *Materials & Design* 31.2 (Feb. 1, 2010), pp. 1029–1032. ISSN: 0261-3069. DOI: 10.1016/j.matdes.2009.07.028. URL: https://www.sciencedirect.com/science/article/pii/S0261306909003707 (visited on 04/18/2022).

[47] Ritam Chatterjee. "Manufacturing of Metallic Glasses". In: *Advanced Materials Manufacturing & Characterization* 7.1 (2017), p. 6.

[48] G. N. Yang et al. "A study of cooling process in bulk metallic glasses fabrication". In: *AIP Advances* 5.11 (Nov. 2015), p. 117111. ISSN: 2158-3226. DOI: 10.1063/1.4935440. URL: http://aip.scitation.org/doi/10.1063/1.4935440 (visited on 04/18/2022).

[49] William L. Johnson. "Bulk Glass-Forming Metallic Alloys: Science and Technology". In: *MRS Bulletin* 24.10 (Oct. 1, 1999), pp. 42–56. ISSN: 1938-1425. DOI: 10.1557/S0883769400053252. URL: https://doi.org/10.1557/S0883769400053252 (visited on 04/18/2022).

[50] Tomasz Kozieł. "Estimation Of Cooling Rates In Suction Casting And Copper-Mould Casting Processes". In: *Archives of Metallurgy and Materials* 60 (June 1, 2015). DOI: 10.1515/amm-2015-0204.

[51] Jan Schroers, Quoc Pham, and Amish Desai. "Thermoplastic Forming of Bulk Metallic Glass— A Technology for MEMS and Microstructure Fabrication". In: *Microelectromechanical Systems, Journal of* 16 (May 1, 2007), pp. 240–247. DOI: 10.1109/JMEMS.0007.892889.

[52] Douglas C. Hofmann et al. "Compositionally graded metals: A new frontier of additive manufacturing". In: *Journal of Materials Research* 29.17 (Sept. 14, 2014), pp. 1899–1910. ISSN: 0884-2914, 2044-5326. DOI: 10.1557/jmr.2014.208. URL: https://www.cambridge.org/core/product/identifier/S0884291414002088/type/journal_article (visited on 09/25/2019).

[53] Gregg Jaeger. "The Ehrenfest Classification of Phase Transitions: Introduction and Evolution". In: *Archive for History of Exact Sciences* 53.1 (May 1, 1998), pp. 51–81. ISSN: 1432-0657. DOI: 10.1007/s004070050021. URL: https://doi.org/10.1007/s004070050021 (visited on 04/18/2022).

[54] Stephen J. Blundell and Katherine M. Blundell. *Concepts in Thermal Physics*. 2nd ed. Oxford: Oxford University Press, 2009. 512 pp. ISBN: 978-0-19-956209-1. DOI: 10.1093/acprof:oso/9780199562091.001.0001. URL: https://oxford.universitypressscholarship.com/10.1093/acprof:oso/9780199562091.001.0001/acprof-9780199562091 (visited on 04/18/2022).

[55] Michael I. Ojovan. "Ordering and structural changes at the glass–liquid transition". In: *Journal of Non-Crystalline Solids* 382 (Dec. 2013), pp. 79–86. ISSN: 00223093. DOI: 10.1016/j.jnoncrysol.2013.10.016. URL: https:

//linkinghub.elsevier.com/retrieve/pii/S0022309313005218 (visited on 10/24/2019).

[56] Frederick A. Lindemann. "The calculation of molecular vibration frequencies". In: *Phys. Z* 11 (1910), pp. 609–612.

[57] Robert W. Cahn. "Melting from within". In: *Nature* 413.6856 (Oct. 2001). Number: 6856 Publisher: Nature Publishing Group, pp. 582–583. ISSN: 1476-4687. DOI: 10.1038/35098169. URL: https://www.nature.com/articles/35098169 (visited on 04/18/2022).

[58] *Polymorphic Identification Using Raman Microscopy*. AZoM.com. Section: Materials Article. Aug. 26, 2014. URL: https://www.azom.com/article.aspx?ArticleID=11279 (visited on 02/22/2022).

[59] Tobias M. Gasser et al. "Structural characterization of ice XIX as the second polymorph related to ice VI". In: *Nature Communications* 12.1 (Feb. 18, 2021). Number: 1 Publisher: Nature Publishing Group, p. 1128. ISSN: 2041-1723. DOI: 10.1038/s41467-021-21161-z. URL: https://www.nature.com/articles/s41467-021-21161-z (visited on 02/19/2022).

[60] Men Zhu et al. "Possible existence of two amorphous phases of d -mannitol related by a first-order transition". In: *The Journal of Chemical Physics* 142.24 (June 28, 2015), p. 244504. ISSN: 0021-9606, 1089-7690. DOI: 10.1063/1.4922543. URL: http://aip.scitation.org/doi/10.1063/1.4922543 (visited on 02/22/2022).

[61] Jittisa Ketkaew et al. "Mechanical glass transition revealed by the fracture toughness of metallic glasses". In: *Nature Communications* 9.1 (Dec. 2018), p. 3271. ISSN: 2041-1723. DOI: 10.1038/s41467-018-05682-8. URL: http://www.nature.com/articles/s41467-018-05682-8 (visited on 02/22/2022).

[62] Qi An et al. "First-Order Phase Transition in Liquid Ag to the Heterogeneous G-Phase". In: *The Journal of Physical Chemistry Letters* 11.3 (Feb. 6, 2020), pp. 632–645. ISSN: 1948-7185, 1948-7185. DOI: 10.1021/acs.jpclett.9b03699. URL: https://pubs.acs.org/doi/10.1021/acs.jpclett.9b03699 (visited on 06/06/2020).

[63] Jürgen E. K. Schawe and Jörg F. Löffler. "Existence of multiple critical cooling rates which generate different types of monolithic metallic glass". In: *Nature Communications* 10.1 (Dec. 2019), p. 1337. ISSN: 2041-1723. DOI: 10.1038/s41467-018-07930-3. URL: http://www.nature.com/articles/s41467-018-07930-3 (visited on 07/15/2020).

[64] Jürgen E.K. Schawe, Stefan Pogatscher, and Jörg Löffler. "Thermodynamics of polymorphism in a bulk metallic glass: Heat capacity measurements by fast differential scanning calorimetry". In: *Thermochimica Acta* 685 (Mar. 1, 2020), p. 178518. DOI: 10.1016/j.tca.2020.178518.

[65] Jie Shen et al. "Metallic Glacial Glass Formation by a First-Order Liquid-Liquid Transition". In: *The Journal of Physical Chemistry Letters* (July 10, 2020), acs.jpclett.0c01789. ISSN: 1948-7185, 1948-7185. DOI: 10.1021/acs.jpclett.0c01789. URL: https://pubs.acs.org/doi/10.1021/acs.jpclett.0c01789 (visited on 07/16/2020).

[66] Qi An et al. "Formation of two glass phases in binary Cu-Ag liquid". In: *Acta Materialia* 195 (Aug. 2020), pp. 274–281. ISSN: 13596454. DOI: 10.1016/j.actamat.2020.05.060. URL: https://linkinghub.elsevier.com/retrieve/pii/S1359645420304079 (visited on 07/13/2020).

[67] Qi An et al. "The first order L-G phase transition in liquid Ag and Ag-Cu alloys is driven by deviatoric strain". In: *Scripta Materialia* 194 (Mar. 2021), p. 113695. ISSN: 13596462. DOI: 10.1016/j.scriptamat.2020.113695. URL: https://linkinghub.elsevier.com/retrieve/pii/S1359646220308174 (visited on 03/25/2021).

[68] Jong H. Na et al. "Observation of an apparent first-order glass transition in ultrafragile Pt–Cu–P bulk metallic glasses". In: *Proceedings of the National Academy of Sciences* 117.6 (Feb. 11, 2020), pp. 2779–2787. ISSN: 0027-8424, 1091-6490. DOI: 10.1073/pnas.1916371117. URL: http://www.pnas.org/lookup/doi/10.1073/pnas.1916371117 (visited on 06/06/2020).

[69] Carl V. Thompson and Frans Spaepen. "On the approximation of the free energy change on crystallization". In: *Acta Metallurgica* 27.12 (Dec. 1, 1979), pp. 1855–1859. ISSN: 0001-6160. DOI: 10.1016/0001-6160(79)90076-2. URL: https://www.sciencedirect.com/science/article/pii/0001616079900762 (visited on 04/18/2022).

[70] Robert L. Jack and Ludovic Berthier. "The melting of stable glasses is governed by nucleation-and-growth dynamics". In: *The Journal of Chemical Physics* 144.24 (June 28, 2016). Publisher: American Institute of Physics, p. 244506. ISSN: 0021-9606. DOI: 10.1063/1.4954327. URL: https://aip.scitation.org/doi/abs/10.1063/1.4954327 (visited on 04/18/2022).

[71] Ludovic Berthier and Mark D. Ediger. "Facets of glass physics". In: *Physics Today* 69.1 (Jan. 2016). Publisher: American Institute of Physics, pp. 40–46. ISSN: 0031-9228. DOI: 10.1063/PT.3.3052. URL: https://physicstoday.scitation.org/doi/10.1063/PT.3.3052 (visited on 04/18/2022).

[72] Elijah Flenner et al. "Front-mediated melting of ultrastable glasses". In: *Physical Review Letters* 123.17 (Oct. 23, 2019), p. 175501. ISSN: 0031-9007, 1079-7114. DOI: 10.1103/PhysRevLett.123.175501. arXiv: 1903.09108. URL: http://arxiv.org/abs/1903.09108 (visited on 04/18/2022).

[73] Bernard D. Cullity. *Elements of x-ray diffraction*. 3. printing. Addison-Wesley series in metallurgy and materials. Reading, Mass.: Addison-Wesley, 1967. 514 pp. ISBN: 978-0-201-01230-9.

[74]   R. Busch, E. Bakke, and W. L. Johnson. "Viscosity of the supercooled liquid and relaxation at the glass transition of the Zr46.75Ti8.25Cu7.5Ni10Be27.5 bulk metallic glass forming alloy". In: *Acta Materialia* 46.13 (Aug. 10, 1998), pp. 4725–4732. ISSN: 1359-6454. DOI: 10.1016/S1359-6454(98)00122-0. URL: https://www.sciencedirect.com/science/article/pii/S1359645498001220 (visited on 04/18/2022).

[75]   Zach Evenson and Ralf Busch. "Enthalpy recovery and free volume relaxation in a Zr44Ti11Ni10Cu10Be25 bulk metallic glass". In: *Journal of Alloys and Compounds*. XVII International Symposium on Metastable, Amorphous and Nanostructured Materials 509 (June 1, 2011), S38–S41. ISSN: 0925-8388. DOI: 10.1016/j.jallcom.2010.12.044. URL: https://www.sciencedirect.com/science/article/pii/S0925838810030173 (visited on 04/18/2022).

[76]   J. H. Na et al. "Compositional landscape for glass formation in metal alloys". In: *Proceedings of the National Academy of Sciences* 111.25 (June 24, 2014), pp. 9031–9036. ISSN: 0027-8424, 1091-6490. DOI: 10.1073/pnas.1407780111. URL: http://www.pnas.org/cgi/doi/10.1073/pnas.1407780111 (visited on 05/05/2021).

[77]   Qi An et al. "The L–G phase transition in binary Cu–Zr metallic liquids". In: *Physical Chemistry Chemical Physics* 24.1 (2022), pp. 497–506. ISSN: 1463-9076, 1463-9084. DOI: 10.1039/D1CP04157F. URL: http://xlink.rsc.org/?DOI=D1CP04157F (visited on 02/15/2022).

A p p e n d i x   A

THERMODYNAMIC DERIVATIONS: A GAUSSIAN DENSITY OF STATES IN PEL THEORY

The included derivations correspond to Equations 1.10 - 1.14 in Chapter 1.2.

Starting with the equation for a Gaussian density of states to describe the inherent energy states available to a glass system, with Φ the potential energy of an inherent state,

$$D(\Phi) = \frac{1}{\sigma\sqrt{2\pi}} \exp \frac{-(\Phi - \bar{\Phi})^2}{2\sigma^2} = \frac{1\,state}{atom}, \tag{A.1}$$

one can then define a general equation for the partition function:

$$Z = \int D(\Phi) \exp \left[\frac{-\Phi}{kT}\right] d\Phi. \tag{A.2}$$

Substituting in $D(\Phi)$ gives

$$Z = \frac{1}{\sigma\sqrt{2\pi}} \int \exp \left[\frac{-(\Phi - \overset{0}{\bar{\Phi}})^2}{2\sigma^2}\right] \exp \left[\frac{-\Phi}{kT}\right] d\Phi, \tag{A.3}$$

where $\bar{\Phi}$ goes to zero with Gaussian center set at zero.

Simplifying the exponential terms,

$$Z = \frac{1}{\sigma\sqrt{2\pi}} \int \exp \left[-\left(\frac{\Phi^2}{2\sigma^2} + \frac{\Phi}{kT}\right)\right] d\Phi. \tag{A.4}$$

Complete the square of bracketed exponential term in A.4 to define a new Gaussian as Φ' by first rearranging to

$$\Phi^2 + \frac{2\sigma^2}{kT}\Phi. \tag{A.5}$$

One can then complete the square

$$\left[\left(\Phi + \frac{\sigma^2}{kT}\right)^2 - \left(\frac{\sigma^2}{kT}\right)^2\right], \tag{A.6}$$

and set

$$\Phi' = \left(\Phi + \frac{\sigma^2}{kT}\right) \tag{A.7}$$

to substitute back into the exponential and distributing the negative sign.

$$\mathbb{Z} = \frac{1}{\sigma\sqrt{2\pi}} \int \exp\left[-\left(\Phi + \frac{\sigma^2}{kT}\right)^2 + \left(\frac{\sigma^2}{kT}\right)^2\right] d\Phi. \tag{A.8}$$

$$\mathbb{Z} = \frac{1}{\sigma\sqrt{2\pi}} \exp\left(\frac{\sigma^2}{kT}\right)^2 \overbrace{\int \exp(-\Phi')^2 d\Phi.}^{\sqrt{\pi}} \tag{A.9}$$

The integral expression in A.9 becomes $\sqrt{\pi}$ due to the Gaussian integral relationship $\int_{-\infty}^{\infty} \exp -a(x + b)^2 dx = \sqrt{\frac{\pi}{a}}$ where $a > 0$.

Where the $\sqrt{\pi}$ cancels with the denominator to form the partition function with a Gaussian configurational density of states,

$$\mathbb{Z}(\Phi, T) = \frac{1}{\sigma\sqrt{2}} \exp\left(\frac{\sigma^2}{kT}\right)^2. \tag{A.10}$$

Utilizing this partition function, the thermodynamic state functions can be defined, i.e., Helmholtz free energy (F), entropy (S), internal energy (U), enthalpy (H), and heat capacity (C_p).

Starting with the Helmholtz free energy (F), the derivations are carried out below utilizing relationships defined in Morse.[32]

$$\begin{aligned}
F &= -kT \ln(\mathbb{Z}) \\
&= -kT \ln\left[\frac{1}{\sigma\sqrt{2}} \exp\left(\frac{\sigma^2}{kT}\right)^2\right] \\
&= -kT \ln\left(\frac{1}{\sigma\sqrt{2}}\right) - kT \left(\frac{\sigma^2}{kT}\right)^2 \\
&= +kT \ln \sigma\sqrt{2} - \frac{\sigma^4}{kT}
\end{aligned}$$

Then for Entropy,

$$S = -\frac{dF}{dT}$$

$$= -k \ln\left(\sigma\sqrt{2}\right) - \frac{\sigma^4}{kT^2}$$

For internal energy,

$$U = F + TS$$

$$= kT \ln\left(\sigma\sqrt{2}\right) - \frac{\sigma^4}{kT} + \frac{-\sigma^4}{kT^2}T$$

$$= \gamma - \frac{2\sigma^4}{kT},$$

where $\gamma = kT \ln\left(\sigma\sqrt{2}\right)$.

Enthalpy (H) can be simplified with a simple observation: $dH = dU + VdP$, where VdP is negligible due to the constant ambient pressure in standard DSC experiments. Thus,

$$H = U = \gamma - \frac{2\sigma^4}{kT}. \tag{A.11}$$

Through the PEL and corresponding assumptions leading to a Gaussian distribution-based partition function outlined above, enthalpy has a T^{-1} dependence (correlated with the n=1 dependence in Chapter 2).

Finally, through the above assumptions, the Gaussian landscape constant pressure heat capacity (C_p) has a T^{-2} dependence;

$$C_p = \frac{dU}{dT} = \gamma + \frac{2\sigma^2}{kT^2}. \tag{A.12}$$

A p p e n d i x B

SUPPLEMENTAL MATERIALS FOR CHAPTER 2

B.1 Underlying Assumptions

There are some fundamental assumptions made in this work that streamline the mathematics. Starting from first principles and the First Law of Thermodynamics, we derive our mathematical representation for configurational enthalpy and its underlying concepts. Through fundamental expansions and indexed steps, the enthalpy is described as a function of the potential energy with the kinetic energy scaling only with temperature.

From the First Law, $U = TS - PV$, its perfect differential $dU = TdS - PdV$, and the fundamental expression for enthalpy, $H = U + PV$, the enthalpic differential is determined as $dH = dU + VdP$.[32] Under the conditions of this work $V = 10^{-5}m^3mol^{-1}$, and P = 1 atm = 10^{+5} Pa. Thus, $VdP = 1Jmol^{-1}$ and is negligible compared to the experimental h_{Config} of $10kJmol^{-1}$. This simplification yields enthalpy as a strict function of internal energy, U. Expanding this energy, however, reveals $U = PE + KE$ with the potential energy (PE) represented now as ϕ, and the kinetic energy is known as $\frac{3k_BT}{2}$ from the equipartition theorem (equipartition theorem of ideal gas states each degree of freedom of kinetic energy is $\frac{k_BT}{2}$. In three dimensions this yields $\frac{3k_BT}{2}$).[32]

Probing deeper into the potential energy description, ϕ can be expanded; $\phi = \phi^l - \phi^x$, with ϕ^l and ϕ^x the potential energy of the liquid and crystalline components, respectively. Each can then be expanded further into configurational and vibrational terms:

$$\phi^l = \phi^l_{Config} + \phi^l_{vib} = \phi^l_{Config} + \phi^l_{vib,har} + \phi^l_{vib,anh}$$

$$\phi^x = \phi^x_{Config} + \phi^x_{vib} = \phi^x_{Config} + \phi^x_{vib,har} + \phi^x_{vib,anh}$$

where the vibrational term contains separable harmonic and anharmonic components.

Substituting terms,

$$\phi = \phi^l - \phi^x$$
$$= \phi^l_{Config} - \phi^x_{Config} + \phi^l_{vib,har} - \phi^x_{vib,har} + \phi^l_{vib,anh} - \phi^x_{vib,anh}$$

can be simplified via two approximations. The harmonic approximation utilizes the Dulong-Petit heat capacity of 3R as a description of the harmonic component of the potential energy. With $C_{P,har} = 3R = \phi^l + \phi^x$, the two terms split evenly yielding $\phi^l = \phi^x = \frac{3R}{2}$. The anharmonic approximation emphasizes the Debye-Grüneisen anharmonic heat capacity, $C_P - C_V = \alpha^2 BvT$ with α the coefficient of thermal expansion, B the isothermal bulk modulus, v the molar volume, and T the temperature in Kelvin. When calculated, the $\phi^l_{vib,anh}$ and $\phi^x_{vib,anh}$ values are negligible compared to the Dulong-Petit ($25 Jmol^{-1}$) and experimental enthalpy measurements ($10 kJmol^{-1}$). These components are thus neglected.

The equations for potential energy and enthalpy simplify to a configurational dependence, $\phi = \phi^l - \phi^x = \phi^l_{Config} - \phi^x_{Config} = \phi^{lx}_C onfig$, and $H = U = \frac{3k_BT}{2} + \phi$ with a standardized kinetic energy term. From this, the enthalpy is termed the configurational energy in this work:

$$H = H_C = \phi^{lx}_{Config} + \frac{3k_BT}{2},$$

where H can be offset by the kinetic energy term, $H - \frac{3k_BT}{2} = \phi^{lx}_{Config}$, thus the configurational enthalpy is truly a measure of the change in potential energy between the liquid and crystal through various phase transformations (glass transition, crystallization, and melt).

Given configurational enthalpy is reported in units of J/g, the various thermodynamic variables discussed here are all specific values. Thus, $H_C = h_C$; $S_C = s_C$; $C_V = c_V$. Further, while here configurational components are denoted by the subscript "$Config$" for clarify, the text utilises the subscript "c" for concision.

B.2   Entropy Derivation: Equivalence of Equation 2.1 and 2.2

In the text, Equation 2.2 is derived from 2.2. Below is an outline of the steps. Starting with Equation 2.1,

$$h_C(T) = h_C(\infty) \left[1 - \left(\frac{\theta_h}{T} \right)^n \right]$$

the specific heat capacity becomes

$$
\begin{aligned}
c_V &= \frac{\partial Q(T)}{\partial T} = \frac{\partial U(T)}{\partial T} = \frac{\partial h_C(T)}{\partial T} = \frac{\partial}{\partial T}\left(h_C(\infty) - \frac{h_C(\infty)\theta_h^n}{T^n}\right) \\
&= \frac{\partial}{\delta T}(h_C(T))_{T=\infty} - \frac{\partial}{\partial T}\left(\frac{h_C(\infty)\theta_h^n}{T^n}\right) \\
&= c_{V,\infty} - \left(\frac{\theta_h^n}{T^n}c_V(T)\right)_{T=\infty} + \frac{nh_C(\infty)\theta_h^n}{T^n} \\
&= c_{V,\infty} + \frac{nh_C(\infty)\theta_h^n}{T^{n+1}}.
\end{aligned}
$$

When ignoring the pressure dependence of $h_C(\infty)$ and θ_h at ambient pressure; i.e., ignoring the PV term in the free energy, c_C is obtained:

$$
c_C = \frac{nh_C(\infty)\theta_h^n}{T^{n+1}}
$$

For the entropy, toward the high-temperature limit,

$$
\begin{aligned}
s_C &= \int_T^\infty \frac{c_V}{T}dT = \int_T^\infty \left(\frac{c_{V,\infty}}{T} + \frac{nh_C(\infty)\theta_h^n}{T^{n+2}}\right) \\
&= s_{C,\infty} + \frac{nh_C(\infty)\theta_h^n}{n+1}\frac{1}{T^{n+1}}
\end{aligned}
$$

Now change the above expression for configurational entropy to the familiar micro-canonical form. Multiply the second term of the configurational enthalpy by

$$
s_C = s_{C,\infty} + \frac{nh_c(\infty)}{\theta_h(n+1)}\left(\frac{\theta_h}{T}\right)^{n+1}
$$

From equation "1",

$$
\frac{h_C(\infty) - h_C(T))}{h_C(\infty)} = \left(\frac{\theta_h}{T}\right)^n
$$

or

$$
\left(\frac{h_C(\infty) - h_C(T)}{h_C(\infty)}\right)^{\frac{1}{n}} = \left(\frac{\theta_h}{T}\right)
$$

So

$$
\left(\frac{\theta_h}{T}\right)^{n+1} = \left(\frac{h_C(\infty) - h_C(T)}{h_C(\infty)}\right)^{\frac{1}{n}}\left(\frac{h_C(\infty) - h_C(T)}{h_C(\infty)}\right) = \left(\frac{h_C(\infty) - h_C(T)}{h_C(\infty)}\right)^{\frac{n+1}{n}}
$$

where

$$
s_C = s_{C,\infty} - \frac{nh_c(\infty)}{\theta_h(n+1)}\left(\frac{h_C(\infty) - h_C(T)}{h_C(\infty)}\right)^{\frac{n+1}{n}} = s_{C,\infty} - C\left(\frac{h_C(\infty) - h_C(T)}{h_C(\infty)}\right)^{\frac{n+1}{n}}
$$

With Equation 2.2 in Chapter 2 written in terms of configurational potential energies ϕ and ϕ_0, these are equivalent to h_C and h_∞, respectively ,given the prior assumptions, with C a constant. The above equation generalizes to Equation 2.2. So the above exhibits the derivation from Equation 2.1 to 2.2,

$$s_c(\phi) \propto s_C(\phi_0) - C(\phi_0 - \phi)^{\frac{n+1}{n}}$$

B.3 Sn Heating Rate Temperature Correction

DTA runs were completed on pure Sn (99.999%) at incremental heating rates from 0.5 to 20 K/min. These heat flow curves are plotted in Figure B.1 and increased peak broadening and peak shift are observed at higher heating rates. This peak broadening and shift effect are the results of thermal lag in the system, where the sample has not yet caught up to the temperature at the thermocouple. These peak shift corrections (Table B.1) are utilized in calculating accurate enthalpy peak temperatures as discussed in Section 2.4.
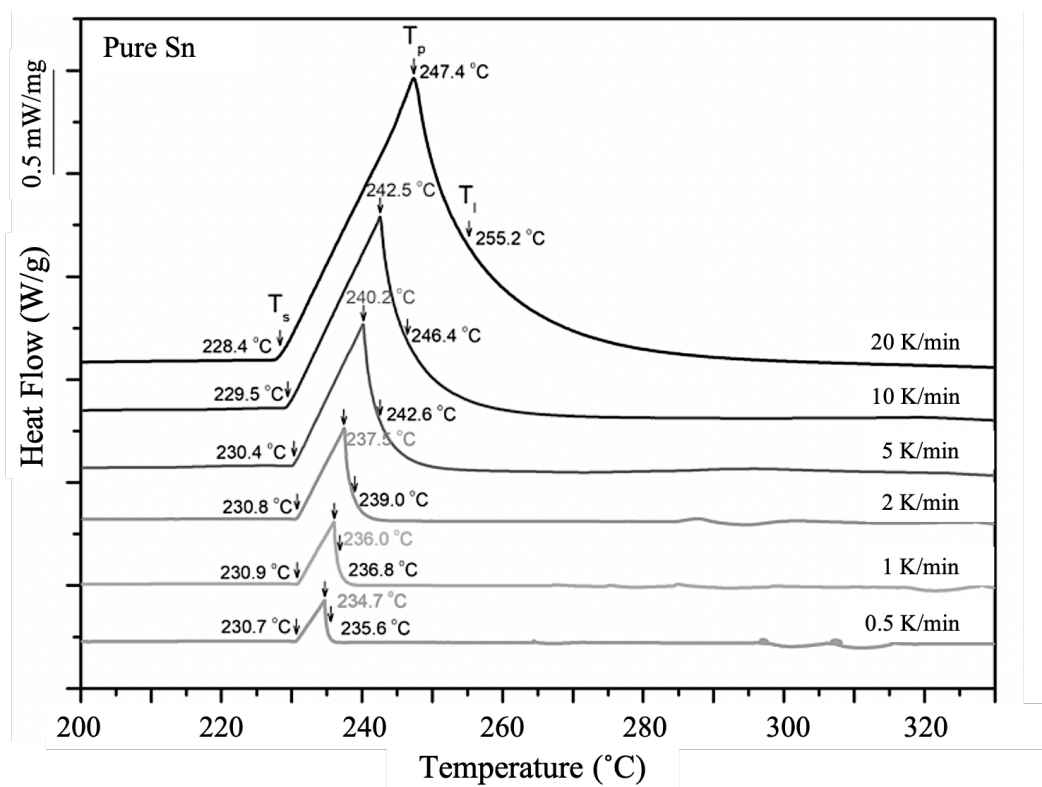

Figure B.1: Sn heat flow responses with respect to heating rate.

The correction values utilized are as follows:

Heating Rate (K/min)	Temperature Correction (K)
0.1	0
0.2	0
0.5	0
1	-0.8
1.5	-1
2	-1.5
3	-2
5	-4.2
8	-5.2
10	-6.5
15	-9
20	-11

Table B.1: Peak offset correction values from Figure B.1.

	Cu_{14}	Cu_{16}	Cu_{18}	Cu_{20}	Cu_{23}	Cu_{27}
T_{gm} (K)	533	548	551	-	-	651
Δh_C (J/g)	27	20	23.7	-	-	15.7

Table B.2: Raw data accompanying Figure 2.11 identifying the trend of fragility, copper content, glass-melting temperature, and latent heat of glass-melting.

B.4 Raw Data

Raw data are included in the supplemental material excel file included in the CaltechThesis archive.

A p p e n d i x   C

SUPPLEMENTAL MATERIALS FOR CHAPTER 3

C.1 Raw Data

Raw data are included in the supplemental material excel file included in the CaltechThesis archive.
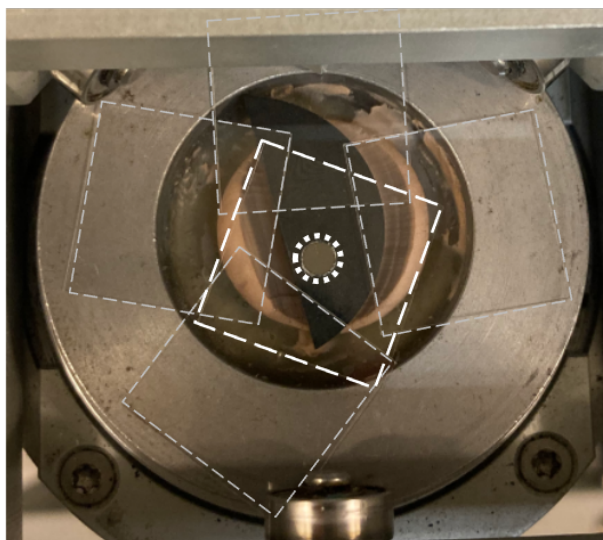

Figure C.1: Cover slip location for carbon-puck masking method. Central cover slip with hole highlighted with white borders on free edges. Full cover slips outlined by grey dashed lines.

A p p e n d i x D

SUPPLEMENTAL MATERIALS FOR CHAPTER 4

Compiled supporting materials for Chapter 4.

	T_g (K)	T_L (K)	m
$Ni_{70.4}Cr_{5.64}Nb_{4.46}P_{16.5}B_3$	671	1243	54

Table D.1: Ni210 Properties. These properties were assumed equivalent to Ni208 within error given sample properties were not able to be confirmed due to non-functional measurement apparatuses.[8]
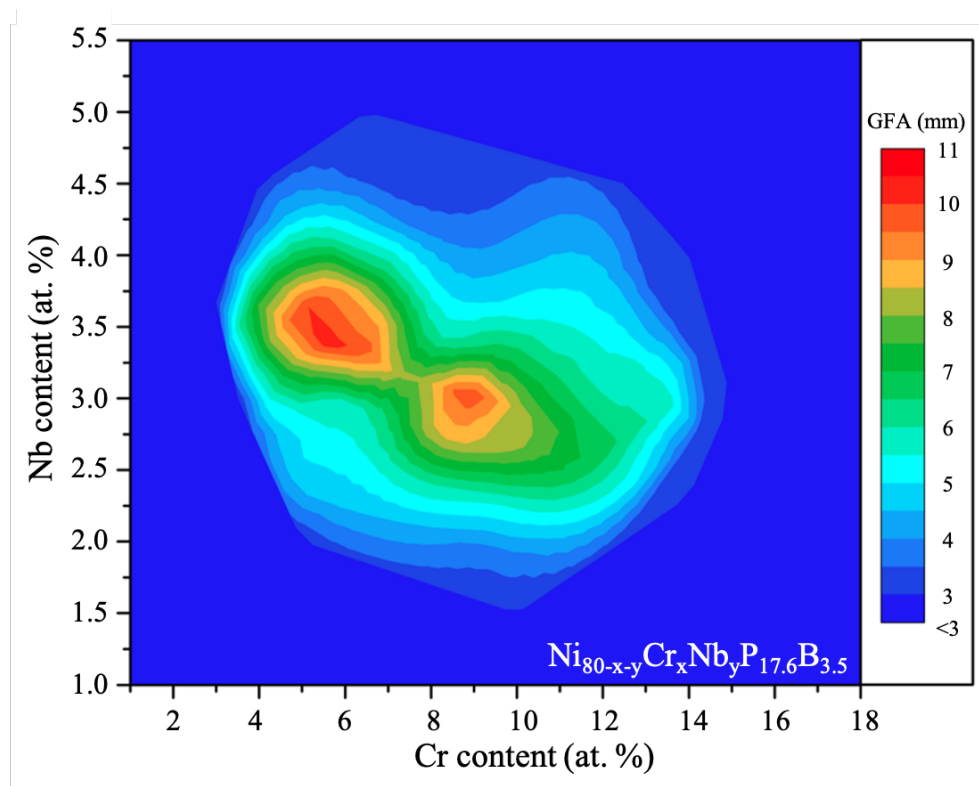
Figure D.1: The color contour plot equivalent to the dashed contour in Figure 4.1. Included for visual clarity.REF
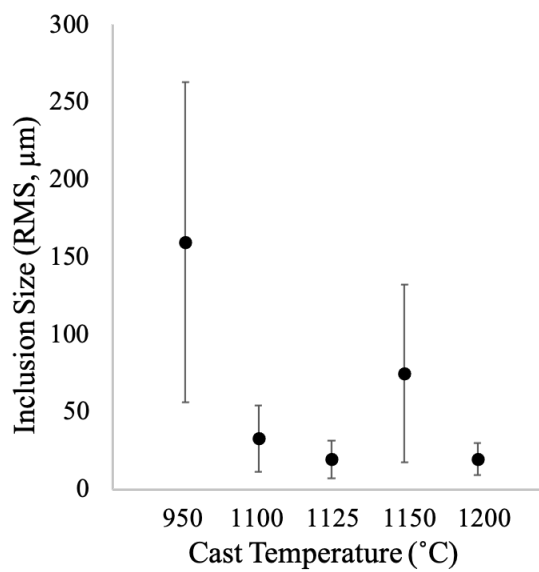

Figure D.2: Inclusion sizes across the direct cast samples' casting temperatures.
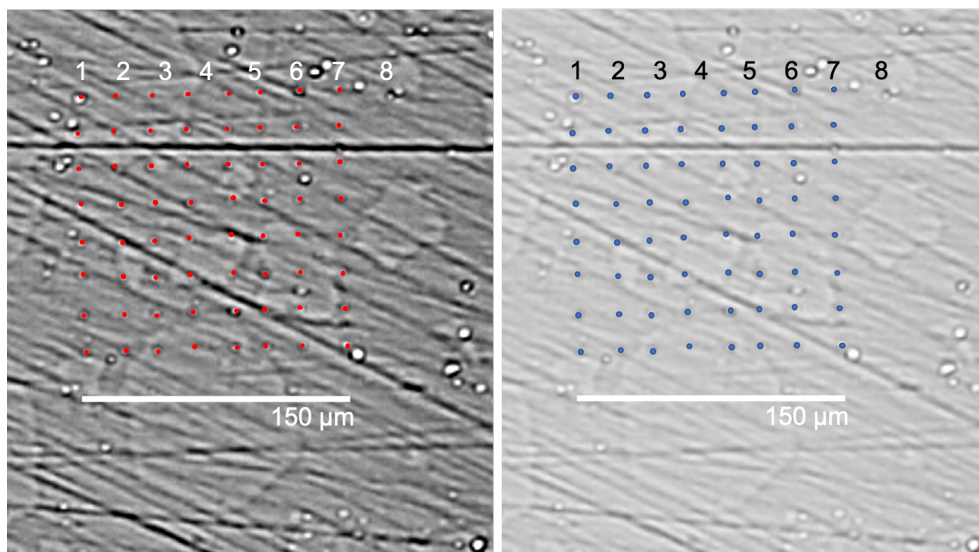
Figure D.3: Two lighting approaches for inclusion visualization on the same sample area. Nanoindentations utilized for sample location identification in SEM.
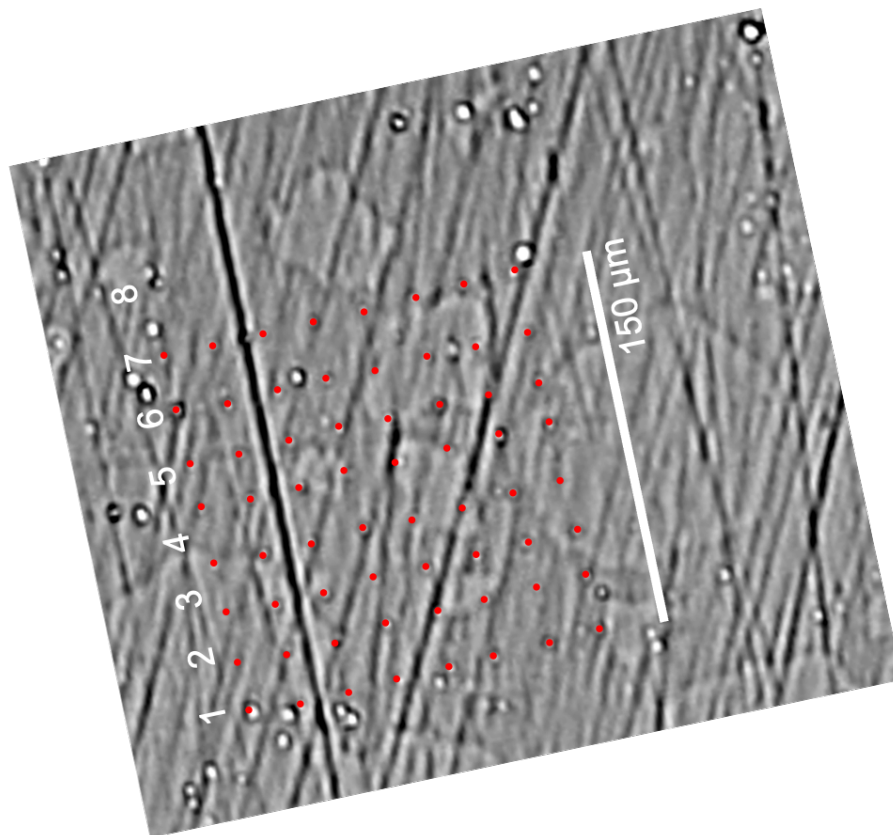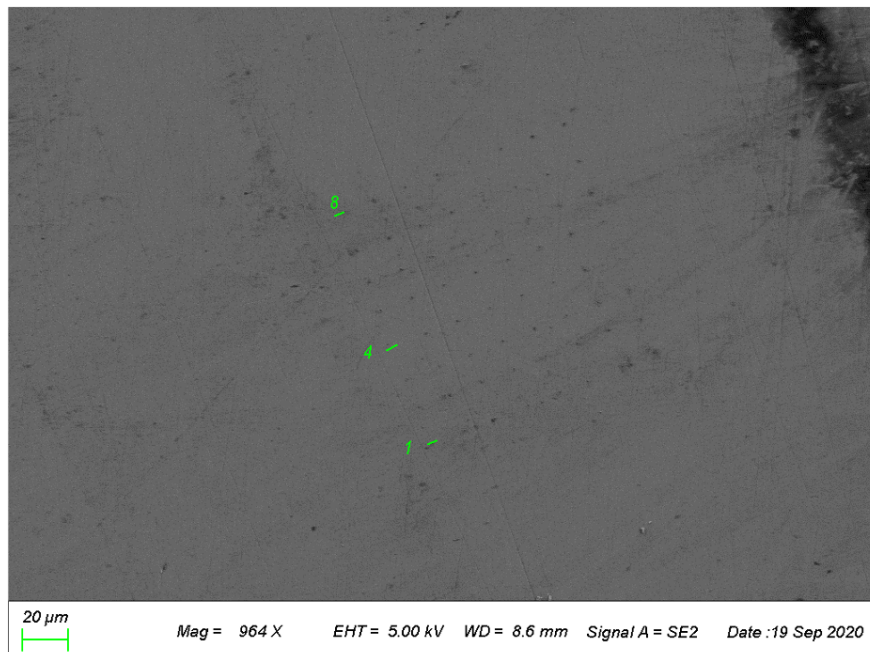
Figure D.4: Top (a): SEM image depicting lack of visibility of the inclusions relative to the 10x optical image (bottom, b).
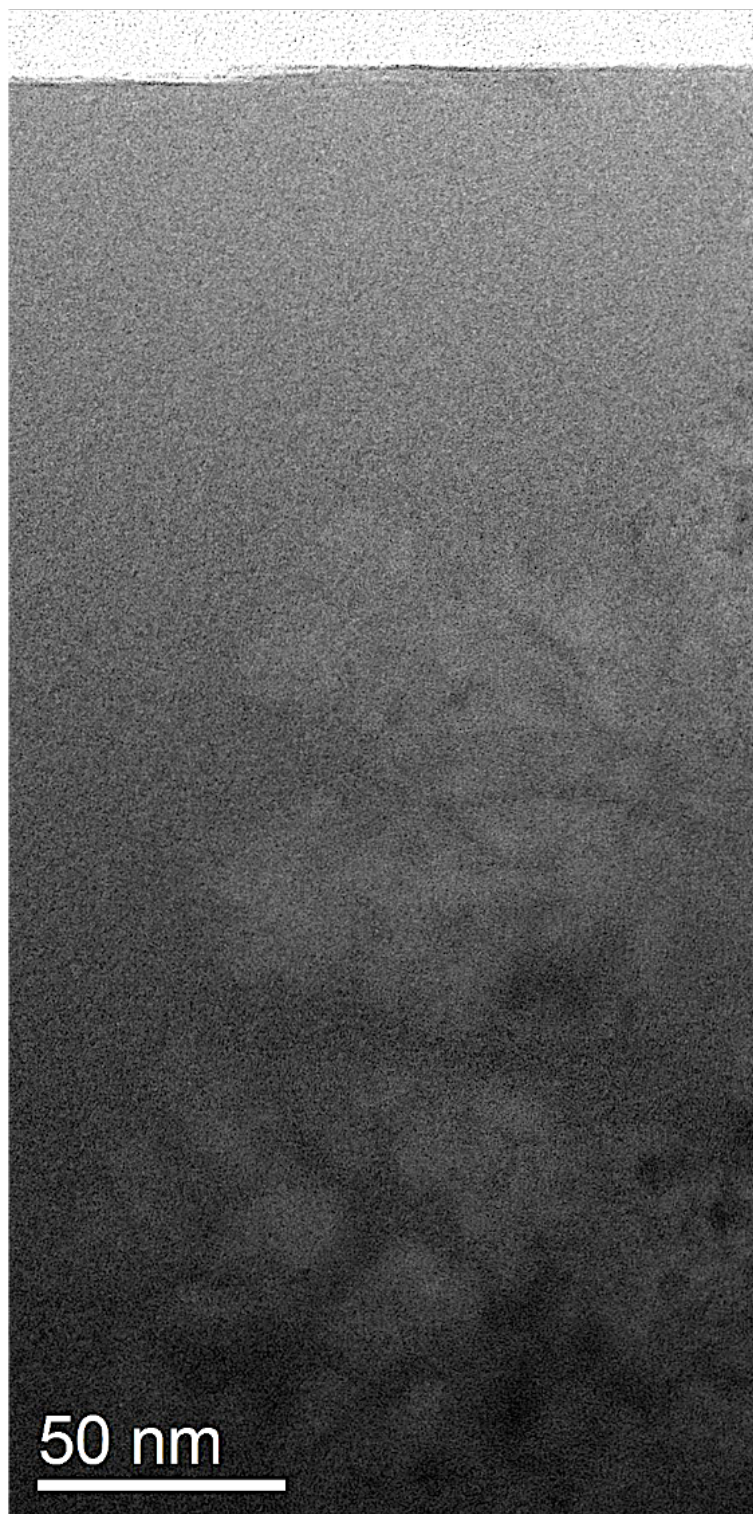
Figure D.5: TEM 64k zoom on Ni208 inclusion-matrix interface. Enlarged here for clarity. The reader is advised to view the image in the electronic version.

A p p e n d i x   E

RESOURCES FOR SURVIVING GRADUATE SCHOOL

E.1   The "Snake Fight" Portion of Your Thesis Defense by Luke Burns

FAQ:

Q: Do I have to kill the snake?

A: University guidelines state that you have to "defeat" the snake. There are many ways to accomplish this. Lots of students choose to wrestle the snake. Some construct decoys and elaborate traps to confuse and then ensnare the snake. One student brought a flute and played a song to lull the snake to sleep. Then he threw the snake out a window.

Q: Does everyone fight the same snake?

A: No. You will fight one of the many snakes that are kept on campus by the facilities department.

Q: Are the snakes big?

A: We have lots of different snakes. The quality of your work determines which snake you will fight. The better your thesis is, the smaller the snake will be.

Q: Does my thesis adviser pick the snake?

A: No. Your adviser just tells the guy who picks the snakes how good your thesis was.

Q: What does it mean if I get a small snake that is also very strong?

A: Snake-picking is not an exact science. The size of the snake is the main factor. The snake may be very strong, or it may be very weak. It may be of Asian, African, or South American origin. It may constrict its victims and then swallow them whole, or it may use venom to blind and/or paralyze its prey. You shouldn't read too much into these other characteristics. Although if you get a poisonous snake, it often means that there was a problem with the formatting of your bibliography.

Q: When and where do I fight the snake? Does the school have some kind of pit or arena for snake fights?

A: You fight the snake in the room you have reserved for your defense. The fight generally starts after you have finished answering questions about your thesis. However, the snake will be lurking in the room the whole time and it can strike at any point. If the snake attacks prematurely it's obviously better to defeat it and get back to the rest of your defense as quickly as possible.

Q: Would someone who wrote a bad thesis and defeated a large snake get the same grade as someone who wrote a good thesis and defeated a small snake?

A: Yes.

Q: So then couldn't you just fight a snake in lieu of actually writing a thesis?

A: Technically, yes. But in that case the snake would be very big. Very big, indeed.

Q: Could the snake kill me?

A: That almost never happens. But if you're worried, just make sure that you write a good thesis.

Q: Why do I have to do this?

A: Snake fighting is one of the great traditions of higher education. It may seem somewhat antiquated and silly, like the robes we wear at graduation, but fighting a snake is an important part of the history and culture of every reputable university. Almost everyone with an advanced degree has gone through this process. Notable figures such as John Foster Dulles, Philip Roth, and Doris Kearns Goodwin (to name but a few) have all had to defeat at least one snake in single combat.

Q: This whole snake thing is just a metaphor, right?

A: I assure you, the snakes are very real.